

AD-A058 365 AGBABIAN ASSOCIATES EL SEGUNDO CALIF  
LOW-CYCLE FATIGUE TESTS OF HOLLOW CONCRETE SPHERES WITH IMPLICA--ETC(U)  
APR 78 M B BALACHANDRA, C F BAGGE, H H HAYNES DNA001-77-C-0245

UNCLASSIFIED

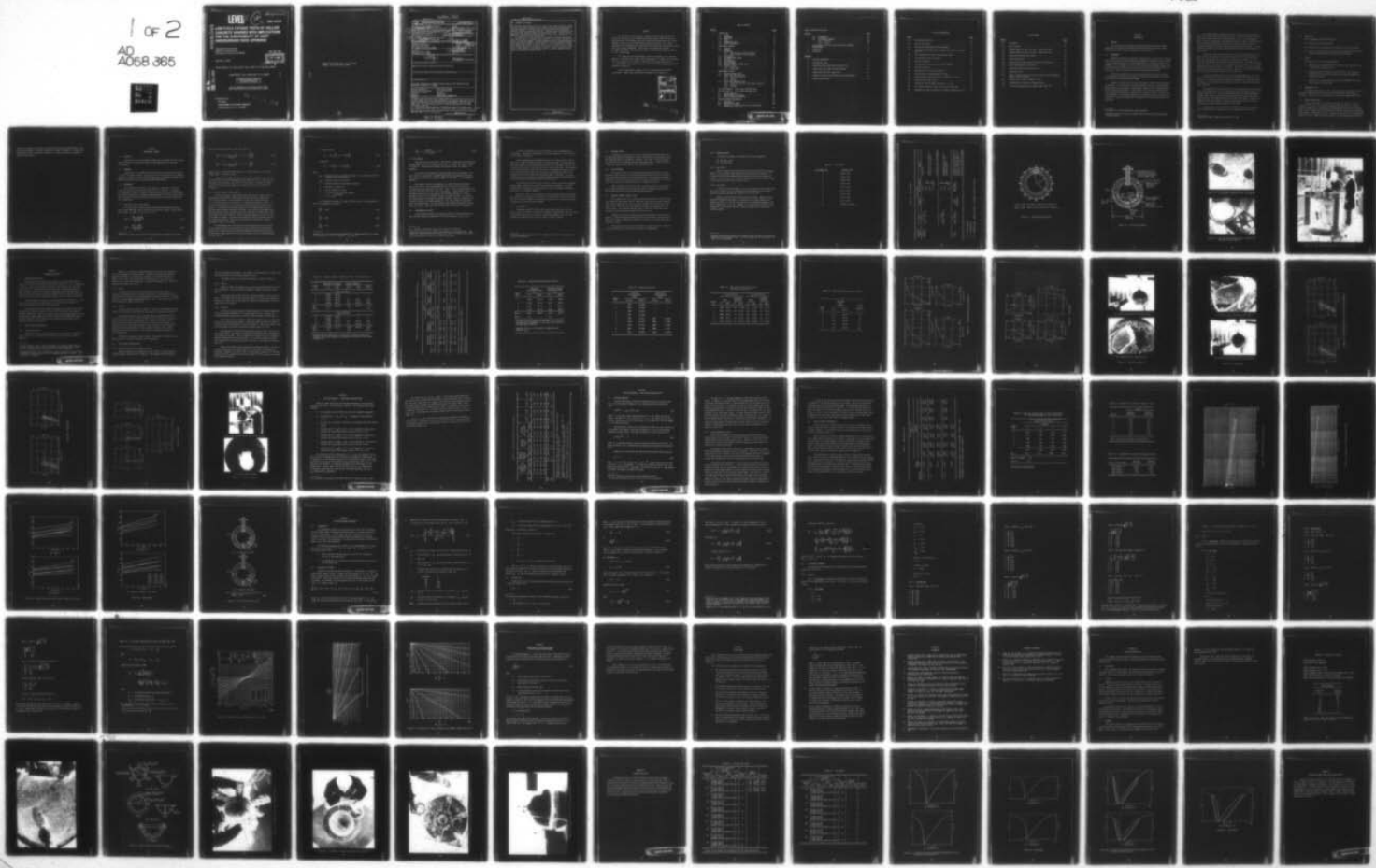
AA-R-7740-4551

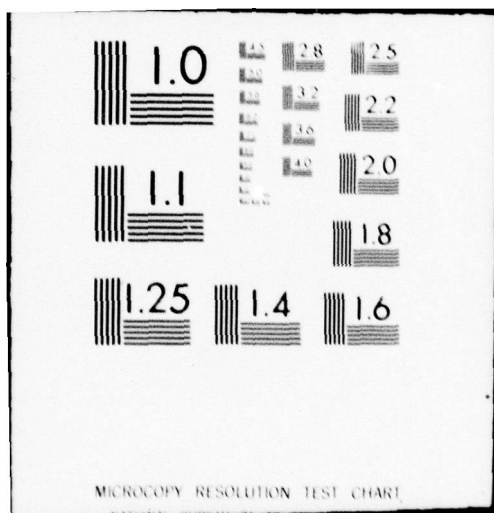
DNA-4433F

F/G 11/2

NL

1 of 2  
AD  
A058 365





ADA 058365

LEVEL II

12  
SC

AD-E300275

DNA 4433F

# LOW-CYCLE FATIGUE TESTS OF HOLLOW CONCRETE SPHERES WITH IMPLICATIONS FOR THE SURVIVABILITY OF DEEP- UNDERGROUND ROCK OPENINGS

Agbabian Associates  
250 North Nash Street  
El Segundo, California 90245

30 April 1978

Final Report for Period 27 April 1977-31 January 1978

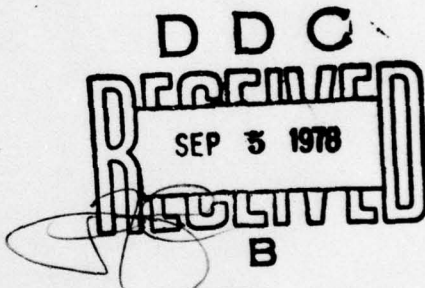
AD No. \_\_\_\_\_  
DDC FILE COPY

CONTRACT No. DNA 001-77-C-0245

APPROVED FOR PUBLIC RELEASE;  
DISTRIBUTION UNLIMITED.

THIS WORK SPONSORED BY THE DEFENSE NUCLEAR AGENCY  
UNDER RDT&E RMSS CODE B344077462 J34HAXSX31111 H2590D.

Prepared for  
Director  
DEFENSE NUCLEAR AGENCY  
Washington, D. C. 20305



78 06 23 068

Destroy this report when it is no longer  
needed. Do not return to sender.



18 DNA, SBIE

UNCLASSIFIED

SECURITY CLASSIFICATION OF THIS PAGE (When Data Entered)

REPORT DOCUMENTATION PAGE		READ INSTRUCTIONS BEFORE COMPLETING FORM
1. REPORT NUMBER DNA 4433F AD-E300 275	2. GOVT ACCESSION NO. 9	3. RECIPIENT'S CATALOG NUMBER
4. TITLE (including subtitle) LOW-CYCLE FATIGUE TESTS OF HOLLOW CONCRETE SPHERES WITH IMPLICATIONS FOR THE SURVIVABILITY OF DEEP-UNDERGROUND ROCK OPENINGS.		5. TYPE OF REPORT & PERIOD COVERED Final Report, for Period 27 Apr 77-31 Jan 78
6. AUTHOR(S) M. Balu/Balachandra, Agbabian Associates Carl F. Bagge, Agbabian Associates Harvey H. Haynes, Civil Engineering Laboratory	7. PERFORMING ORG. REPORT NUMBER AA- R-7740-4551	8. CONTRACT OR GRANT NUMBER(S) DNA 001-77-C-0245
9. PERFORMING ORGANIZATION NAME AND ADDRESS Agbabian Associates 250 North Nash Street El Segundo, California 90245	10. PROGRAM ELEMENT, PROJECT, TASK AREA & WORK UNIT NUMBERS Subtask J34HAXSX3111-11	11. 27104
11. CONTROLLING OFFICE NAME AND ADDRESS Director Defense Nuclear Agency Washington, D.C. 20305	12. REPORT DATE 30 Apr 78	13. NUMBER OF PAGES 150
14. MONITORING AGENCY NAME & ADDRESS (if different from Controlling Office) 12 140p.	15. SECURITY CLASS (of this report) UNCLASSIFIED	16. DECLASSIFICATION/DOWNGRADING SCHEDULE
17. DISTRIBUTION STATEMENT (of this Report) Approved for public release; distribution unlimited.		
18. DISTRIBUTION STATEMENT (of the abstract entered in Block 20, if different from Report)		
19. SUPPLEMENTARY NOTES This work sponsored by the Defense Nuclear Agency under RDT&E RMSS Code B344077462 J34HAXSX31111 H2590D.		
20. KEY WORDS (Continue on reverse side if necessary and identify by block number) Fatigue (Mechanics) Fiber Reinforcement Cumulative Fatigue Damage Military Facilities Hydrostatic Pressure Openings Concrete Underground Spheres Probabilistic Methodology		
21. ABSTRACT (Continue on reverse side if necessary and identify by block number) There has been conflicting evidence about the significance of low-cycle fatigue damage inflicted on deep-underground rock openings subjected to ground shock from sequential, multiple bursts of nuclear weapons. Few tests have been made. This investigation comprises tests and data analyses to further examine the question. Nine hollow concrete spheres, reinforced with steel-wire fibers, were instrumented and tested under cyclic, hydrostatic loads in a pressure vessel. over		

407844

LB

UNCLASSIFIED

SECURITY CLASSIFICATION OF THIS PAGE(When Data Entered)

20. ABSTRACT (Continued)

Strain gages were mounted on the inner surface and inside the wall to detect the onset of in-plane cracking and to monitor the progressive degradation of the test specimens. Cylinders cast at the same time as the spheres were tested to define the material properties. Fatigue curves were prepared from the cyclic test data and a power law equation was fitted. From the strain-gage data, pressure/strain plots and cyclic histories were constructed. The growth of strain with cycles was analyzed.

A methodology was then developed for designing a failure mode to meet a survivability goal or to assess the survivability of a design. The failure mode resistance was assumed to undergo degradation under repeated loads according to the fatigue equation. The methodology differs from standard methods of designing under random fatigue in that (1) it is structured for 1 to 100 load applications and (2) it reduces to the correct solution for the 1-load case. Sample problems illustrate the procedure. It was concluded that low-cycle fatigue needs to be considered in the survivability analysis of rock openings subjected to multiple attack.

UNCLASSIFIED

SECURITY CLASSIFICATION OF THIS PAGE(When Data Entered)

## PREFACE

For the project reported herein, Agbabian Associates (AA) performed the analytical work and the Civil Engineering Laboratory (CEL), Naval Construction Battalion Center, Port Hueneme, California performed the experimental work, under separate contracts from the Defense Nuclear Agency, Washington, D.C. AA was responsible for coordinating and interpreting the test data and incorporating these data into a design methodology. The AA effort was funded under Contract No. DNA001-77-C-0245. The contracting officer's representative (COR) for DNA was Lt. Col. John Galloway.

C.F. Bagge was the Program Manager; and M.B. Balachandra was the Project Engineer. This report was written by M.B. Balachandra, C.F. Bagge, and H.H. Haynes, with the assistance of J.D. Radler. Significant contributions were made by Y.C. Lee throughout the project and by H.S. Ts'ao and A. Der-Kiureghian during the probabilistic analysis.

For the experimental program at CEL, H.H. Haynes was the Principal Investigator. Significant contributions were made by P.C. Zubiate, Jr.

ACCESSION NO.	
NTIS	Section <input checked="" type="checkbox"/>
DDC	Serial <input type="checkbox"/>
UNCLASSIFIED	<input type="checkbox"/>
JUSTIFICATION	
BY	
DISTRIBUTION/AVAILABILITY CODES	
Dist.	AVAIL. and/or SPECIAL
A	

## TABLE OF CONTENTS

<u>Section</u>	<u>Page</u>
1      INTRODUCTION . . . . .	7
1.1    PURPOSE . . . . .	7
1.2    BACKGROUND . . . . .	7
1.3    OBJECTIVES . . . . .	9
1.4    SCOPE . . . . .	9
1.5    RESPONSIBILITIES . . . . .	9
1.6    REPORT ORGANIZATION . . . . .	9
2      EXPERIMENTAL PROGRAM . . . . .	11
2.1    OBJECTIVE . . . . .	11
2.2    APPROACH . . . . .	11
2.3    BACKGROUND . . . . .	11
2.3.1    Lamé Solution for Hollow Spheres . . . . .	11
2.3.2    Failure Modes of Hollow Spheres . . . . .	12
2.4    TEST SPHERES . . . . .	14
2.5    INSTRUMENTATION SYSTEM . . . . .	14
2.6    TEST MATRIX . . . . .	15
2.7    PRESSURE VESSEL . . . . .	16
2.8    TEST PROCEDURE . . . . .	16
2.9    MATERIAL PROPERTY CONTROL TESTS . . . . .	16
2.10    TECHNICAL RISKS . . . . .	17
2.10.1    Epoxy Joint . . . . .	17
2.10.2    Size Effect . . . . .	17
3      EXPERIMENTAL RESULTS . . . . .	25
3.1    MATERIAL PROPERTY TESTS . . . . .	25
3.2    SINGLE-LOAD IMPLOSION TESTS . . . . .	25
3.2.1    Implosion Pressures . . . . .	25
3.2.2    Strains . . . . .	26
3.2.3    Failures . . . . .	26
3.3    CYCLIC-LOAD IMPLOSION TESTS . . . . .	26
3.3.1    Implosion Pressure versus Number of Cycles . .	26
3.3.2    Strains . . . . .	27
3.3.3    Failures . . . . .	27
4      TEST DATA ANALYSIS: SINGLE-LOAD IMPLOSION TESTS . . . . .	43
5      TEST DATA ANALYSIS: CYCLIC-LOAD IMPLOSION TESTS . . . . .	47
5.1    FATIGUE EQUATION . . . . .	47
5.2    STRAIN GROWTH WITH CYCLES . . . . .	48
5.3    SPATIAL STRAIN DISTRIBUTION . . . . .	49
6      DESIGN/ASSESSMENT METHODOLOGY . . . . .	59
6.1    INTRODUCTION . . . . .	59
6.2    SURVIVABILITY BOUNDS . . . . .	59
6.3    PROBABILITY OF SURVIVAL OF THE N-TH APPLICATION OF THE LOAD, $P(X_n > Z_n)$ . . . . .	60

TABLE OF CONTENTS (Continued)

<u>Section</u>		<u>Page</u>
6.4	FATIGUE DATA . . . . .	61
6.5	RESISTANCE $X_n$ . . . . .	62
6.6	ILLUSTRATIVE EXAMPLES . . . . .	64
6.6.1	Analysis . . . . .	64
6.6.2	Design . . . . .	68
7	SIGNIFICANCE OF LOW-CYCLE FATIGUE FOR ROCK OPENINGS/ REINFORCEMENT . . . . .	75
8	CONCLUSIONS . . . . .	77
9	REFERENCES . . . . .	79

APPENDIX

A	SPECIMEN PREPARATION . . . . .	81
B	CYLINDER TEST DATA . . . . .	91
C	STRAIN DATA FROM SINGLE-LOAD IMPLOSION TESTS . . . . .	99
D	DESCRIPTION OF FAILURES OF TEST SPECIMENS . . . . .	107
E	STRAIN DATA FROM CYCLIC LOAD TESTS . . . . .	121
F	REVIEW OF LOW-CYCLE FATIGUE DATA ON ROCK AND CONCRETE . . . . .	135
G	SYMBOLS AND NOTATIONS . . . . .	143

## LIST OF ILLUSTRATIONS

<u>Figure</u>		<u>Page</u>
2-1 Hollow-sphere notation . . . . .	20	
2-2 Typical test sphere . . . . .	21	
2-3 Test-specimen hemisphere mold, disassembled . . . . .	22	
2-4 Test-specimen hemisphere mold, assembled and ready for concrete pouring . . . . .	22	
2-5 Test specimen being lowered into pressure vessel . . . . .	23	
3-1 Pressure/strain data for Sphere 2 . . . . .	34	
3-2 Failure of Sphere 3 . . . . .	36	
3-3 Pressure/strain data from cyclic test of Sphere 5 . . . . .	38	
3-4 Failure of Sphere 8 . . . . .	41	
5-1 Fatigue plot of cyclic test pressure $P$ . . . . .	53	
5-2 Fatigue plot of normalized pressure $P/\bar{P}_{im}$ . . . . .	54	
5-3 Growth of peak strain with cycles in Spheres 7, 8, and 9 . . . . .	55	
5-4 Distribution of hoop strain . . . . .	57	
6-1 Probability that the mode survives the $Z_n$ load . . . . .	72	
6-2 Illustrative regression lines of low-cycle fatigue data . . . . .	73	
6-3 Degradation of mean resistance with repeated loading (Eq. 6-11). . . . .	74	

LIST OF TABLES

<u>Table</u>		<u>Page</u>
2-1	Test matrix . . . . .	18
2-2	Test cylinders . . . . .	19
3-1	Checkout-sphere cylinder test data: Single-load tests . . . . .	28
3-2	Checkout-sphere cylinder test data: Double-load tests . . . . .	29
3-3	Single-load implosion test results . . . . .	30
3-4	Pressurization rate . . . . .	31
3-5	Mean peak and minimum pressures during cyclic-load tests . . . . .	32
3-6	Cyclic-load implosion test results . . . . .	33
4-1	Single-load implosion test data analysis . . . . .	45
5-1	Mean peak strains . . . . .	50
5-2	Ratio of failure strain to first-cycle strain for steel-mounted gages in cyclic load tests . . . . .	51
5-3	Variability of strains in Spheres 1 to 6 . . . . .	52
5-4	Circumferential variation of average strains . . . . .	52
6-1	First-order approximation of means and COVs (Ref. 18) . . . . .	71

SECTION 1  
INTRODUCTION

1.1 PURPOSE

The investigation reported herein provides data for the design of deep-underground rock openings/reinforcement subjected to ground shock arising from nuclear-weapon attacks comprising sequential, multiple bursts.

1.2 BACKGROUND

Deception, duplication, dispersion, nomadization,<sup>\*</sup> reconstitution,<sup>†</sup> and hardening of prime mission materiel/personnel are approaches that can be used to achieve a survival capability against a nuclear-weapon attack. A subsystem is said to be hardened if it is designed to *directly* resist and mitigate the weapon effects. Most of the hardening requirements are generally allocated to the subsidiary facilities, which house, support, and protect the prime mission materiel/personnel.

Achieving superhard facilities by deep basing/burial has been the subject of DoD attention for more than two decades. Attention has focused on the facility cost driver--the rock openings/reinforcement.

A number of attack scenarios can be postulated to defeat the rock openings/reinforcement. One such scenario comprises sequential bursts of state-of-the-art weapons and has as its objective a ground-shock-induced low-cycle fatigue defeat of the rock openings/reinforcement. Unfortunately, the low-cycle fatigue defeat of rock openings/reinforcement has received little attention to date. In fact, there is disagreement in the technical community as to whether multiple bursts lead to a sufficiently significant accumulation of damage that low-cycle fatigue needs to be considered.

---

<sup>\*</sup>To nomadize is to keep changing the targeting address.

<sup>†</sup>To reconstitute is to reestablish surface links with the aid of outside and/or internal resources.

For example, Agbabian-Jacobsen Associates\* analytically investigated the ground-shock-induced low-cycle fatigue of the rock surrounding a steel-lined penetration to a deep-underground rock opening (Refs. 1 and 2). The mathematical model of the rock incorporated a moving yield surface to simulate strength degradation. Laboratory data obtained from noncyclic testing of intact, sawed, and naturally fractured rock specimens made up the data base for the model. In spite of numerical problems, the results indicated that the designer should address low-cycle fatigue.

On the other hand, Stanford Research Institute has experimentally investigated the low-cycle fatigue of small-scale models of steel-lined rock openings (Ref. 3). The specimens were cylinders 4 in. (102 mm) in diameter by 3 in. to 6 in. (76 mm to 152 mm) high, made of rock-simulating grout. The tunnel was simulated by a 5/8-in. (15.9 mm) dia. hole transverse to the cylinder axis. The steel lining had a thickness of 0.025 in. (0.64 mm). The closure of the opening showed from 5% to 10% increase under two load cycles. Damage was thus found to accumulate, but was judged by the investigators not to be significant.

An upcoming underground nuclear test, the DIABLO HAWK Event, will reload the structures used in the Structures Add-on Experiment of the MIGHTY EPIC Event (Ref. 4). This double ground-shock loading of the MIGHTY EPIC structures affords the community a rare opportunity to observe the effects of multiple loading under field conditions.

Post-MIGHTY EPIC, one of the 6-ft O.D. (1.83 m) hollow spherical structures (AY-11) was removed from the test bed and tested under hydrostatic loading in a pressure vessel (Ref. 4). The test subjected the sphere to repeated loading at a pressure level that was high enough to induce some inelasticity but not catastrophic failure. The sphere failed after five cycles of loading, indicating the lethality of low-cycle fatigue. Strains monitored during the tests also gave evidence of the progressive deterioration of the sphere.

The hydrostatic test of Sphere AY-11 pointed up the value of laboratory tests of hydrostatically loaded structures and prompted the present program.

---

\*Formerly the name of Agbabian Associates until 1972.

### 1.3 OBJECTIVES

This investigation has three objectives:

- (1) Generate low-cycle fatigue data.
- (2) Develop a design methodology that embraces low-cycle fatigue data.
- (3) Assess the significance of low-cycle fatigue (multiple bursts) on the design of deep-underground rock openings/reinforcement.

### 1.4 SCOPE

The scope of this investigation encompasses:

- a. Addressing up to one-hundred cycles of load, or the equivalent of up to one-hundred sequential bursts.
- b. Conducting low-cycle fatigue tests on nine 16-in. O.D. (406 mm), random-steel-wire-reinforced, hollow concrete spheres subjected to hydrostatic pressure.
- c. Developing first-order probabilistic design methodology that incorporates low-cycle fatigue data.

### 1.5 RESPONSIBILITIES

The experimental portions of this investigation were conducted by the Civil Engineering Laboratory, Naval Construction Battalion Center, Port Hueneme, California. The rest of the investigation was conducted by Agbabian Associates.

### 1.6 REPORT ORGANIZATION

Section 2 describes the experimental program, the results of which are reported in Section 3. Test data are analyzed in Sections 4 and 5. Section 6 develops a probabilistic design/analysis methodology that uses low-cycle fatigue data. Section 7 addresses the significance of low-cycle fatigue for rock openings/reinforcement. Conclusions are given in Section 8. Section 9 lists the references cited in the text. Additional details and data from the experimental program are

presented in Appendixes A through E, whereas data from several investigations of low-cycle fatigue behavior of rock and concrete are reviewed in Appendix F. Symbols used throughout the report are defined in Appendix G. Tables and figures are grouped at the end of each section.

SECTION 2  
EXPERIMENTAL PROGRAM

2.1 OBJECTIVE

The objective of the experimental program was to generate low-cycle fatigue data that relate to ground-shock loading of deep-underground rock openings/reinforcement.

2.2 APPROACH

Scaled models of the MIGHTY EPIC Event spherical structures were subjected to cyclic, hydrostatic loading. This approach allows for the testing of a number of specimens at a modest cost and provides insight into the probable performance of the MIGHTY EPIC spheres under the forthcoming DIABLO HAWK loading.

2.3 BACKGROUND

CEL has extensive experience in the noncyclic, hydrostatic testing of plain-concrete hollow spheres and cylinders (Refs. 5 through 12). In addition to investigating the basic strength of these structures, CEL has also investigated the effects of penetrations, polymer-impregnated concrete, and steel-liner reinforcement. The basic-strength investigations are pertinent to the present program and are reviewed below.

2.3.1 Lamé Solution for Hollow Spheres

For thick, elastic, hollow spheres under external hydrostatic pressure, the classical Lamé theory (Ref. 13) gives the hoop stress  $\sigma_\phi(R)$ <sup>x</sup> and the radial stress  $\sigma_R(R)$  at radius  $R$  (see Fig. 2-1) as

$$\sigma_\phi(R) = \frac{R_o^3(1 + R_i^3/2R_o^3)}{R_o^3 - R_i^3} P \quad (2-1)$$

$$\sigma_R(R) = \frac{R_o^3(1 - R_i^3/R_o^3)}{R_o^3 - R_i^3} P \quad (2-2)$$

<sup>x</sup>Compressive stresses and strains are considered positive throughout this report.

and the corresponding strains  $\epsilon_\phi(R)$  and  $\epsilon_R(R)$  as

$$\epsilon_\phi(R) = \frac{1}{E} \frac{1}{1 - (R_i/R_o)^3} \left\{ 1 - 2v + (1 + v) \frac{R_i^3}{2R^3} \right\} P \quad (2-3)$$

$$\epsilon_R(R) = \frac{1}{E} \frac{1}{1 - (R_i/R_o)^3} \left\{ 1 - 2v - (1 + v) \frac{R_i^3}{R^3} \right\} P \quad (2-4)$$

where  $R_i, R_o$  = inside and outside radius,  $P$  = external pressure,  $E$  = Young's modulus, and  $v$  = Poisson's ratio.

Equations 2-1 through 2-4 show that at the inner periphery, where  $R = R_i$ , the hoop strain attains its maximum value, the radial strain  $\epsilon_R$  is tensile, and the radial stress vanishes, since this is a free surface. The state of biaxial compression and the tensile radial strain cause failure to start at the inner periphery.

### 2.3.2 Failure Modes of Hollow Spheres

The CEL experimental investigations have identified two modes of failure exhibited by hollow concrete spheres under external hydrostatic compression:

(1) "in-plane cracking," or the formation of cracks along spherical surfaces (i.e., delamination) and (2) "implosion," or subsequent catastrophic failure. The in-plane cracking mode of failure generally starts at the inner surface of the sphere. It is detected by an abrupt decrease in strain gage readings while the applied external pressure continues to increase. Such a behavior presumably signifies that the local region around the gage has cracked and is unable to carry the load although the entire sphere is still structurally competent and able to sustain an increase in pressure. Implosion usually manifests itself as the shear failure of a section of the wall, resulting in the formation of a hole with or without subsequent collapse of the sphere.

The experimental data show that the external pressures at the occurrences of both modes of failure are governed by the ratio of the wall thickness of the sphere to its diameter and by the unconfined compressive strength of the material. In particular, investigations on plain-concrete spheres led to the following design formulas (Ref. 6).

In-Plane Cracking<sup>\*</sup>:

$$P_{p1} = 0.9 f'_c \left\{ 1 - \left( 1 - \frac{2t}{D_o} \right)^3 \right\} \quad (2-5)$$

Implosion<sup>\*</sup>:

$$P_{im} = \lambda k f'_c \left\{ 1 - \left( 1 - \frac{2t}{D_o} \right)^2 \right\} \quad (2-6)$$

where

$P_{p1}$  = External pressure at in-plane cracking, i.e., pressure at the first indication of in-plane cracks

$P_{im}$  = External pressure at implosion

$f'_c$  = Unconfined compressive strength of concrete

$t$  = Thickness of sphere wall

$D_o$  = Outside diameter of sphere

$\lambda$  = 1, for short-term, noncyclic loading  
 $13.5t/D_o$

$k$  =  $1.22 + 0.014e$

For the geometry selected here ( $t/D_o = 0.1875$ , see Sec. 2.4), Equations 2-5 and 2-6 are manipulated to produce

$$\frac{P_{p1}}{f'_c} = 0.68 \quad (2-7)$$

$$\frac{P_{im}}{f'_c} = 0.85 \quad (2-8)$$

$$\frac{P_{im}}{P_{p1}} = 1.25 \quad (2-9)$$

---

<sup>\*</sup>Equation 2-5 is derived from the Lamé Equation 2-1, whereas Equation 2-6 is based on the average wall stress at implosion,  $\sigma_{im}$  (Ref. 6).

$$\frac{\sigma_{im}}{f'_c} = \frac{P_{im}/f'_c}{1 - (1 - 2t/D_o)^2} = 1.4^* \quad (2-10)$$

#### 2.4 TEST SPHERES

Each test specimen was a 16-in. (406 mm) O.D., random-steel-wire-reinforced concrete sphere with a 3-in. (76 mm) thick wall.<sup>†</sup> A typical test sphere is shown in Figure 2-2. One and one-half percent (by volume) of fiber was added to the concrete.<sup>‡</sup>

The concrete was prepared with Portland cement and local aggregate. The mix, similar to that used for the MIGHTY EPIC spheres, was designed to produce a 7-day unconfined compressive strength of 8300 psi (57.2 MPa). It is described in Appendix A.

Each sphere was cast one hemisphere at a time with the molds shown in Figures 2-3 and 2-4. The top hemisphere was cast with a hole to receive the instrumentation-cable penetrator (Fig. 2-2). Steel strips carrying weldable strain gages were attached to the inner mold of the bottom hemisphere before casting. The hemispheres were cured in a fog room at 73°F (22.8°C), 100% RH, for 14 days, followed by curing at 73°F (22.8°C), 50% RH, for another 28 days. At the end of the 42-day period, the hemispheres were moved outside. Gages were mounted on the internal surfaces of the bottom hemispheres. The inner surfaces of both hemispheres were waterproofed. The test specimens were assembled by bonding the hemispheres with epoxy. These operations are described in more detail in Appendix A.

#### 2.5 INSTRUMENTATION SYSTEM

Strain gages were used (1) to detect the onset of in-plane cracking, and (2) to monitor progressive degradation of the test specimens in cyclic tests.

---

\*  $\sigma_{im}$  represents the average stress across the wall at implosion.

<sup>†</sup> The size of the spheres was fixed by the availability of existing molds. (The MIGHTY EPIC spheres measured 6-ft [1.83 m] O.D. with 1-ft [0.305 m] thick walls.)

<sup>‡</sup> The same percentage was used for the MIGHTY EPIC spheres.

In order to minimize the cost of fabrication, only one hemisphere was instrumented. Seven gages were mounted on the lower hemisphere of each test specimen, as shown in Figure 2-2.

Three of the gages were mounted directly on the inside concrete surface. These were intended to detect the onset of in-plane cracking. The remaining four gages were weldable strain gages mounted on steel strips embedded in the wall of the test specimen close to the inner and outer surfaces (Fig. 2-2). This method of installing strain gages, which was also used for the MIGHTY EPIC spherical structures, ensures that strain data will continue to be recorded even after local failure of the concrete renders concrete-mounted gages inoperative. For cyclic loading tests, this is especially important because the concrete-mounted gages are expected to cease functioning after the first few cycles.

The hydrostatic pressure acting on the test sphere was measured by Bourdon pressure gages as well as by a second type of pressure transducer. Since the Bourdon gage is considered the more accurate of the two, the Bourdon recordings were used in all subsequent analyses.

During the cyclic tests, pressure and strain readings from all seven gages were recorded for subsequent data reduction. At approximately 10-cycle intervals, data were recorded on magnetic tape; during the interim cycles, data were recorded on paper tape for hand-plotting as needed.

## 2.6 TEST MATRIX

One checkout sphere\* and nine test spheres were fabricated. The test matrix is shown in Table 2-1. Each test concluded with implosion of the test sphere. The pressure levels for the cyclic tests, which were updated as the tests progressed, were selected so as to yield a range of cycles to failure.

\*The checkout sphere (listed as No. 10 in Table 2-1) was cast first and used for pretest experimentation.

## 2.7 PRESSURE VESSEL

The noncyclic and cyclic tests of the test spheres were conducted in the CEL Deep Ocean Simulation Laboratory's 18-in. (457 mm) dia. pressure vessel, which has a maximum capacity of 20,000 psi (138 MPa). The vessel is filled with water and pressurized by air-operated, positive displacement pumps. Figure 2-5 shows a typical test specimen being lowered into the pressure vessel.

## 2.8 TEST PROCEDURE

At the time of the test, the upper hemisphere was fitted with the steel penetrator, which connects to the pressure-vessel head and leads the strain-gage cables from the test sphere to the recording devices. All specimens from Sphere 3 onward were filled with water to lessen the violence of the implosions. The vent hole in the penetrator maintained the water at atmospheric pressure.

During unloading in the cyclic tests, a minimum pressure of a few hundred psi ( $\sim 1$  MPa) was maintained to keep the test sphere in compression and thereby prevent undue distress of the joint between the hemispheres.

## 2.9 MATERIAL PROPERTY CONTROL TESTS

Test cylinders for use in monitoring the concrete material properties were cast along with the checkout sphere. Unconfined compression tests were conducted twice: after seven days to verify the target strength of the concrete mix, and after curing. Some tests were instrumented with gages that measured axial and lateral strain. The resulting data were used to construct stress/strain curves and hence to determine Young's modulus and Poisson's ratio.

Cylinders were also cast and cured with each hemisphere of the nine test spheres. Cylinder strengths determined on the test day of each associated sphere were used in formulas analogous to Equations 2-5 and 2-6 to calculate each sphere's implosion strength.

The disposition of all the test cylinders is shown in Table 2-2. Results of the cylinder tests are discussed in Section 3.1 and Appendix B.

## 2.10 TECHNICAL RISKS

In planning the program, two technical risks were recognized:

- (1) The epoxy joint
- (2) The size effect

### 2.10.1 Epoxy Joint

There was concern that the equatorial epoxy joint binding the two hemispheres of a test specimen might precipitate the failure of the specimen. In previous noncyclic tests conducted by CEL, however, the epoxy joint posed no problem. To minimize the risk, the hydrostatic pressure was not allowed to drop to zero during the cyclic tests (see Sec. 2.8).\*

### 2.10.2 Size Effect

A technical question inherent in this investigation has been whether data from 16-in. (406 mm) O.D. test specimens could be extrapolated to the larger prototype structures (perhaps 40- to 80-ft [10 to 20 m] O.D.).

Budget constraints ruled out addressing size effect. However, CEL has previously determined that there is no significant size effect between 16-in. (406 mm) and 66-in. (1.7 m) O.D. plain-concrete test specimens subjected to non-cyclic loading (Refs. 5 and 11). Moreover, it is known that size effect is less pronounced in high-strength concrete (present program) than in conventional-strength concrete.

---

\*Although the MIGHTY EPIC spheres were integrally cast, we chose to use existing molds that had an equatorial joint. This also allowed the inside surface of the spheres to be instrumented.

Table 2-1. Test matrix.

<u>Test Sphere No.</u>	<u>Type of Test</u>
1	Single load
2	Single load
3	Single load
4	Single load
5	Cyclic load
6	Cyclic load
7	Cyclic load
8	Cyclic load
9	Cyclic load
10	Checkout specimen

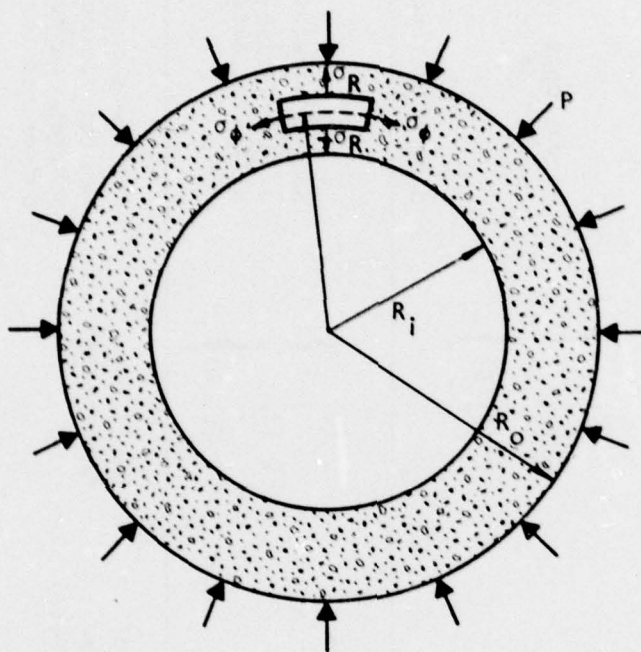
Table 2-2. Test cylinders.

Associated Sphere	Size	Quantity	Test Cylinder	Tests Performed	Remarks
Checkout (No. 10)	3" x 6" (76 mm x 152 mm)	12	3 (U) 2 (U)	7-day cure	
			2 (S)	42-day cure cycle identical to that of test spheres	
			2 (S, R)	3 held in reserve as backups	
			2 (U) 2 (S)	Same concrete mix used for 3" x 6" cylinders, but different batch	
	6" x 12" (152 mm x 305 mm)	6	2 (S)		
			2 (S, R)		
Nos. 1 to 9	3" x 6" (76 mm x 152 mm)	108 (6 per hemisphere)	54 (3 per hemisphere)	Cylinders cast from same batch as their associated test spheres, cured by same cycle, and tested the same day.	
				54 held in reserve as backups	

U = Uninstrumented

S = Instrumented

R = Repeated load: Loaded to 85% f<sub>u</sub>, unloaded, reloaded to failure



$\sigma_\phi(R)$ ,  $\epsilon_\phi(R)$ : Hoop Stress and Strain at Radius R

$\sigma_R(R)$ ,  $\epsilon_R(R)$ : Radial Stress and Strain at Radius R

Figure 2-1. Hollow-sphere notation.

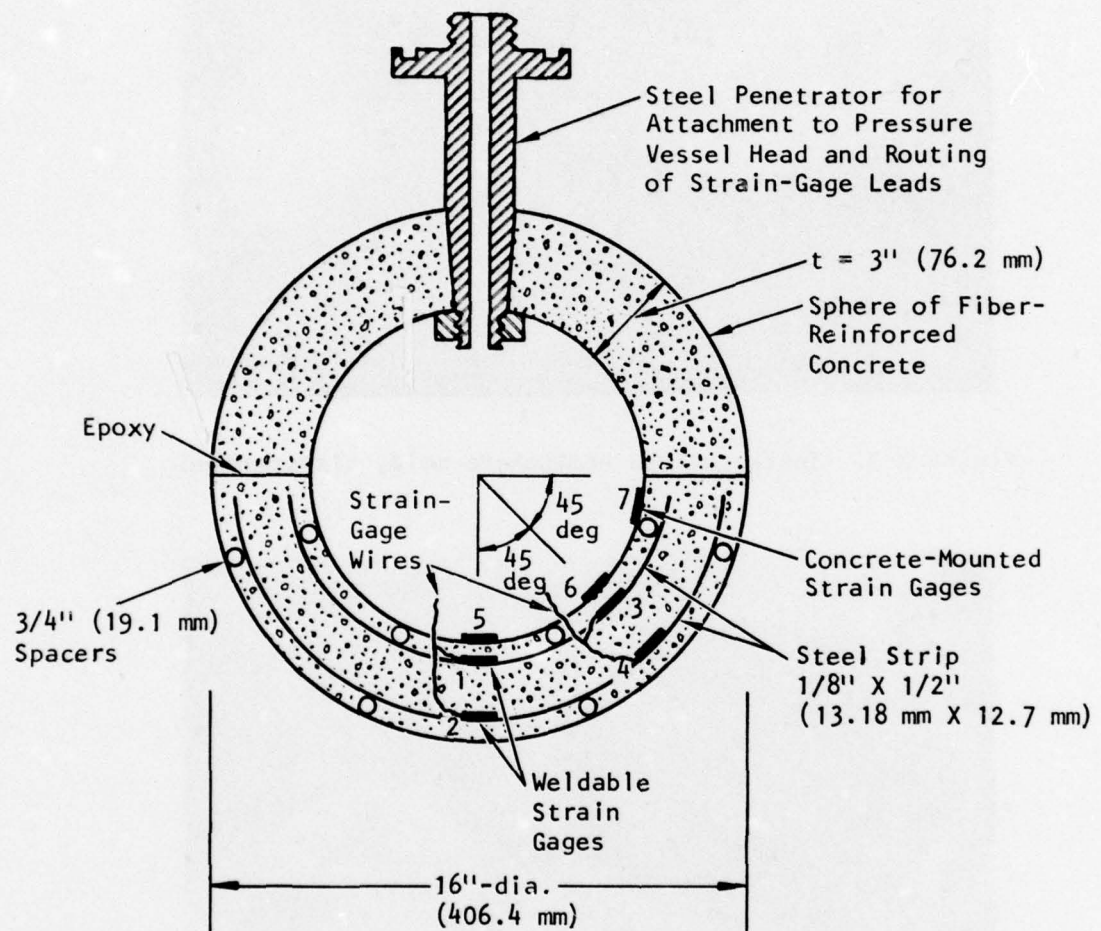


Figure 2-2. Typical test sphere.

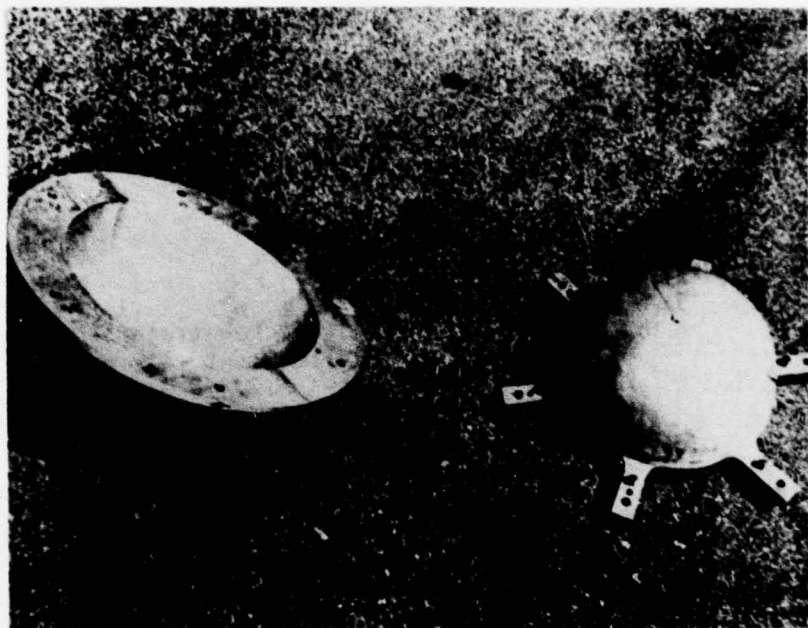


Figure 2-3. Test-specimen hemisphere mold, disassembled.

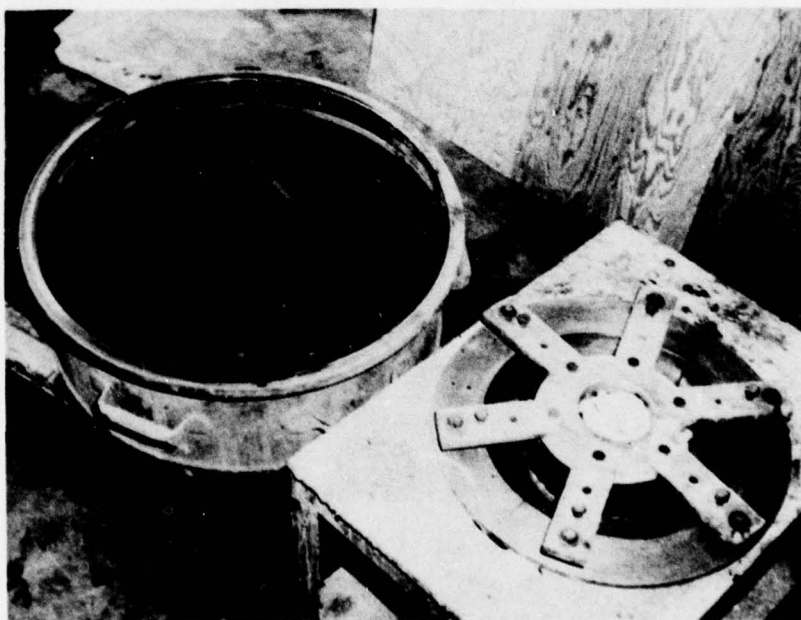


Figure 2-4. Test-specimen hemisphere mold, assembled and ready for concrete pouring.

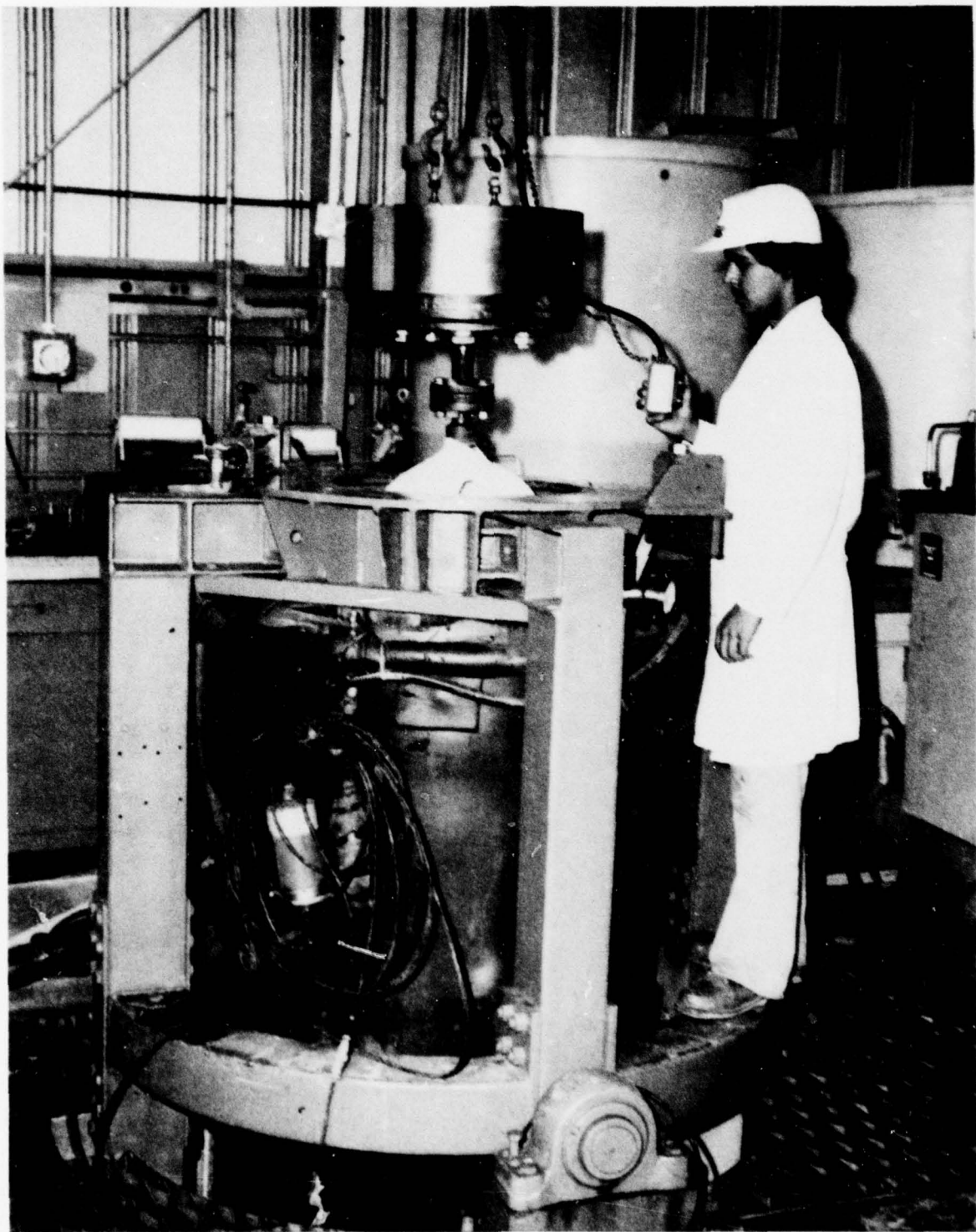


Figure 2-5. Test specimen being lowered into pressure vessel.

## SECTION 3

### EXPERIMENTAL RESULTS

#### 3.1 MATERIAL PROPERTY TESTS

The data from the single-load compression tests on four small and four large test cylinders\* associated with the checkout sphere (Sec. 2.9) are summarized in Table 3-1. Data from the double-load tests on the remaining four cylinders are in Table 3-2. Young's modulus and Poisson's ratio calculated from the first cycle in double-load tests are included in computing the mean and COV<sup>†</sup> shown in Table 3-1, whereas the mean strengths are computed from the single-load tests only. Stress/strain curves from the instrumented cylinder tests are shown in Appendix B.

The mean unconfined compressive strength obtained from the 54 3-in. x 6-in. (76 mm x 152 mm) cylinders associated with the other nine test specimens is 10,125 psi (69.8 MPa), with a COV of 8% (see App. B).

The comparable mean Young's modulus and mean 28-day strength of the MIGHTY EPIC spherical structures concrete were  $4.85 \times 10^6$  psi (33 GPa) and 10,060 psi (69 MPa), respectively. Thus, the concrete of the present program exhibited a mean stiffness and a mean strength that are 58% and 100.1% of the MIGHTY EPIC spheres. The large disparity in the stiffnesses is attributed to the difference in the aggregates used in the concretes.

#### 3.2 SINGLE-LOAD IMPLOSION TESTS

##### 3.2.1 Implosion Pressures

The results of the single-load implosion tests of Spheres 1 through 4 are shown in Table 3-3. The pressurization rate for all sphere tests is shown in Table 3-4.

\*The small cylinders, cast from the same batch as the checkout sphere, were 3 in. by 6 in. (76 mm by 152 mm). The large cylinders, cast from the same concrete mix but a different batch, were 6 in. by 12 in. (152 mm by 305 mm).

†The abbreviation COV is used throughout this report to represent the coefficient of variation, defined as the ratio of the standard deviation to the mean. It is expressed as a percentage.

Sphere No. 1 exhibited an anomalous implosion occurring almost immediately after the development of in-plane cracks. The failure was highly localized and probably originated at an imperfection. Therefore, the implosion pressure of Sphere 1 has not been used in calculating the mean value of  $P_{im}$  (Table 3-3). However, the in-plane cracking pressure is considered acceptable and is included in calculating the mean value of  $P_{pl}$ .

### 3.2.2 Strains

The pressure versus strain data obtained for Sphere 2 are shown in Figure 3-1, along with a plot of pressure versus time. In-plane cracking, which is signaled by a decrease in strain accompanying an increase in pressure, is clearly shown by the three concrete-mounted gages (Nos. 5, 6, 7). The strain records of the other specimens are similar (see App. C).

### 3.2.3 Failures

Figure 3-2 shows the failure of Sphere 3. Drawings and photographs showing details of the failures of all the other test spheres are presented in Appendix D.

The failure of Sphere 1 was an oval hole measuring approximately 3/4 in. by 1/4 in. (19 mm by 6 mm) to a depth of about 1-1/4 in. (32 mm) from the outside surface and then flaring to approximately 4 in. (102 mm) in diameter. Apart from some crushing inside near the failure hole, there was little damage. The failure occurred in the bottom hemisphere in spite of the fact that the material properties tests indicated that the lower strength value was in the cylinders associated with the top hemisphere. The failure most probably originated at a local imperfection.

The failure of Sphere 2 was very violent. The failures of Spheres 3 and 4, which occurred in the bottom hemisphere, were unremarkable.

## 3.3 CYCLIC-LOAD IMPLOSION TESTS

### 3.3.1 Implosion Pressure versus Number of Cycles

Spheres 5 through 9 were subjected to cyclic loading. The mean peak and minimum pressures used are shown in Table 3-5. The pressure variations within a

test are considered insignificant. For analysis, the peak pressure is taken as the mean peak pressure, and the minimum pressure as zero.

The number of load cycles producing implosion is shown in Table 3-6.

### 3.3.2 Strains

Figure 3-3 shows the pressure versus strain data recorded during the cyclic tests of Sphere 5. The strain data from Spheres 6 through 9 are similar (see App. E).

These plots were obtained from data recorded on magnetic tape during the tests. For Spheres 5 and 6, the strain data cover most of the cycles; whereas for Spheres 7, 8, and 9, the data were taken at intervals of approximately 10 cycles, after the first few cycles.

### 3.3.3 Failures

In all the cyclic-test spheres, failure occurred in the bottom hemisphere, which was the weaker hemisphere in all except Spheres 7 and 8. However, the strength difference between the two halves of these specimens was small (App. B).

The failures of the cyclic-test spheres were generally more localized than those of the single-load test spheres. Figure 3-4 shows the failure of Sphere 8. Failures of the other specimens are shown in Appendix D. The failures did not seem to be influenced by the steel strips carrying strain gages (Fig. 2-2).

Although some of the failure holes abutted the epoxy joint, failures did not originate there. Furthermore, no anomalous or premature failure resulted from the presence of the joint. Thus, the epoxy joint did not prove to be a problem, as had been feared before the tests were made. It is possible, however, that the epoxy significantly influenced the strain distribution in the spherical specimens (Sec. 5.3).

Some of the failures were accompanied by two explosive sounds. The first of these occurred when the pressure was near its peak value, and probably was caused by a slippage in the failure zone. But the sphere evidently still had some resistance, which allowed partial pressure buildup on the next loading cycle before final implosion occurred.

Table 3-1. Checkout-sphere cylinder test data: Single-load tests.

Cylinder No.	Compressive Strength		Young's Modulus		Poisson's Ratio
	psi	(MPa)	$10^6$ psi	(GPa)	
Small Cylinders					
1	12,590	(86.8)	--	--	--
2	12,450	(85.8)	--	--	--
3	11,670	(80.5)	3.0	(20.7)	0.20
4	11,320	(78.1)	3.0	(20.7)	0.20
Mean	12,010	(82.8)	3.0*	(20.7*)	0.22*
COV, %	5.1		0*		13.3*
Large Cylinders					
7	11,160	(77.0)	--	--	--
8	10,890	(75.1)	--	--	--
9	11,050	(76.2)	2.6	(17.9)	0.20
10	11,180	(77.1)	2.7	(18.6)	0.23
Mean	11,070	(76.3)	2.68*	(18.5*)	0.20*
COV, %	1.2		3.6*		10.2*

\*The mean and COV (coefficient of variation) of Young's modulus and Poisson's ratio were computed by including the results of tests shown in Table 3-2.

Table 3-2. Checkout-sphere cylinder test data: Double-load tests.

Cylinder No.	Peak Stress on Cycle 1 psi	Compressive Strength (MPa)	Cycle 1		Cycle 2	
			Young's Modulus* $10^6$ psi (GPa)	Poisson's Ratio* .	Young's Modulus $10^6$ psi (GPa)	Poisson's Ratio Katio $10^6$ psi (GPa)
Small Cylinders						
5	9600 (66.2)	11,880 (81.9)	-- <sup>†</sup>	--	--	--
6	9600 (66.2)	12,240 (84.4)	3.0 (20.7)	0.25	2.9 (20.0)	0.26
Large Cylinders						
11	9300 (64.1)	10,910 (75.2)	2.8 (19.3)	0.20	2.5 (17.2)	0.29
12	9300 (64.1)	10,290 (71.0)	2.6 (17.9)	0.18	2.5 (17.2)	0.29

\* Included in computing mean and COV shown in Table 3-1

<sup>†</sup> Strain gage failure

Table 3-3. Single-load implosion test results.

Sphere No.	Measured Implosion Pressure $P_{im}$		Measured In-Plane* Cracking Pressure $P_{pl}$	
	ksi	(MPa)	ksi	(MPa)
1	7.46 <sup>†</sup>	(51.4)	7.28	(50.2)
2	11.80	(81.4)	8.01	(55.2)
3	11.76	(81.1)	7.72	(53.2)
4	13.26	(91.4)	9.02	(62.2)
Mean	12.27	(84.6)	8.01	(55.2)
COV, %	7.0		9.2	

\* In-plane cracking indicated by Gage Nos. 2, 7, 5, and 6, respectively, for Spheres 1, 2, 3, and 4 (see Figure 2-2 for gage identification).

<sup>†</sup> Anomalous failure, not included in computing mean value of  $P_{im}$ .

Table 3-4. Pressurization rate.

Sphere No.	Up-Cycle Pressurization Rate		Down-Cycle Pressurization Rate	
	psi/min	(MPa/s)	psi/min	(MPa/s)
1	3100	(0.356)	--	--
2	4000	(0.460)	--	--
3	5500	(0.632)	--	--
4	5100	(0.586)	--	--
5	4500	(0.517)	8200	(0.942)
6	6400	(0.736)	9500	(1.092)
7	5700	(0.655)	9000	(1.034)
8	6600	(0.758)	8800	(1.011)
9	5700	(0.655)	9200	(1.057)

Table 3-5. Mean peak and minimum pressures during cyclic-load tests.

Sphere No.	Peak Pressure				Minimum Pressure			
	Mean		Standard Deviation		Mean		Standard Deviation	
	psi	(MPa)	psi	(MPa)	psi	(MPa)	psi	(MPa)
5	9480	(65.4)	475	(3.28)	225	(1.55)	105	(0.72)
6	8440	(58.2)	80	(0.55)	265	(1.83)	35	(0.24)
7	6800	(46.9)	75	(0.52)	415	(2.86)	45	(0.31)
8	6830	(47.1)	30	(0.21)	385	(2.66)	30	(0.21)
9	6275	(43.3)	15	(0.10)	385	(2.66)	35	(0.24)

Table 3-6. Cyclic-load implosion test results.

Sphere No.	Mean Peak Test Pressure P		Cycles to Implosion, n
	ksi	(MPa)	
5	9.5	(65.5)	10
6	8.4	(57.9)	20
7	6.8	(46.9)	161
8	6.8	(46.9)	79
9	6.3	(43.4)	343

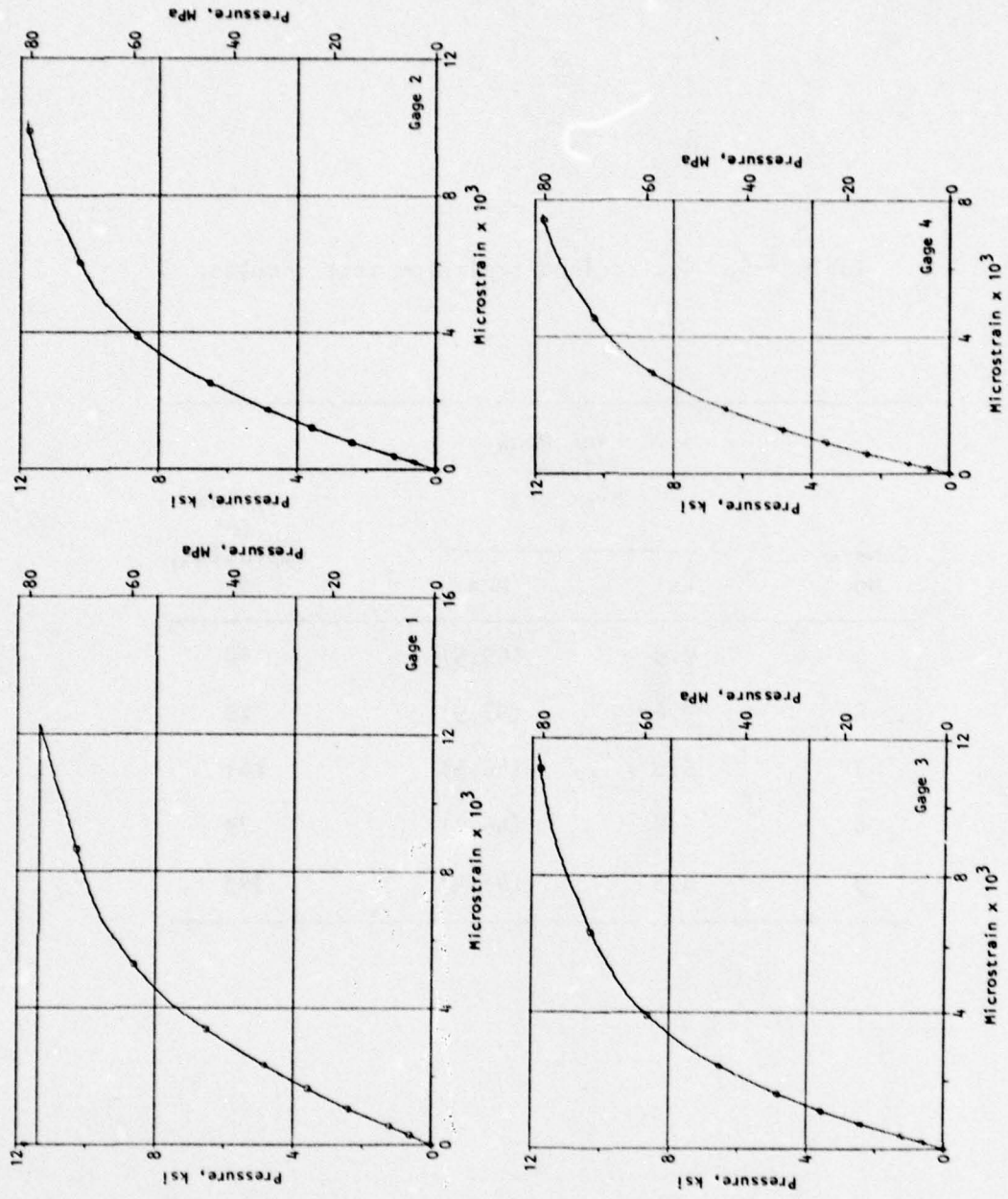


Figure 3-1. Pressure/strain data for Sphere 2.

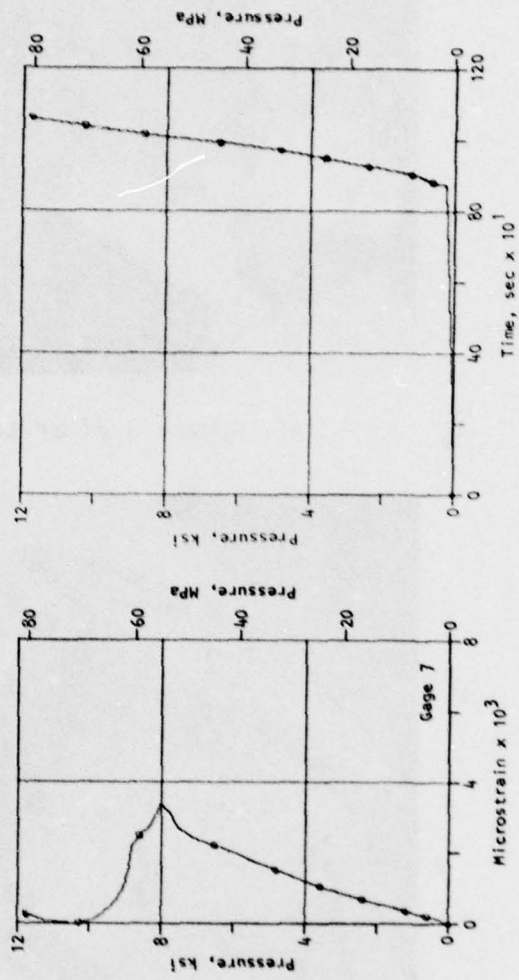
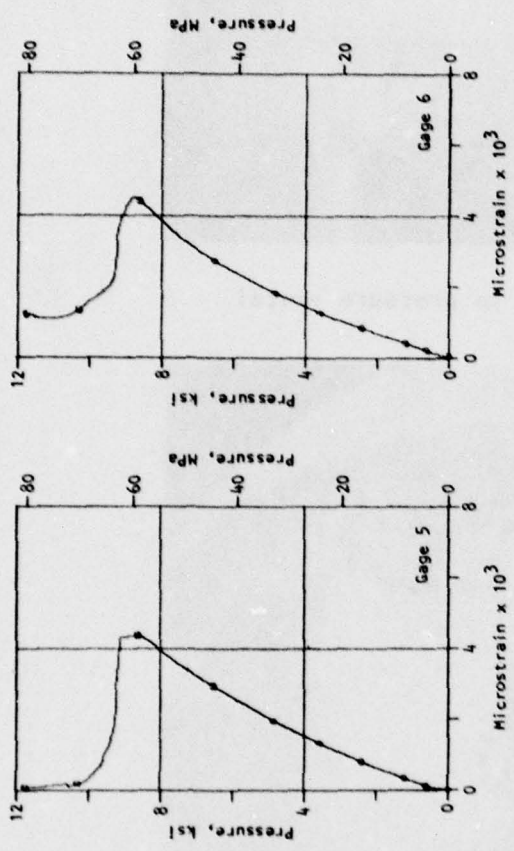
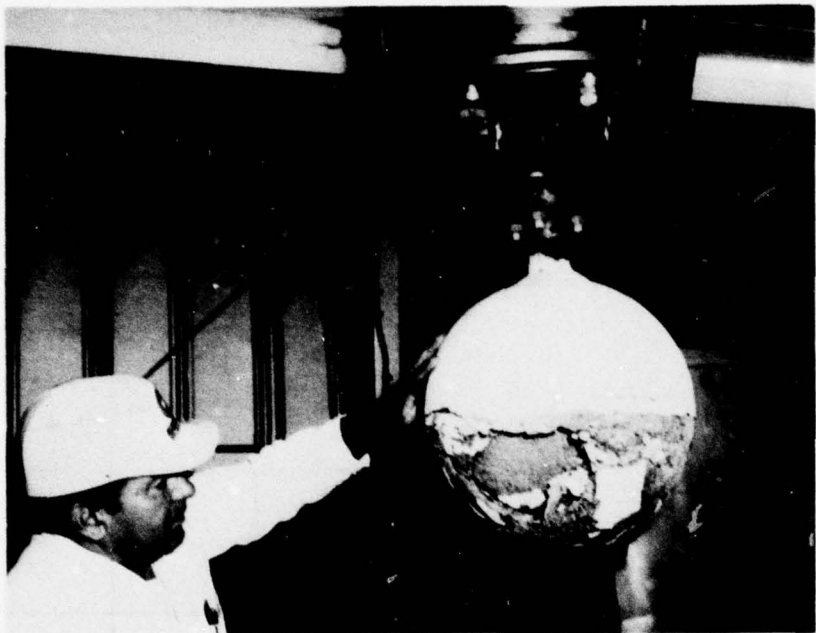
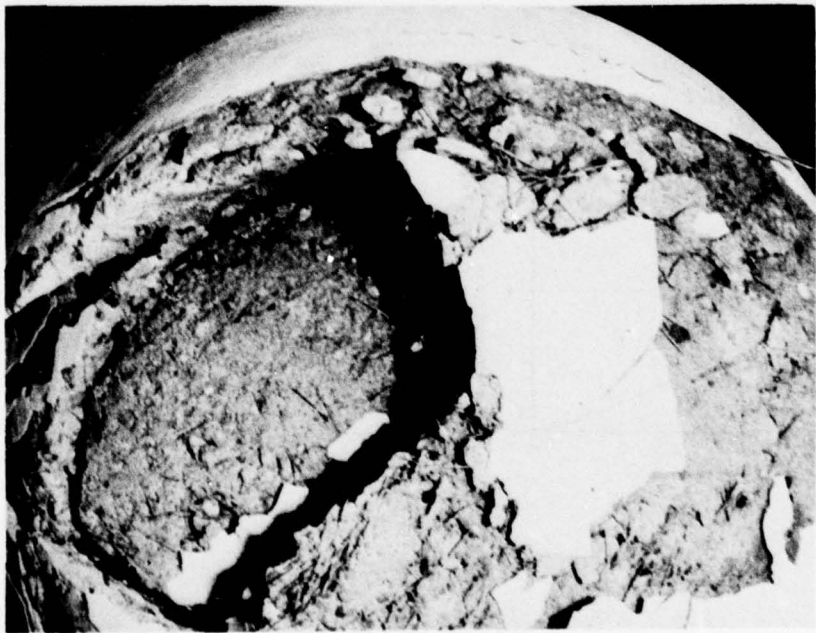


Figure 3-1. (Concluded).



(a) Sphere 3 after test in pressure vessel

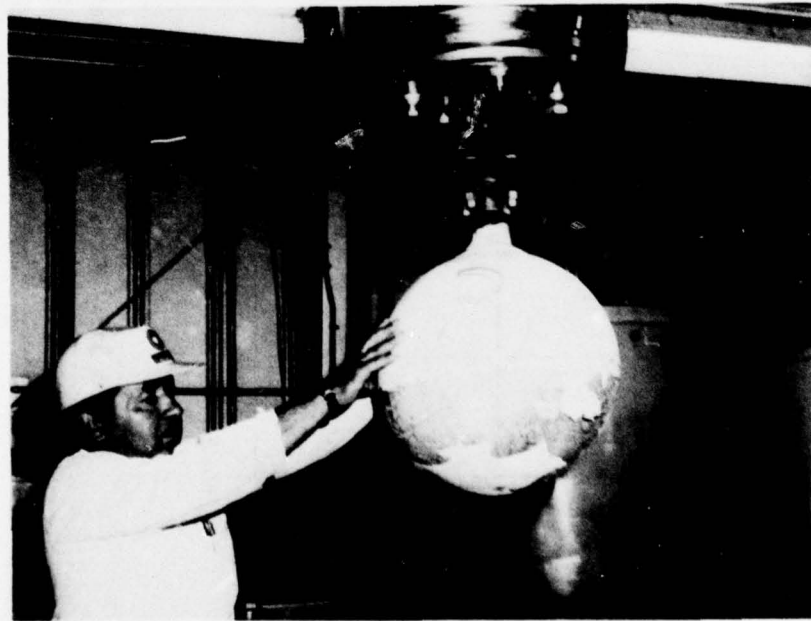


(b) Close-up view of implosion area

Figure 3-2. Failure of Sphere 3.



(c) Close-up view showing the wall cracks



(d) Outside view showing epoxy paint peeled off

Figure 3-2. (Concluded).

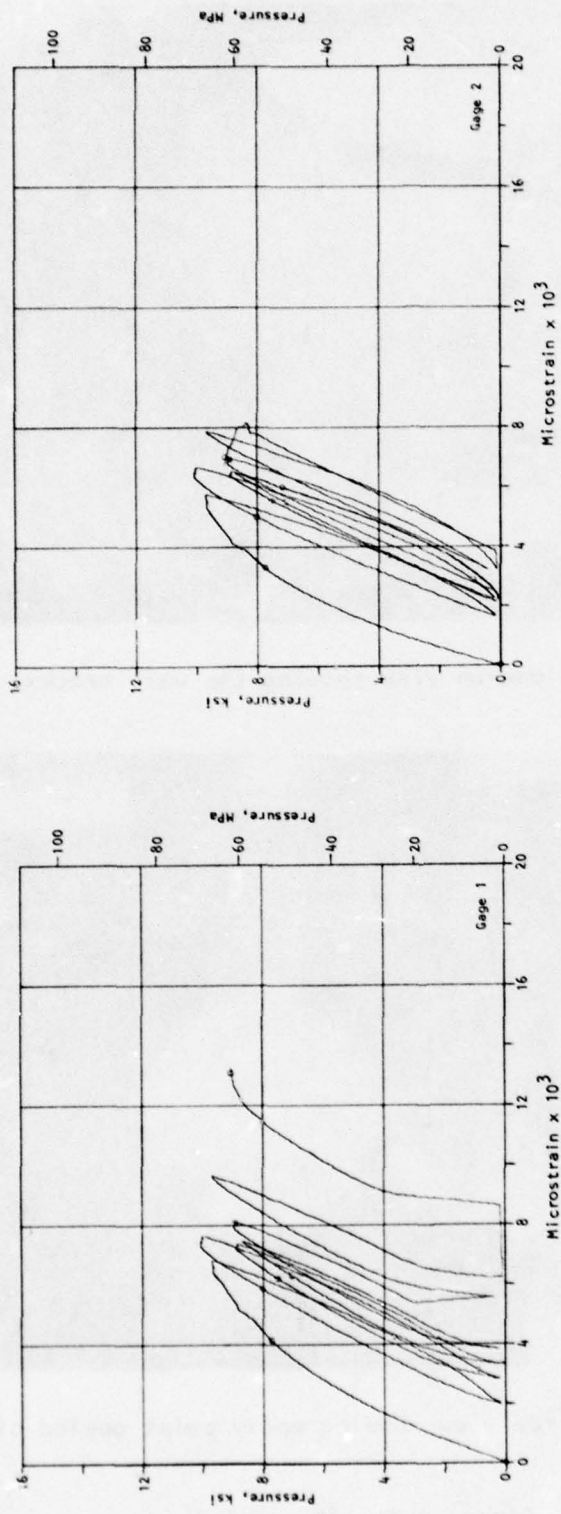


Figure 3-3. Pressure/strain data from cyclic test of Sphere 5.

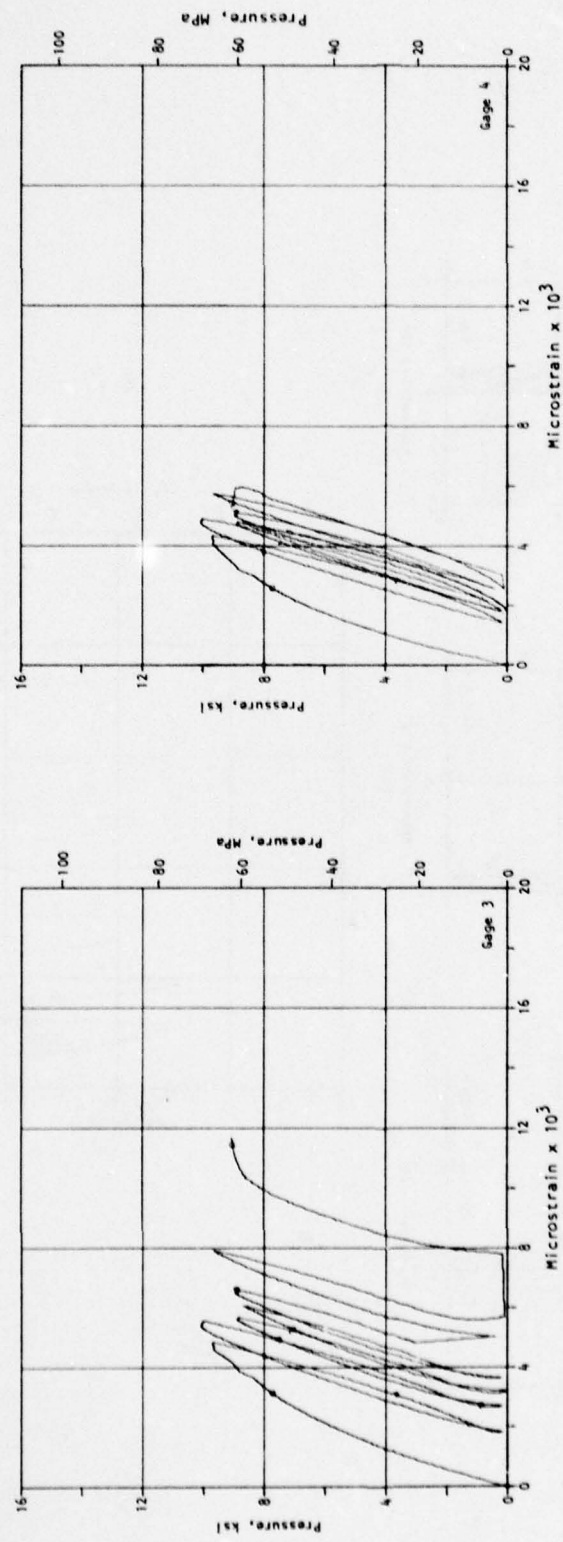


Figure 3-3. (Continued).

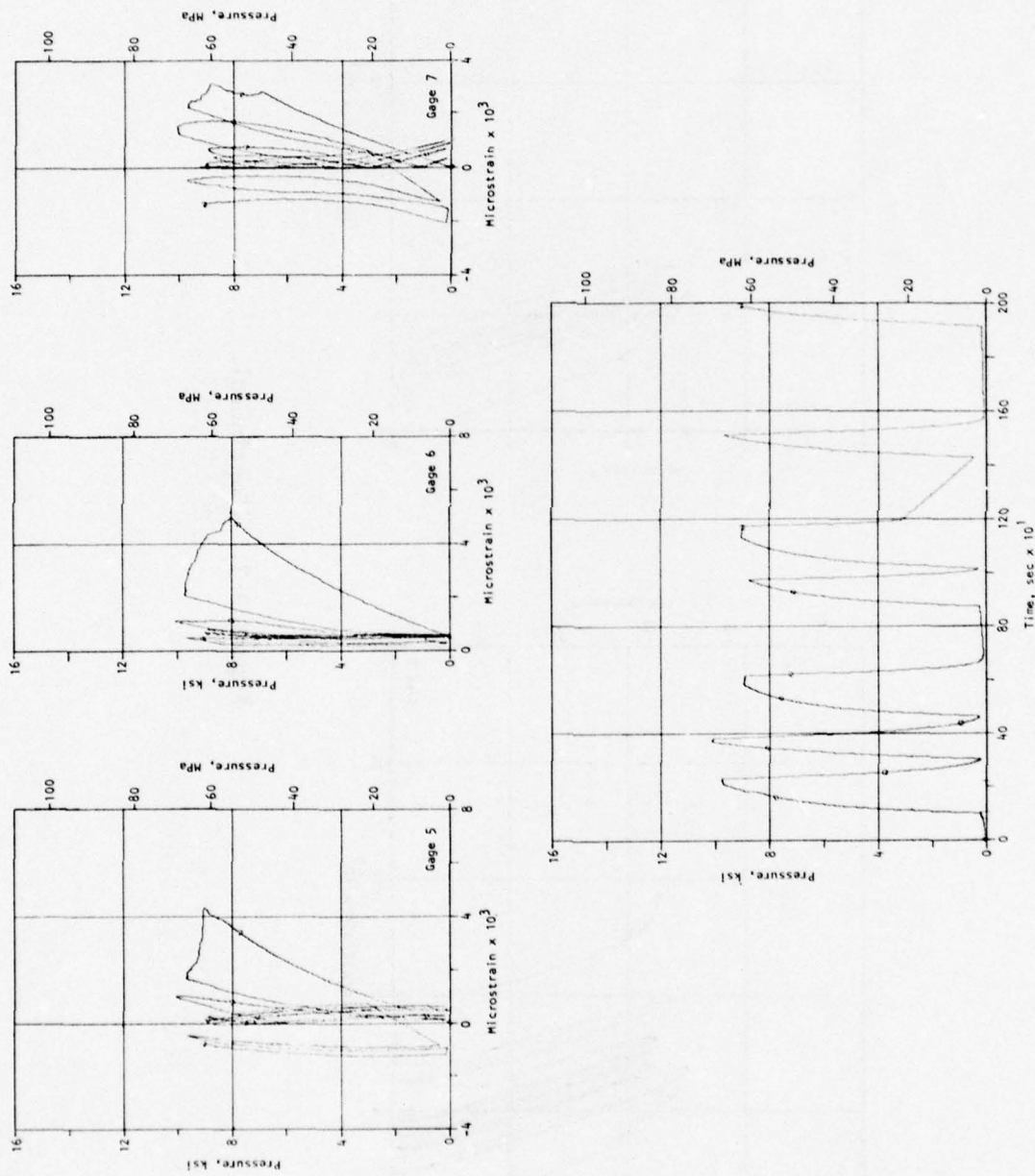
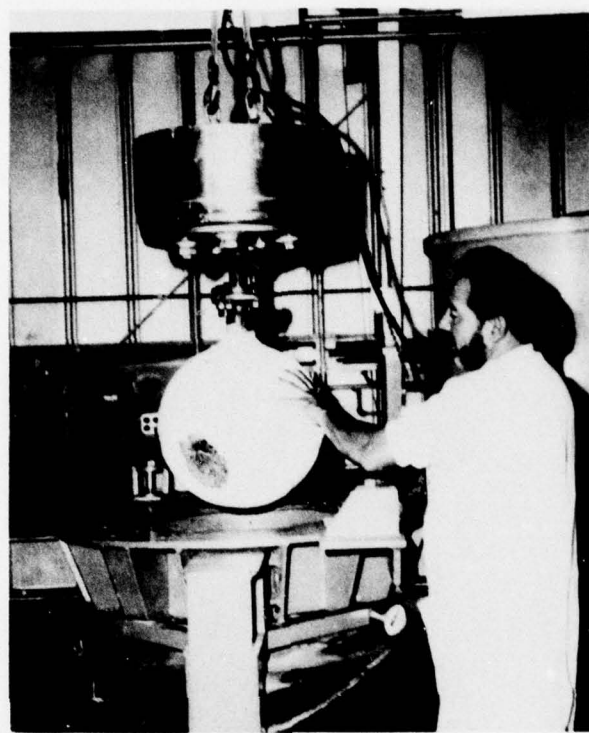
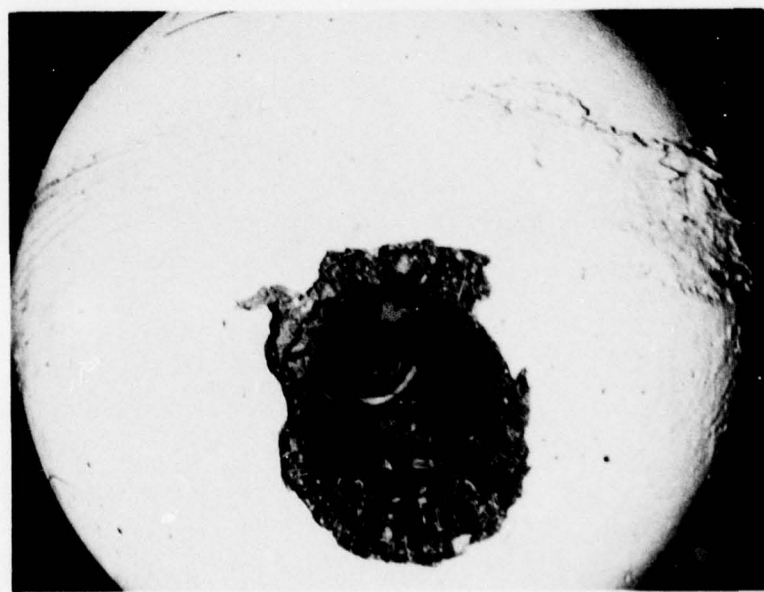


Figure 3-3. (Concluded).



(a) Sphere 8 being removed from pressure vessel



(b) Close-up view of failure

Figure 3-4. Failure of Sphere 8.

## SECTION 4

### TEST DATA ANALYSIS: SINGLE-LOAD IMPLOSION TESTS

Table 4-1 shows the analysis that has been performed on the single-load implosion test results. With reference to Table 4-1, the following observations are made:

- a. As evidenced by the low COVs, the tests were remarkably repeatable.
- b. The variability in  $P_{im}$  and  $P_{pl}$  is traceable to the variability in  $f'_c$ .
- c.  $P_{im}$  and  $P_{pl}$  are highly correlated, as evidenced by the small COV for  $P_{im}/P_{pl}$ .
- d. The mean ratio of  $P_{pl}/\bar{f}'_c = 0.87$  is to be compared to 0.68, which is derived from previous test results (see Eq. 2-7, Sec. 2.3.2).
- e. The mean ratio of  $P_{im}/\bar{f}'_c = 1.35$  is to be compared to 0.85, which is derived from previous test results (see Eq. 2-8, Sec. 2.3.2).
- f. The mean ratio of  $P_{im}/P_{pl} = 1.49$  is to be compared to 1.25, which is derived from previous test results (see Eq. 2-9, Sec. 2.3.2).
- g. The mean ratio of  $\sigma_{im}/\bar{f}'_c = 2.2^*$  is to be compared to 1.4, which is derived from previous test results (see Eq. 2-10, Sec. 2.3.2).

The disparities noted in Observations *d*, *e*, *f*, and *g* are apparently due to the effects of the random steel-wire fibers and to the effects of loading rate. It is speculated, for the following reasons, that the significant effect is the fibers. The previous test results were obtained using an average wall stress rate  $\dot{\sigma}_{im}$  of 160 psi/min (0.018 MPa/s), as compared with 6000 psi/min (0.69 MPa/s) for the present tests. However, other tests at CEL (Ref. 7) using  $\dot{\sigma}_{im} = 8000$  psi/min (0.92 MPa/s) showed implosion pressures only 13% higher than tests that used  $\dot{\sigma}_{im} = 800$  psi/min (0.092 MPa/s).

\*  $\sigma_{im}$  represents the average stress across the wall at implosion (see Eq. 2-10).

The higher value of the ratio  $P_{pl}/\bar{f}'_c$  in the present program shows that the in-plane cracks develop later than noted in the plain-concrete tests. Furthermore, the higher value noted for  $P_{im}/P_{pl}$  shows that the fiber-reinforced concrete has higher reserve strength left after the initiation of in-plane cracks. Thus, the oft-postulated role of random steel-wire fibers as inhibitors of crack growth is apparently reaffirmed here. The above two factors together lead to a ratio  $P_{im}/\bar{f}'_c$  that is 58% higher for the present program than for plain-concrete spheres (Ref. 6).

The ratio  $\sigma_{im}/\bar{f}'_c$  represents the strengthening induced by confinement in the test sphere. The present program shows that confinement and the use of fiber reinforcement together led to an average wall stress 2.2 times the failure stress in unconfined compression.

Table 4-1. Single-load implosion test data analysis.

Sphere No.	Mean Unconfined Compression Strength $\bar{f}_c^*$	Measured In-Plane Cracking Pressure $P_{p1}^†$	Measured Implosion Pressure $P_{im}$	Average Wall Stress at Implosion $\sigma_{im}$		$P_{p1}/\bar{f}_c^*$	$P_{im}/\bar{f}_c^*$	$P_{im}/P_{p1}$	$\sigma_{im}/\bar{f}_c^*$
				ksi	MPa				
1 <sup>‡</sup>	9.63 (66.4)	7.28 (50.2)	7.46 (51.4)	12.24	(84.4)	0.756	0.775	1.025	1.271
2	8.20 (56.5)	8.01 (55.2)	11.80 (81.4)	19.36	(133.5)	0.977	1.439	1.473	2.361
3	9.36 (64.5)	7.72 (53.2)	11.76 (81.1)	19.30	(133.1)	0.825	1.256	1.523	2.062
4	9.88 (68.1)	9.02 (62.2)	13.26 (91.4)	21.76	(150.0)	0.913	1.342	1.470	2.202
Mean		8.01 (55.2)	12.27 (84.6)	20.14	(138.9)	0.868	1.346	1.489	2.208
COV, %		9.2	7.0	7.0		11.2	6.8	2.0	6.8

<sup>\*</sup>Tabulated value is the lower of the two mean strengths obtained from tests on cylinders cast with each hemisphere (see App. B).

<sup>†</sup>In-plane cracking indicated by Gage Nos. 2, 7, 5, and 6, respectively, for Spheres 1, 2, 3, and 4 (see Fig. 2-2 for gage identification).

<sup>‡</sup>Anomalous failure; not included in computing means involving  $P_{im}$ .

## SECTION 5

### TEST DATA ANALYSIS: CYCLIC-LOAD IMPLOSION TESTS

#### 5.1 FATIGUE EQUATION

The data from Tables 3-3 and 3-6, along with the AY-11 data point (see Sec. 1.2), are plotted in Figure 5-1. The figure also shows the regression line\*

$$\bar{n} \bar{P}^{8.37} = 1.27 \times 10^9 (= 122), \quad (5-1)$$

where  $\bar{n}$  is the mean life at the mean pressure  $\bar{P}$  in ksi (MPa), and the  $\pm 2\sigma$  limits. The COV of  $\bar{P}$  for a given life  $\bar{n}$  is 5.1%. The relatively low life of the AY-11 sphere (see Fig. 5-1) could be due to its larger size, its prior damage, or its unique fabrication.†

The data shown in Figure 5-1 are replotted in Figure 5-2 after normalizing by the mean of the implosion pressures from Spheres 2, 3, and 4 (the specimens subjected to single loads). Also shown in Figure 5-2 is the regression line

$$\bar{n} (\bar{P}/\bar{P}_1)^{8.6} = 1.0 \quad (5-2)$$

where  $\bar{P}_1$  is the mean implosion pressure under one application of the load. The format of Equation 5-2 is preferred for the analyses to be performed in Sections 6 and 7.

Equations 5-1 and 5-2 have the same form as the familiar fatigue equation

$$ns^m = c \quad (5-3)$$

where  $n$  is the life at stress level  $s$  and  $c^{1/m}$  is equivalently the "failure" stress for  $n = 1$ . The parameter  $m$  reflects the "degree" of fatigue and is the slope of the fatigue curve in log space. The smaller the value of  $m$  (the steeper the slope), the greater the degree of fatigue.

\*The AY-11 data point was not used in the regression analysis.

†It should be noted that the first load of AY-11 was not hydrostatic.

The value of  $m$  is strongly dependent on the material and the state of stress. In general,  $m$  has been found to vary between about three and a few tens. The present investigation shows  $m$  falling toward the critical lower end of this range. This low value of  $m$  apparently reflects the rather complex stress state (physical configuration), since fatigue tests of plain-concrete cylinders in unconfined compression yield  $m$  values of a few tens (see, for example, Ref. 14). Rock cylinders, on the other hand, exhibit  $m$  values ranging from about seven to a few tens when tested in unconfined compression (see, for example, Ref. 15). Typical  $m$  values corresponding to some earlier investigations are tabulated in Appendix F. It is to be noted, however, that typical fatigue investigations are carried out over a range of at least several thousand cycles, and the region of the plots covering a range of a few hundred cycles often shows a steep slope corresponding to a low value of  $m$  (Ref. 15).

## 5.2 STRAIN GROWTH WITH CYCLES

The strains recorded by the several gages at peak load, monitored at approximately 10-cycle intervals in the tests of Spheres 7, 8, and 9, are shown plotted against cycles in Figure 5-3a, b, and c. Gages 5, 6, and 7 (Fig. 2-2), mounted on the inner surface, behaved erratically because of local effects; and some of their records are omitted.

The growth of peak strains with cycles is approximately linear, showing that the accumulation of damage per cycle is constant. The slope of the lines in Figure 5-3a, b, and c indicates a very low rate of damage accumulation, comparable to the rates observed in the work at Stanford Research Institute (Ref. 3). Average strain-growth plots for the strain gages are shown in Figure 5-3d.

The maximum strains observed in the cyclic tests are compared with those of the single-load tests in Table 5-1. For the single-load tests, the strains at failure are shown. For the cyclic-load tests, strains at the end of cycle 1 are shown for all seven gages; whereas the strains both at the end of cycle 1 and near failure are shown only for the steel-bar-mounted gages. The strains at failure in the single-load tests are observed to be greater than those in the cyclic-load tests of Spheres 5 and 6, which in turn are greater than the strains at failure in Spheres 7, 8, and 9. Thus, spheres subjected to higher pressures showed greater strains, which presumably resulted from the increased inelasticity caused by the higher pressures.

In Table 5-2 the ratios of strain at failure to strain at the end of cycle 1 are compared for the spheres tested by cyclic loading. The ratios, derived from recordings made by the steel-bar-mounted gages, show remarkable consistency, as confirmed by the low coefficients of variation. It is also observed that for all gages, the values of the ratios for Spheres 5 and 6 are of the same order as for Spheres 7, 8, and 9. Since the number of cycles to failure was considerably larger for Spheres 7, 8, and 9, this means that the strain growth per cycle was larger for Spheres 5 and 6, which were tested at a higher pressure.

### 5.3 SPATIAL STRAIN DISTRIBUTION

The average strains obtained from testing the first six spheres at two pressure levels are shown in Figure 5-4a and b. The variability of these strains is shown in Table 5-3. The relative values of the average strains at each radial location are shown in Table 5-4.

Each of the ratios in Table 5-4 should theoretically be 1.0, since strains at the same radius are compared; but a distinct trend appears in the circumferential direction even at the lower pressure, at which the behavior is probably elastic. Moreover, the trends differ between the steel-mounted and the concrete-mounted gages. A 50% increase in pressure leads to strains that are 63% to 69% higher, thus indicating some nonlinearity in the pressure versus strain relation; but the relative strain values at each radial location are not changed much.

The coefficients of variation shown in Table 5-3 suggest that the above trend is not the result of random experimental error but originates from a physical cause. Two possible sources were (1) a geometric imperfection in the mold, leading to a systematic out-of-roundness in all the test spheres, and (2) the material inhomogeneity due to the presence of the epoxy joint. The penetrator was judged to be too far from the gages to influence their records. Finite element calculations incorporating appropriate material properties for epoxy, which were made to address the second possibility, were inconclusive and are not reported.

Table 5-1. Mean peak strains.

Sphere No.	Strain Recorded at:	Mean Strain $\times 10^{-6}$ (COV, %)					
		1	2	3	4	5	6
		Gage No.					
2, 3, 4	Failure	12,300 <sup>*</sup> (-)	15,530 <sup>†</sup> (29.4)	12,120 (40.9)	10,148 (26.6)	5,108 (26.4)	4,572 (12.0)
5, 6	Cycle 1	5,583 (30.8)	4,960 (23.0)	3,350 (62.5)	4,183 (6.2)	4,728 (14.0)	4,990 (0)
	Failure	10,365 (39.4)	7,403 (14.4)	11,013 (9.3)	8,208 (53.7)	--	--
7, 8, 9	Cycle 1	2,892 (9.7)	2,503 (4.4)	2,152 (7.7)	1,918 (10.6)	3,130 (4.6)	2,542 (18.1)
	Failure	4,815 (16.3)	4,022 (25.6)	3,430 (26.3)	3,555 (2.5)	--	--

<sup>\*</sup> From Sphere 2; range (20,000 microstrain) exceeded in Spheres 3 and 4.

<sup>†</sup> From Spheres 2 and 3; range exceeded in Sphere 4.

Table 5-2. Ratio of failure strain to first-cycle strain for steel-mounted gages in cyclic load tests.

Sphere No.	Ratio of Peak Strain near Failure to Peak Strain of Cycle 1			
	1	2	3	4
5	1.95	1.42	2.43	1.17
6	1.71	1.60	5.50*	2.83
7	1.80	1.41	1.47	2.06
8	1.35	1.39	1.30	1.63
9	1.88	1.99	2.00	1.92
Mean	1.74	1.56	1.80	1.92
COV, %	13.5	16.2	28.6	31.8
Mean (all gages):	1.75			
COV, %:	23.7			

\*Omitted in computing mean.

Table 5-3. Variability of strains in Spheres 1 to 6.

Gage No.	COV, %	
	4000 psi (27.6 MPa)	6000 psi (41.4 MPa)
1	10.9	11.2
2	12.4	17.2
3	13.0	10.6
4	12.3	14.4
5	8.7	9.0
6	6.2	4.6
7	16.0	14.4

NOTE: For location of gages, see Figure 2-2.

Table 5-4. Circumferential variation of average strains.

Ratio of Strain Gages	4000 psi (27.6 MPa)	6000 psi (41.4 MPa)
Gage 3/Gage 1	0.774	0.769
Gage 4/Gage 2	0.683	0.676
Gage 6/Gage 5	1.110	1.126

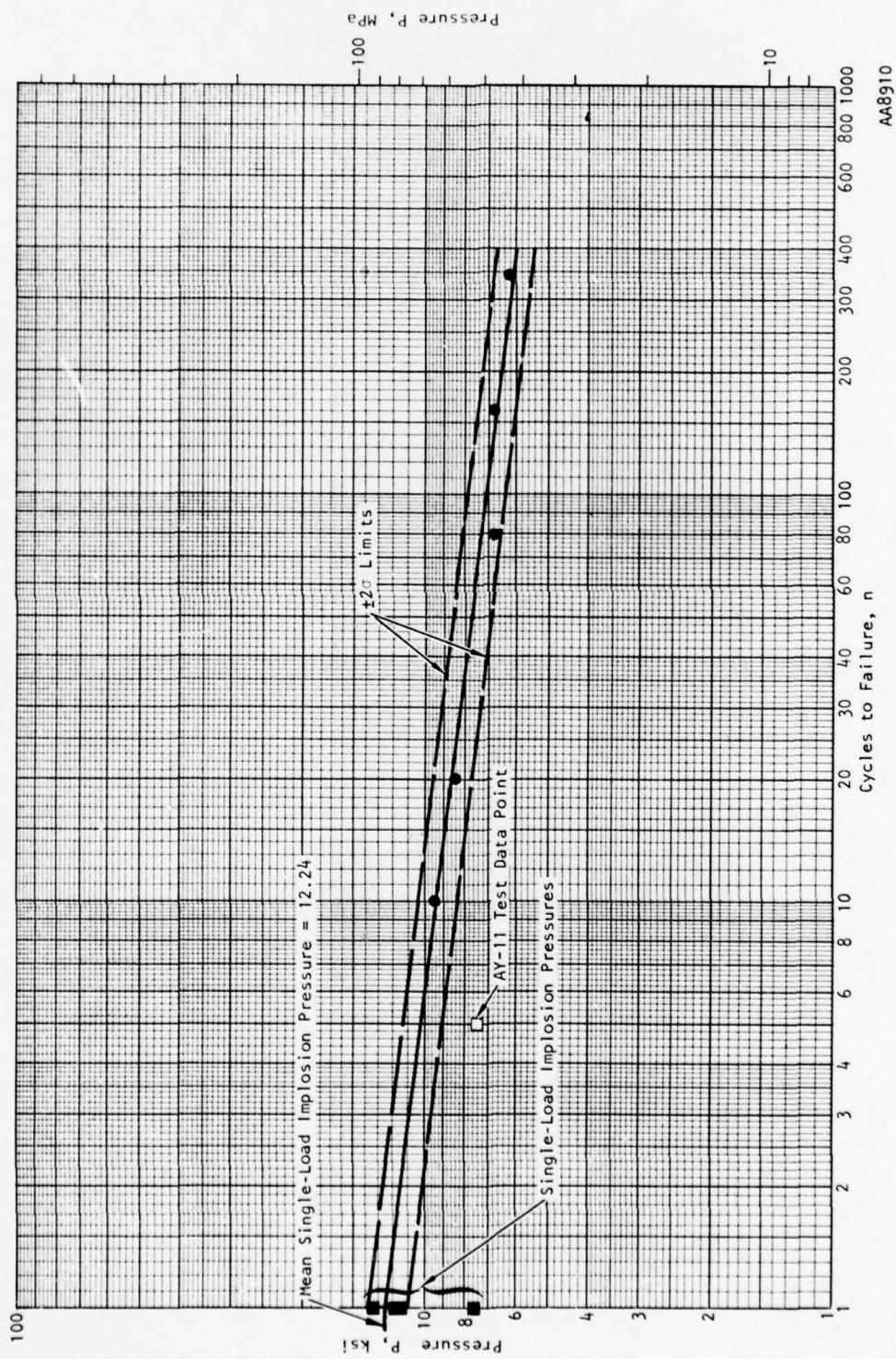


Figure 5-1. Fatigue plot of cyclic test pressure P.

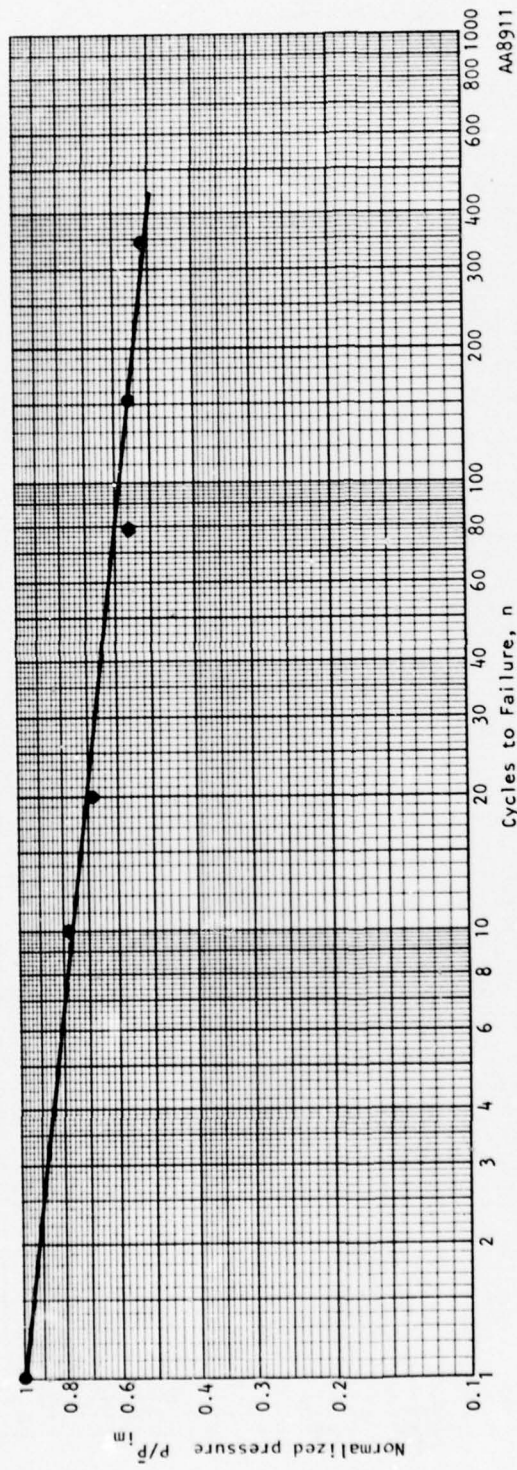
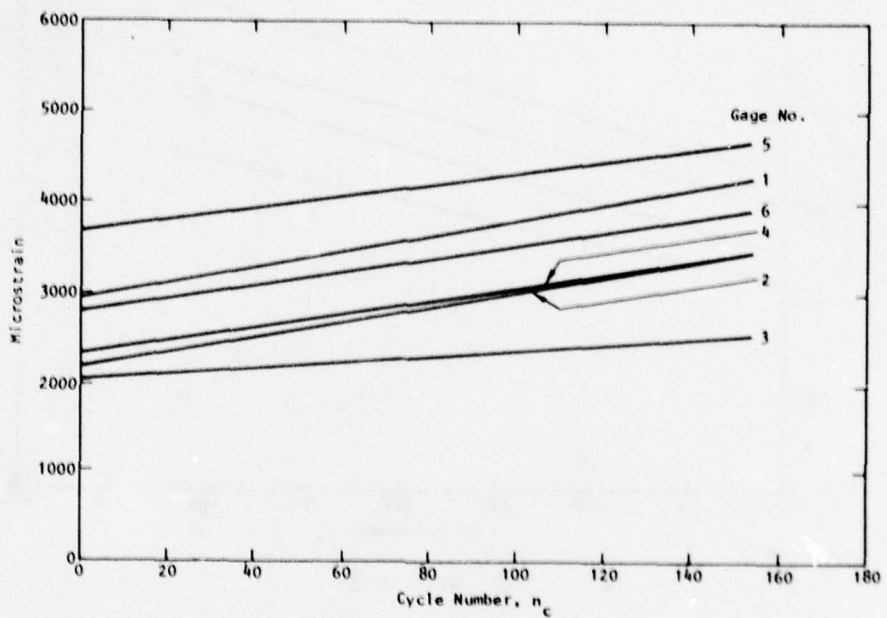
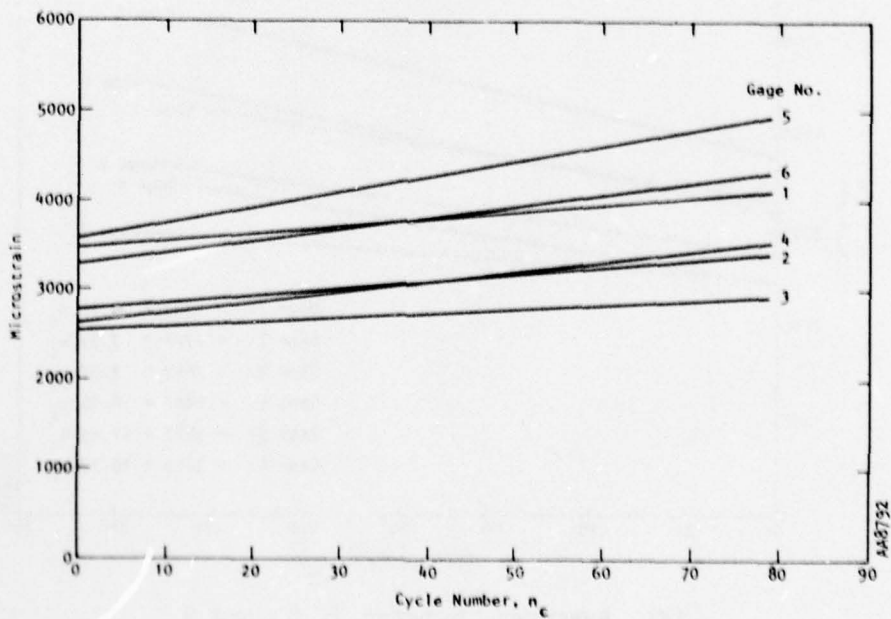


Figure 5-2. Fatigue plot of normalized pressure  $P/\bar{P}_{im}$ .

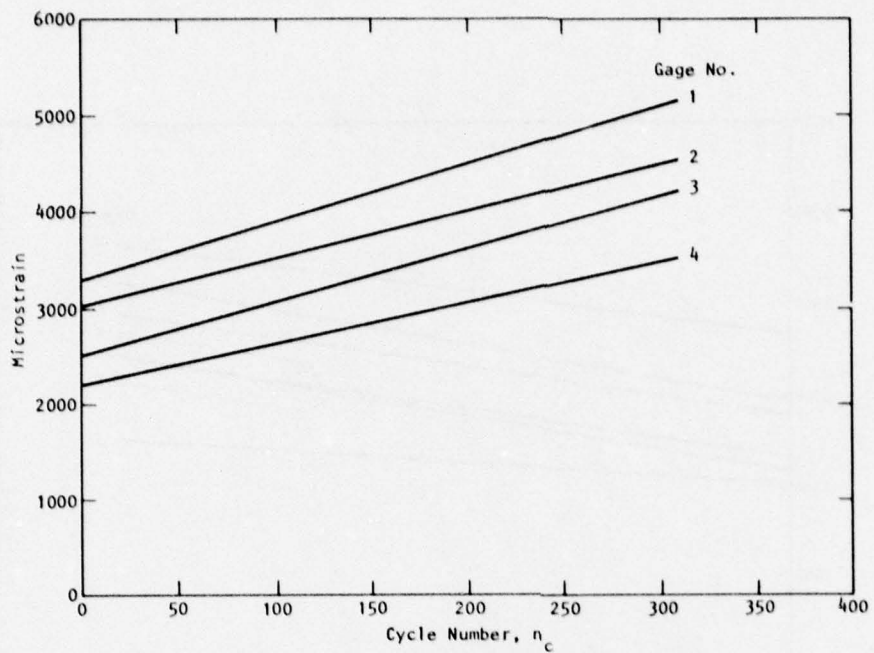


(a) Sphere 7

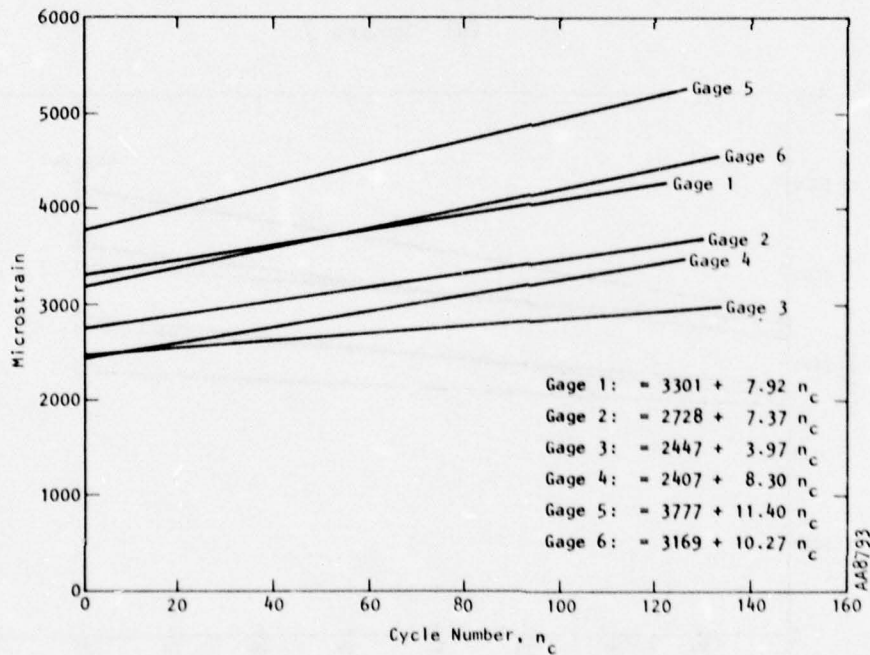


(b) Sphere 8

Figure 5-3. Growth of peak strain with cycles in Spheres 7, 8, and 9.

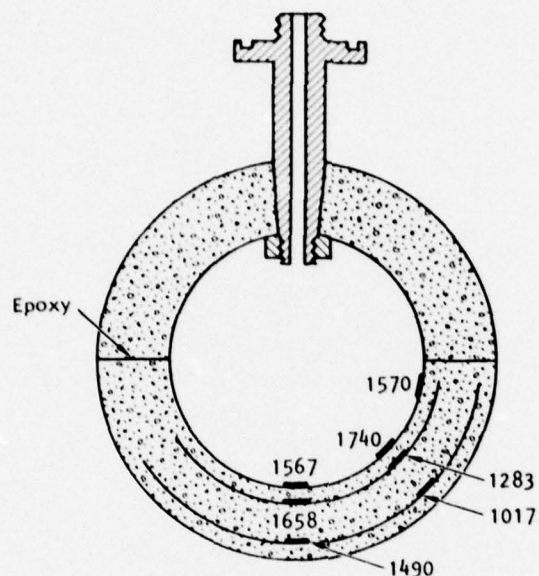


(c) Sphere 9

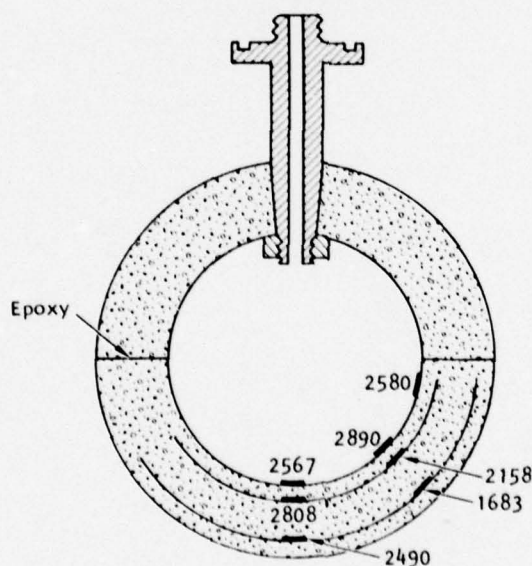


(d) Average: Spheres 7, 8, and 9

Figure 5-3. (Concluded).



(a)  $P = 4000$  psi (27.6 MPa)



(b)  $P = 6000$  psi (41.4 MPa)

Note: Strains in  $\mu\text{in./in.}$ ; Strains Averaged from Spheres 1 through 4 and Cycle 1 of Spheres 5 and 6

AA8791

Figure 5-4. Distribution of hoop strain.

## SECTION 6

### DESIGN/ASSESSMENT METHODOLOGY

#### 6.1 INTRODUCTION

The methodology presented in this section can be used either to design a (failure) mode to meet an allocated survivability goal or to assess the survivability of a mode design. In either case, the load is assumed to arise from sequential multiple bursts and to produce progressive degradation of the mode failure resistance. The methodology is not necessarily restricted to the (failure) modes of rock openings/reinforcement.

The methodology suggested here differs from the methodology that is generally used to treat random fatigue (see, for example, Ref. 16) because of the following characteristics:

- a. One to a hundred load applications are treated, not thousands to millions of load applications.
- b. The methodology must incorporate the rigorous solution to the case of one load application.

#### 6.2 SURVIVABILITY BOUNDS

Consider a (failure) mode whose resistance  $X$  deteriorates in a monotonic fashion under repeated loading. Consider the load sequence  $z_1, z_2, z_3, \dots, z_n, \dots, z_N$ , whose individual loads all have a common distribution function, i.e., have a common mean and COV. Assume that the degree of statistical dependency between the loads is unknown. The probability that the mode survives all  $N$  applications of the load  $z$  is bounded by (Ref. 17):

$$\prod_{n=1}^N P(X_n > z_n) < P(X_1 > z_1 \cap X_2 > z_2 \cap \dots \cap X_n > z_n \cap \dots \cap X_N > z_N) < P(X_N > z_N) \quad (6-1)$$

where  $X_n$  is the mode resistance at the start of the application of  $z_n$ , the symbol  $\prod$  signifies the multiplication of terms, and the symbol  $\cap$  is read "and."

### 6.3 PROBABILITY OF SURVIVAL OF THE N-TH APPLICATION OF THE LOAD, $P(X_n > z_n)$

The probability that the mode survives the  $z_n$  load is (after Ref. 18):

$$P(X_n > z_n) = \Phi \left\{ \frac{\log_e \left[ \frac{\bar{x}_n}{\bar{z}} \exp \left( - k_\alpha \sqrt{\frac{2}{\Delta \bar{x}_n} + \frac{2}{\Delta \bar{z}}} \right) \right]}{\sqrt{\delta_{X_n}^2 + \delta_z^2}} \right\} \quad (6-2)$$

where

$x_n$  = Mode failure resistance at the start of the application of load  $z_n$

$\bar{x}_n$  = Best estimate of  $\mu_{X_n}$ , the mean (average or expected) value of  $x_n$

$z_n$  = Mode load

$\bar{z}$  = Best estimate of  $\mu_{Z_n}$ , the mean (average or expected) value of  $z_n$   
( $n = 1, 2, 3, \dots, N$ )

$k_\alpha$  = Parameter that reflects our confidence that the probability of survival is greater than or equal to  $P(X_n > z_n)$

<u>Confidence</u>	<u><math>k_\alpha</math></u>
50%	0
90%	1.282
95%	1.645
99%	2.326

$\Delta \bar{x}_n$  = COV that reflects our uncertainty in estimating  $\mu_{X_n}$ , the mean of  $x_n$

$\Delta \bar{z}$  = COV that reflects our uncertainty in estimating  $\mu_{Z_n}$ , the mean of  $z_n$  ( $n = 1, 2, 3, \dots, N$ )

$\Phi(\xi)$  = Tabulated cumulative probability of the standard normal variate  $\xi$

$\delta_{X_n}$  = COV that reflects the real random nature of  $X_n$

$\delta_Z$  = COV that reflects the real random nature of  $Z_n$  ( $n = 1, 2, 3, \dots, N$ )

Equation 6-2 is displayed in Figure 6-1.

The following assumptions are inherent in Equation 6-2:

a.  $\delta_{X_n}^2 \ll 1$

b.  $\delta_Z^2 \ll 1$

c.  $\Delta_{X_n}^2 \ll 1$

d.  $\Delta_Z^2 \ll 1$

e.  $X_n, \bar{X}_n, Z_n$ , and  $\bar{Z}$  are lognormally distributed

When  $X_n$  and  $Z_n$  are themselves functions of random variables, the information provided in Table 6-1 can be used to calculate first-order approximations of their means and COVs.\* The  $\delta_{Y_r}$  COVs are determined from experimental data; whereas, the  $\Delta_{Y_r}$  COVs are determined by quantifying our "degrees of belief."

#### 6.4 FATIGUE DATA

Assume that low-cycle fatigue data have been collected for the mode and that it takes the familiar form

$$nZ^m = c \quad (6-3)$$

---

\*The following assumptions are inherent in the information provided in Table 6-1:

a.  $\delta_{Y_r}^2 \ll 1$

b. The nonlinearity in  $Q$  near  $\bar{Q}$  is not severe.

where  $n$  is the life of the mode (expressed in terms of number of load applications) at the applied load level  $Z$ , and  $m$  and  $c$  are experimentally determined parameters. A more useful form of Equation 6-3 is

$$nZ^m = x_1^m \quad (6-4a)$$

or

$$n\left(\frac{Z}{x_1}\right)^m = 1 \quad (6-4b)$$

where  $x_1$  is the mode resistance at the start of the first application of the load  $Z$ . Thus, there is actually only one fatigue parameter:  $m$ . The regression line of Equation 6-4b is plotted in Figure 6-2 for illustrative values of  $m$ .

## 6.5 RESISTANCE $x_n$

Assume that  $x_n$  is given by

$$x_n = x_1 \psi(n) \quad (6-5)$$

where the function  $\psi(n)$  decreases monotonically with increasing  $n$ . The function  $\psi(n)$  is readily evaluated at  $n = 1$  and  $n = n_Z$ . Obviously,

$$\psi(1) = 1.0 \quad (6-6)$$

Equation 6-4 requires that

$$x_{n_Z} = Z = x_1 \left(\frac{1}{n_Z}\right)^{1/m} \quad (6-7)$$

Thus,

$$\psi(n_Z) = \left(\frac{1}{n_Z}\right)^{1/m} = \frac{Z}{x_1} \quad (6-8)$$

The value of  $\psi(n \neq 1, n \neq n_2)$  is unknown. A linear assumption for  $\psi(n)$  is therefore appropriate.\* Thus, we observe that Equations 6-6 and 6-8 lead to

$$\psi(n) = 1 - \frac{n-1}{(x_1/z)^m - 1} \left( 1 - \frac{1}{x_1/z} \right) \quad (6-9)$$

and finally to

$$x_n = x_1 \left[ 1 - \frac{n-1}{(x_1/z)^m - 1} \left( 1 - \frac{1}{x_1/z} \right) \right] \quad (6-10)$$

The mean value of  $x_n$  is<sup>†</sup>

$$\bar{x}_n = \bar{x}_1 \left[ 1 - \frac{n-1}{(\bar{x}_1/\bar{z})^m - 1} \left( 1 - \frac{1}{\bar{x}_1/\bar{z}} \right) \right] \quad (6-11)$$

where the bar signifies our best estimate of the mean value. Equation 6-11 is plotted in Figure 6-3 for illustrative values of  $\bar{m}$  and  $\bar{x}_1/\bar{z}$ .

\*Strain was found to accumulate in a linear fashion for this experimental program (see Sec. 5.2). But whether strain is the appropriate measure of damage is, of course, not known. It is possible to determine  $\psi(n)$  experimentally by performing cyclic loading followed by a destructive test for failure. Many such tests would be required.

<sup>†</sup>Equation 6-11 is a good approximation for  $\bar{m}$  that is not large compared to unity.

According to Table 6-1, the COV is

$$\begin{aligned}
 \delta_{\bar{X}_n}^2 &= \delta_{g_{\bar{X}_n}}^2 + \left( \frac{n-1}{\bar{B}^{\bar{m}} - 1} \right)^2 \left( \frac{(\bar{B} - 1) \bar{B}^{\bar{m}-1} \log_e \bar{B}^{\bar{m}}}{(\bar{B}^{\bar{m}} - 1)} \right)^2 \left( \frac{\bar{X}_1}{\bar{X}_n} \right)^2 \delta_m^2 \\
 &+ \left( \frac{n-1}{\bar{B}^{\bar{m}} - 1} \right)^2 \left( \frac{1 + \bar{m} \bar{B}^{\bar{m}+1} - (\bar{m} + 1) \bar{B}^{\bar{m}}}{\bar{B}(\bar{B}^{\bar{m}} - 1)} \right)^2 \left( \frac{\bar{X}_1}{\bar{X}_n} \right)^2 \delta_z^2 \\
 &+ \left[ 1 - \frac{n-1}{\bar{B}^{\bar{m}} - 1} \left( \frac{\bar{m} \bar{B}^{\bar{m}-1} (\bar{B} - 1) - (\bar{B}^{\bar{m}} - 1)}{\bar{B}^{\bar{m}} - 1} \right) \right]^2 \left( \frac{\bar{X}_1}{\bar{X}_n} \right)^2 \delta_{\bar{X}_1}^2
 \end{aligned} \tag{6-12}$$

where  $\bar{B} = \bar{X}_1/\bar{Z}$ . The COV  $\Delta_{\bar{X}_n}$  is calculated from Equation 6-12 by replacing the  $\delta$ 's with  $\Delta$ 's.

## 6.6 ILLUSTRATIVE EXAMPLES

Two examples are provided below to illustrate the use of the above methodology (Eq. 6-1 to 6-12).

### 6.6.1 Analysis

6.6.1.1 The Problem. Determine the probability of survival (at 90% confidence) for five applications of the load  $Z$ , for  $\bar{X}_1/\bar{Z} = 2$ , and for the following inputs.

#### 6.6.1.2 The Inputs.

Load

$$\delta_z = 0.17$$

$$\Delta_{\bar{Z}} = 0.36$$

*Resistance*

$$\delta_{x_1} = 0.17$$

$$\Delta \bar{x}_1 = 0.36$$

$$\bar{m} = 4$$

$$\delta_m = 0.17$$

$$\Delta \bar{m} = 0.36$$

$$\delta_{g_{x_n}} = 0.00$$

$$\Delta \bar{g}_{x_n} = 0.00$$

*Number of Load Applications*

$$N = 5$$

*Confidence Parameter*

$$k_\alpha = 1.282$$

*Mean Factor of Safety*

$$\bar{x}_1/\bar{z} = 2$$

**6.6.1.3 The Solution.**

Step 1: Calculate  $\bar{x}_n/\bar{x}_1$  (Eq. 6-11).

n	$\bar{x}_n/\bar{x}_1$
1	1.00
2	0.97
3	0.93
4	0.90
5	0.87

Step 2: Calculate  $\delta_{X_n}$  (Eq. 6-12).

n	$\delta_{X_n}$
1	0.17
2	0.19
3	0.22
4	0.25
5	0.28

Step 3: Calculate  $\Delta_{\bar{X}_n}$  (Eq. 6-12).

n	$\Delta_{\bar{X}_n}$
1	0.36
2	0.40
3	0.47
4	0.53
5	0.59

Step 4: Calculate  $\sqrt{\delta_{X_n}^2 + \delta_Z^2}$ .

n	$\sqrt{\delta_{X_n}^2 + \delta_Z^2}$
1	0.24
2	0.25
3	0.28
4	0.30
5	0.33

Step 5: Calculate  $\sqrt{\frac{\Delta_x^2}{X_n} + \frac{\Delta_z^2}{Z}}$ .

n	$\sqrt{\frac{\Delta_x^2}{X_n} + \frac{\Delta_z^2}{Z}}$
1	0.51
2	0.54
3	0.59
4	0.64
5	0.69

Step 6: Calculate the ordinate of Figure 6-1.

n	$\frac{\bar{X}_n}{\bar{Z}} \exp \left( - k_a \sqrt{\frac{\Delta_x^2}{X_n} + \frac{\Delta_z^2}{Z}} \right)$
1	1.04
2	0.97
3	0.87
4	0.79
5	0.72

Step 7: Determine  $P(X_n > Z_n)$  (Fig. 6-1).

n	$P(X_n > Z_n)$
1	0.56
2	0.45
3	0.31
4	0.21
5	0.16

Step 8: Calculate survivability (Eq. 6-1).

$$0.003 < P(X_1 > Z_1 \cap \dots \cap X_5 > Z_5) < 0.16$$

The upper-bound probability 0.16 would apply if the loads were perfectly correlated (i.e.,  $Z_1 = Z_2 = Z_3 = Z_4 = Z_5$ ) and if the resistances were perfectly correlated (i.e., if the degradation function  $\psi(n)$  [see Eq. 6-9] were deterministic).

Finally, it is interesting to note that for no fatigue, i.e., for  $\bar{m} \rightarrow \infty$ ,

$$0.06 < P(X > z_1 \cap \dots \cap X > z_5) < 0.56$$

### 6.6.2 Design

6.6.2.1 The Problem. Determine the mean factor of safety  $\bar{X}_1/\bar{Z}$  required to meet a survivability goal of 0.9 (at 90% confidence) for two applications of load  $Z$ .

#### 6.6.2.2 The Inputs.

##### *Load*

$$\delta_Z = 0.17$$

$$\Delta_{\bar{Z}} = 0.36$$

##### *Resistance*

$$\delta_{X_1} = 0.17$$

$$\Delta_{\bar{X}_1} = 0.36$$

$$\bar{m} = 2$$

$$\delta_m = 0.00$$

$$\Delta_{\bar{m}} = 0.36$$

$$\delta_{g_{X_m}} = 0.00$$

$$\Delta_{\bar{g}_{X_n}} = 0.00$$

##### *Number of Load Applications*

$$N = 2$$

##### *Required Survivability*

$$P(X_1 > z_1 \cap X_2 > z_2) = 0.9$$

##### *Confidence Parameter*

$$k_\alpha = 1.282$$

6.6.2.3 The Solution.

Step 1: Guess  $\bar{x}_1/\bar{z} = 3$ .

Step 2: Calculate  $\bar{x}_n/\bar{x}_1$  (Eq. 6-11).

n	$\bar{x}_n/\bar{x}_1$
1	1.00
2	0.92

Step 3: Calculate  $\delta_{x_n}$  (Eq. 6-12).

n	$\delta_{x_n}$
1	0.17
2	0.20

Step 4: Calculate  $\Delta_{\bar{x}_n}$  (Eq. 6-12).

n	$\Delta_{\bar{x}_n}$
1	0.36
2	0.42

Step 5: Calculate  $\sqrt{\delta_{x_n}^2 + \delta_z^2}$ .

n	$\sqrt{\delta_{x_n}^2 + \delta_z^2}$
1	0.24
2	0.26

Step 6: Calculate  $\sqrt{\frac{\Delta \bar{x}_n^2}{\bar{x}_n} + \frac{\Delta \bar{z}^2}{\bar{z}}}$ .

$n$	$\sqrt{\frac{\Delta \bar{x}_n^2}{\bar{x}_n} + \frac{\Delta \bar{z}^2}{\bar{z}}}$
1	0.51
2	0.55

Step 7: Calculate the ordinate of Figure 6-1.

$n$	$\frac{\bar{x}_n}{\bar{z}} \exp \left( - k_a \sqrt{\frac{\Delta \bar{x}_n^2}{\bar{x}_n} + \frac{\Delta \bar{z}^2}{\bar{z}}} \right)$
1	1.56
2	1.48

Step 8: Determine  $P(X_n > Z_n)$  (Fig. 6-1).

$n$	$P(X_n > Z_n)$
1	0.97
2	0.94

Step 9: Calculate survivability (Eq. 6-1).

$$0.91 < P(X_1 > Z_1 \cap X_2 > Z_2) < 0.97$$

These bounds indicate that the original guess of  $\bar{x}_1/\bar{z} = 3$  is adequate. However, if the lower bound had been less than 0.9, we would have had to guess a higher value of  $\bar{x}_1/\bar{z}$ , repeat Steps 2 through 9, and iterate until the lower-bound probability were greater than or equal to 0.9.

Table 6-1. First-order approximation of means and COVs (Ref. 18).

$$Q = g(Y_1, Y_2, Y_3, \dots, Y_r, \dots, Y_R)$$

Mean

$$\bar{Q} \approx g(\bar{Y}_1, \bar{Y}_2, \bar{Y}_3, \dots, \bar{Y}_r, \dots, \bar{Y}_R)$$

Coefficient of Variation (COV)

$$\delta_Q^2 \approx \delta_g^2 + \sum_{r=1}^R \frac{\bar{Y}_r^2}{\bar{Q}^2} \left( \frac{\partial g}{\partial Y_r} \right)_0^2 \delta_{Y_r}^2$$

$$+ \sum_{r \neq s}^R \sum_{s=1}^R \frac{\bar{Y}_r \bar{Y}_s}{\bar{Q}^2} \left( \frac{\partial g}{\partial Y_r} \frac{\partial g}{\partial Y_s} \right)_0 \rho_{rs} \delta_{Y_r} \delta_{Y_s}^*$$

where

$\delta_g$  = COV associated with the functional form of  $Q$

$\delta_{Y_r}$  = COV associated with  $Y_r$

$\rho_{rs}$  = Correlation coefficient,  $-1 \leq \rho_{rs} \leq 1$

and where the "o" indicates that the partial derivatives are to be evaluated at  $\bar{Y}_r$  ( $r = 1$  to  $R$ ).

---

\*A similar expression holds for  $\Delta_Q^2$ .

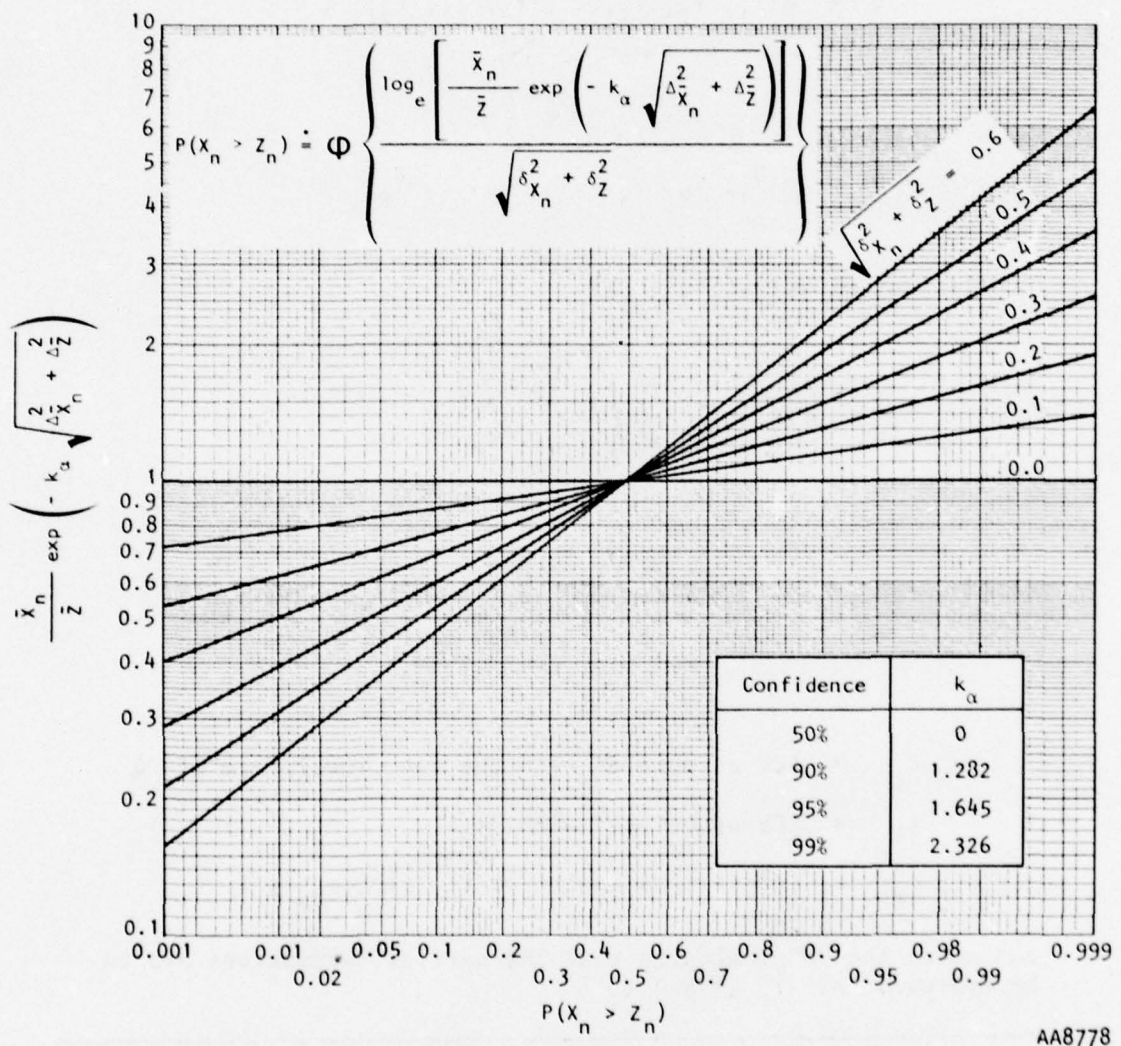


Figure 6-1. Probability that the mode survives the  $z_n$  load.

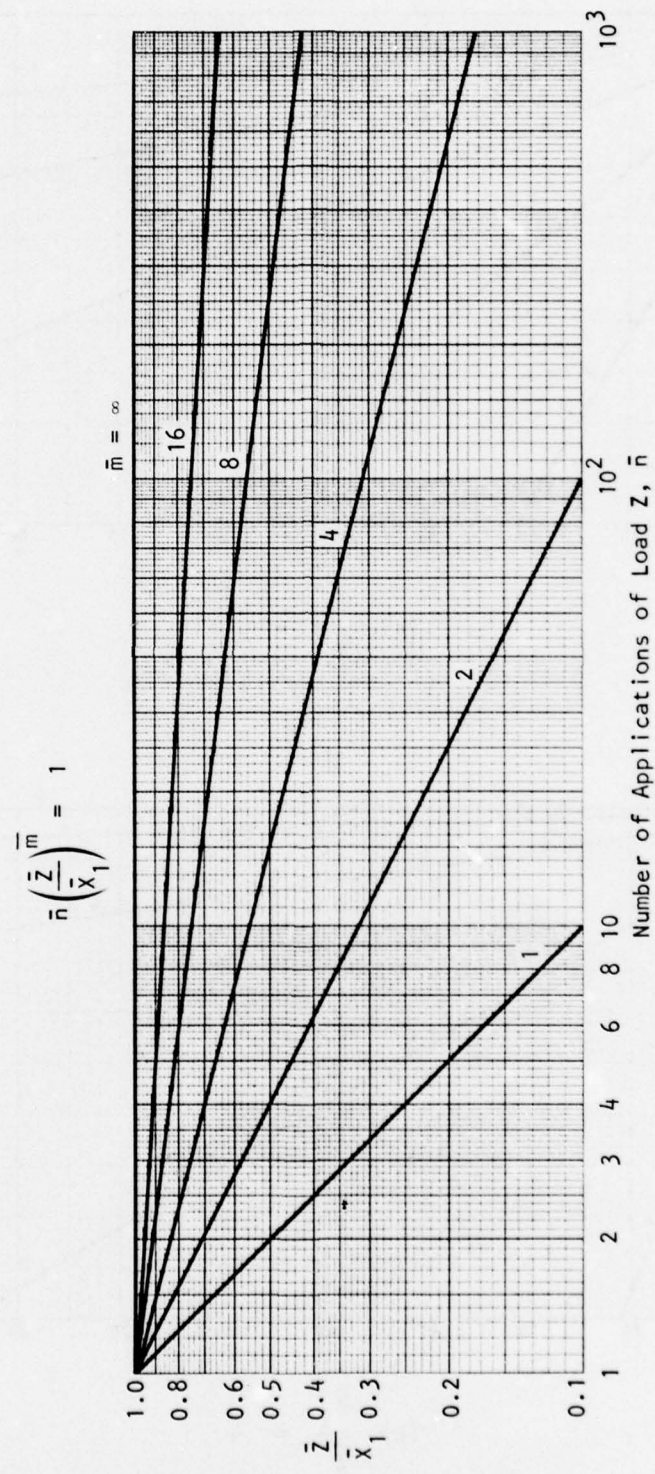
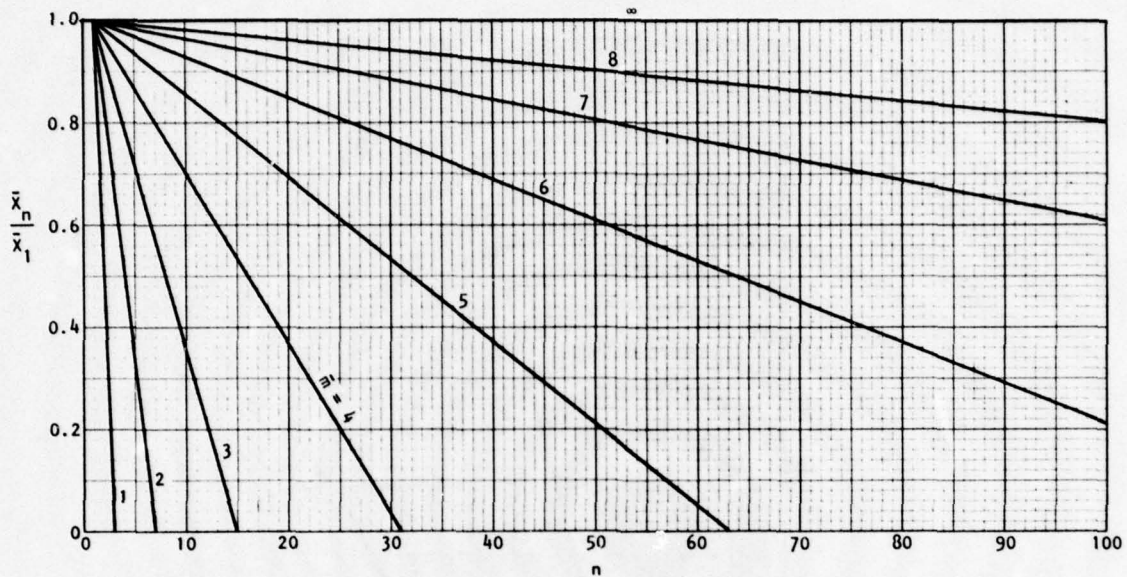
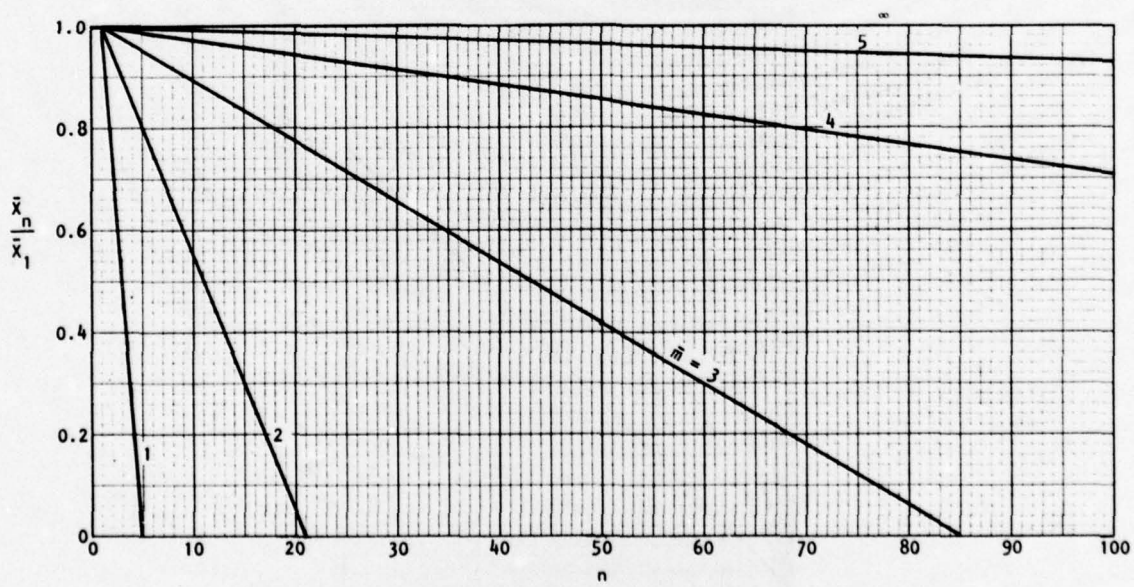


Figure 6-2. Illustrative regression lines of low-cycle fatigue data.



$$(a) \frac{\bar{x}_1}{\bar{z}} = 2$$



$$(b) \frac{\bar{x}_1}{\bar{z}} = 4$$

AA8960

Figure 6-3. Degradation of mean resistance with repeated loading (Eq. 6-11).

## SECTION 7

### SIGNIFICANCE OF LOW-CYCLE FATIGUE FOR ROCK OPENINGS/REINFORCEMENT

The fatigue parameter  $m$  enters the calculation of survivability via the resistance (Eq. 6-10) and the resistance COVs (Eq. 6-12). Examination of these equations reveals that fatigue will be insignificant and can be neglected if

$$\frac{N}{(\bar{x}_1/\bar{z})^m} \ll 1 \quad (7-1)$$

where

$N$  = Total number of applications of the load  $Z$

$\bar{x}_1$  = Best estimate of the mean resistance at the start of the first application of the load  $Z$

$\bar{z}$  = Best estimate of the mean load

$m$  = Fatigue parameter, equal to the exponent of the familiar fatigue data regression line,  $ns^m = c$

The ratio  $\bar{x}_1/\bar{z}$  represents the mean factor of safety for the mode under the first loading. In general,  $\bar{x}_1/\bar{z}$  will fall between 2 and 4 for threats and rock openings/reinforcement of interest. It is speculated that the ineffectiveness of bursts on devastated ground will limit to a few tens the number of bursts  $N$  that would be used against deep underground rock openings/reinforcement.

It is speculated that

$$1 < m < 10$$

for prototype rock openings/reinforcement. Cylindrical specimens of prefailed Westerly granite, which were tested in unconfined compression, exhibit an  $m$  of about 7 (Ref. 15). This suggests that  $m = 7$  is a representative value for

unlined or backpacked cavities in Westerly granite subjected to static load. The test spheres of the present investigation exhibit an  $\bar{m}$  of about 8. However, these values of  $\bar{m}$  are expected to decrease when the added prototype complications of physical penetrations and dynamic nonhydrostatic load are introduced. For other prototype designs that mobilize more plastic strain than the test spheres in attaining  $\bar{x}_1$  (about 1% for the test spheres),  $\bar{m}$  is expected to decrease even further.

Since Inequality 7-1 will not be satisfied if  $\bar{m}$  falls in the lower half of its speculated range, it is concluded that low-cycle fatigue must tentatively be considered in the design and analysis of deep-underground rock openings/reinforcement subjected to sequential, multiple bursts.

## SECTION 8

### CONCLUSIONS

This investigation of the low-cycle fatigue of hollow concrete spheres, with applications to deep-underground rock openings/reinforcement subjected to ground shock arising from nuclear-weapon attack, has successfully met its stated objectives.

The following specific conclusions are drawn from the investigation:

- a. The fatigue data generated follow the general trend of low-cycle fatigue data observed for a wide variety of materials and loading conditions in previous studies. In particular, the familiar power-law equation  $ns^m = c$  can be fitted to express the relationship between the peak applied pressure ( $s$ ) and the number of load cycles to implosion ( $n$ ).
- b. The generated fatigue data exhibit relatively low scatter, attesting to the success and utility of the experimental procedures used.
- c. The test-sphere degradation attributable to low-cycle fatigue was significant. The 100-cycle mean (expected or average) implosion pressure ( $s$ ) was about 0.6 times the single-load implosion pressure.
- d. Strain in a test sphere accumulated in a linear fashion as the specimen was subjected to cyclic loading. Linear accumulation of strain implies that the strain increments per cycle of loading are independent of the total state of strain. However, the strain increments are greater at higher applied pressures.
- e. Low-cycle fatigue data exhibiting the classical  $ns^m = c$  fit can be readily incorporated into first-order probabilistic design procedures that account for variability in both the applied load and the failure resistance of the component.

f. Examination of the suggested design methodology indicates that low-cycle fatigue will be insignificant provided

$$\frac{N}{(\bar{X}_1/\bar{Z})^{\bar{m}}} \ll 1$$

where  $N$  is the number of load applications,  $\bar{X}_1/\bar{Z}$  is the mean factor of safety under the first application of load, and  $\bar{m}$  is the exponent of the familiar fatigue data regression line  $ns^{\bar{m}} = c$ . It is argued that  $N$  could be as large as a few tens, that  $\bar{X}_1/\bar{Z}$  could range from 2 to 4, and that  $1 < \bar{m} < 10$  for deep-underground prototype rock openings/reinforcement subjected to sequential multiple bursts. Since the above inequality will not be satisfied if  $\bar{m}$  falls in the lower half of its speculated range, it is concluded that consideration should be given to low-cycle fatigue in the design and analysis of survivable rock openings/reinforcement.

g. The test spheres subjected to a single load exhibited a ratio of implosion pressure to unconfined compressive strength of 1.35. This ratio was previously found to be 0.85 for similar test specimens fabricated from plain concrete. The enhanced ratio is attributed to the random steel-wire reinforcement and to a higher rate of loading. The loading rate, however, is believed to account for only a small portion of the enhancement.

h. The test spheres subjected to a single load exhibited a ratio of implosion pressure to in-plane cracking pressure of 1.49. This ratio was previously found to be 1.25 for similar test specimens fabricated from plain concrete. This difference indicates a greater load capacity beyond initiation of inelastic response (in-plane cracking) for the specimens with random steel-wire reinforcement.

## SECTION 9

### REFERENCES

1. Agbabian-Jacobsen Assoc. (AJA). *Design Considerations for Deep Underground Protective Facilities*, R-7020-1760. Los Angeles, CA: AJA, Mar 1972. (AD 744 790)
2. Agbabian-Jacobsen Assoc. (AJA). *Material Failure of Penetrations to Deep Underground Protective Cavities--Effect of Deterioration of Rock Properties*, R-7126-2178. Los Angeles, CA: AJA, Jan 1972.
3. Stanford Res. Inst. (SRI). *Laboratory Investigation of Rock Cavity Reinforcement*, DNA-4023F. Menlo Park, CA: SRI, Apr 1976. (AD A043 398)
4. Agbabian Assoc. (AA) *Mighty Epic Spherical Structures Experiment*, El Segundo, CA: AA, Unpublished.
5. Haynes, H.H.; Kahn, L.G.; and Stachiw, J.D. "Concrete Hulls for Undersea Applications," in *Civil Engineering in the Oceans 11*. New York: Amer. Soc. of Civil Eng., Dec 1969.
6. Haynes, H.H. *Handbook for Design of Undersea, Pressure-Resistant Concrete Structures*, Port Hueneme, CA: Naval Civil Eng. Lab., Sep 1976.
7. Stachiw, J.D. and Gray, K.O. *Behavior of Spherical Concrete Hulls under Hydrostatic Loading; Pt. 1 - Exploratory Investigation*, TR-R-517. Port Hueneme, CA: Naval Civil Eng. Lab., Mar 1967. (AD 649 290)
8. Stachiw, J.D. *Behavior of Spherical Concrete Hulls under Hydrostatic Loading; Pt. 2 - Hull Penetrations*, TR-R-547. Port Hueneme, CA: Naval Civil Eng. Lab., Oct 1967.
9. Stachiw, J.D. and Mack, K. *Behavior of Spherical Concrete Hulls under Hydrostatic Loading; Pt. 3 - Relationship between Thickness to Diameter Ratio and Critical Pressures, Strains, and Water Permeation Rates*, TR-R-588. Port Hueneme, CA: Naval Civil Eng. Lab., Jun 1968.
10. Haynes, H.H. et al. *Polymer-Impregnated Concrete Spherical Hulls under Hydrostatic Loading*, TR-R-753. Port Hueneme, CA: Naval Civil Eng. Lab., Dec 1971. (AD 736 598)
11. Haynes, H.H. and Kahn, L.J. *Behavior of 66-Inch Concrete Spheres under Short- and Long-Term Hydrostatic Loading*, TR-R-774. Port Hueneme, CA: Naval Civil Eng. Lab., Sep 1972. (AD 748 584)
12. Haynes, H.H.; Page, G.L.; and Ross, R.J. *Hydrostatic Loading of Concrete Spherical Hulls; Reinforced with Steel Liners*, TR-R-785. Port Hueneme, CA: Naval Civil Eng. Lab., Apr 1973.
13. Timoshenko, S. and Goodier, J.N. *Theory of Elasticity*. New York: McGraw Hill, 1951.

#### REFERENCES (CONCLUDED)

14. Awad, M.E. and Hilsdorf, H.K. "Strength and Deformation Characteristics of Plain Concrete Subjected to High Repeated and Sustained Loads," in *Fatigue of Concrete*. Detroit; Amer. Concrete Inst., 1974.
15. Haimson, B.C. "Mechanical Behavior of Rock Under Cyclic Loading," in *Advances in Rock Mechanics*, Proc. 3rd Congress of the International Soc. for Rock Mechanics, Vol. 2, Pt. A, pp 373-378. Washington, DC: Nat'l Academy of Sciences, 1974.
16. Ang, A.H-S. "Risk, Reliability, and Safety Analyses in Engineering Design," in *Structural and Geotechnical Mechanics* edited by W.J. Hall. Englewood Cliffs, NJ: Prentice-Hall, 1977.
17. Cornell, C.A. "Bounds on the Reliability of Structural Systems," *Proc. ASCE Struct. Div.* 93:ST1, Feb 1967, pp 786-795.
18. Ang, A.H-S. and Cornell, C.A. "Reliability Bases of Structural Safety and Design," *Proc. ASCE Struct. Div.* 100:ST9, Sep 1974, pp 1755-1769.

## APPENDIX A

### SPECIMEN PREPARATION

This appendix discusses detailed procedures used for preparing the test spheres, including concrete mix design, casting of hemispheres, and fabrication and waterproofing.

#### A.1 MIX DESIGN

Like the MIGHTY EPIC spheres, the specimens were made of concrete reinforced with steel fibers to 1.5% by volume. The mix design for the concrete is shown in Table A-1. The resulting mix was fairly stiff, as shown in Figure A-1.

#### A.2 CASTING

Hemisphere sections were cast in the aluminum molds shown in Figures 2-3 and 2-4. Figure A-2 shows further details of the molds. The same mold was used for each hemisphere; however, the top hemispheres differed from the bottom hemispheres. The top hemisphere had a hole cast at the apex for a steel penetrator. The bottom hemisphere had two steel strips, or model rebar, to which strain gages were attached. Figures A-3 and A-4 show the installation of rebars on the molds.

The mold, prior to casting, was lubricated with Dow Corning silicone grease, which acted as a form-release agent. The mold was vibrated with an external pneumatic vibrator.

Approximately 20 hours after casting, the concrete hemispheres (Fig. A-5) were removed from the molds. The specimens were cured in an environment of 100% relative humidity for the first 14 days and an environment of 50% relative humidity for the following 28 days. Subsequent to this 42-day period, the specimens were cured in a laboratory room environment.

#### A.3 ASSEMBLY

The equatorial edges of the hemispheres were ground flat by using a vibrating table on which silica carbide grit (No. 60) and water were used as the cutting agent. At this stage, a steel penetrator was bonded in the hole of the top

hemisphere. The two hemispheres were then bonded together at the equator with an epoxy adhesive (Fig. A-6).

The exterior of the sphere was lightly sandblasted in preparation for waterproof coating. The coating material was a two-part phenolic compound (Phenoline 300). After a two-day drying period, the specimen was ready for hydrostatic testing.

Table A-1. Concrete mix design.

Portland Cement, Type III

Santa Clara River aggregate

Water-to-cement ratio = 0.43

Sand-to-cement ratio = 2.55

Coarse aggregate (3/8-in. pea gravel)-to-cement ratio = 0.64

Water-reducing admixture (Zecon) = 8 oz/sack

Steel-fiber reinforcement <sup>\*</sup> = 1.5% by volume or 5% by weight

Sand Gradation	
Sieve Size No.	Percent Passing
4	99
8	85
16	70
30	42
50	17
100	4
200	1

<sup>\*</sup>Fibers were 1.5 in. (38.1 mm) long by 17 mil (0.043 mm) dia.  
(supplied by National Standard Company).

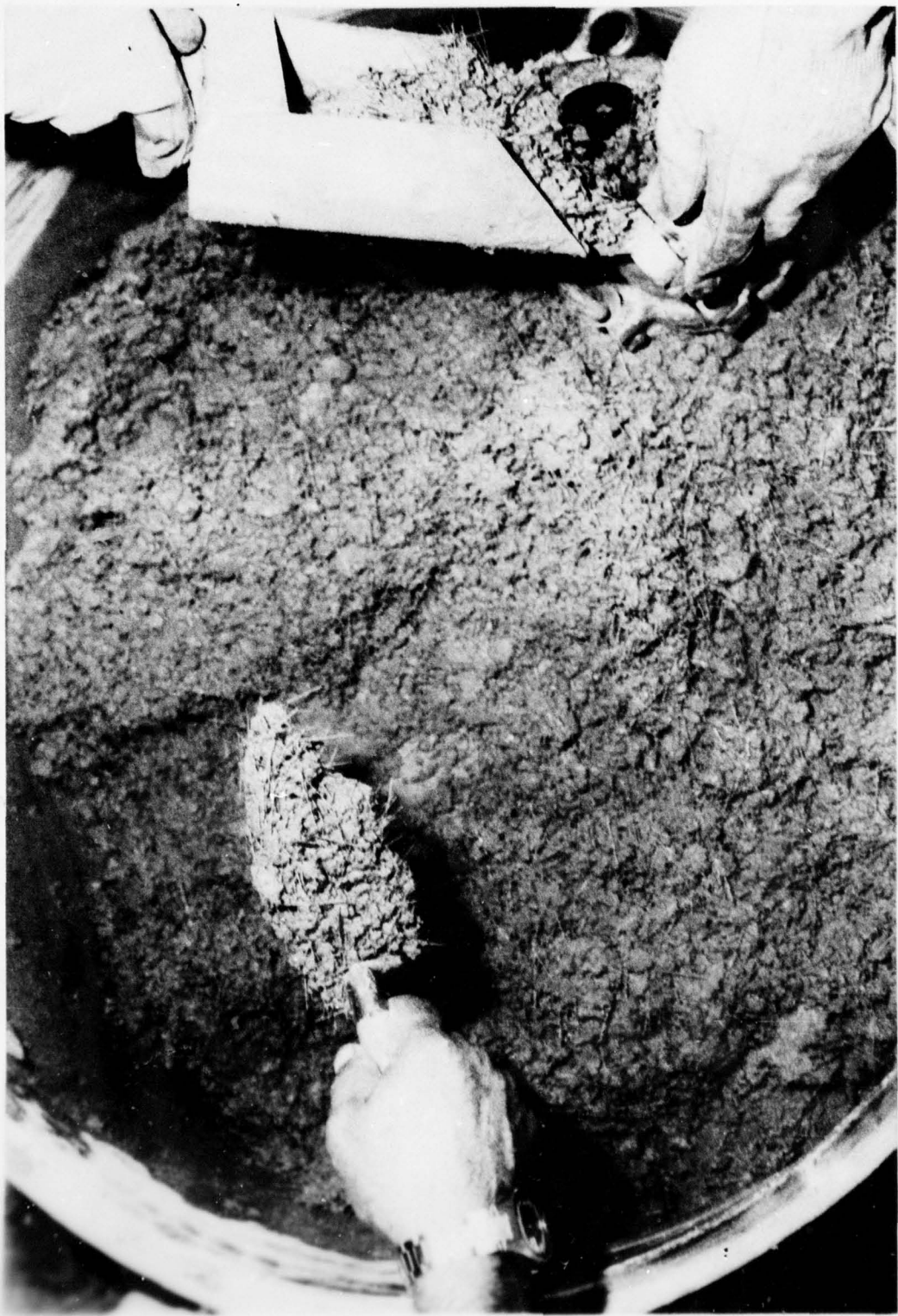
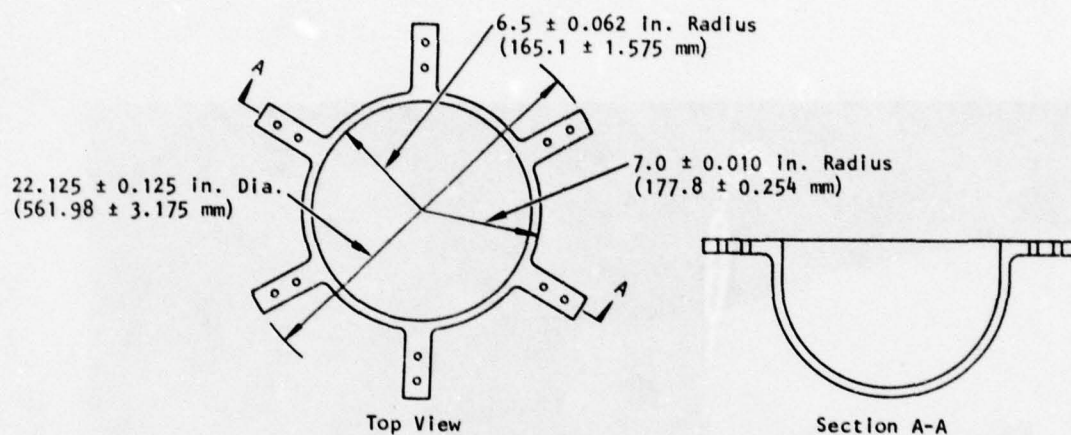
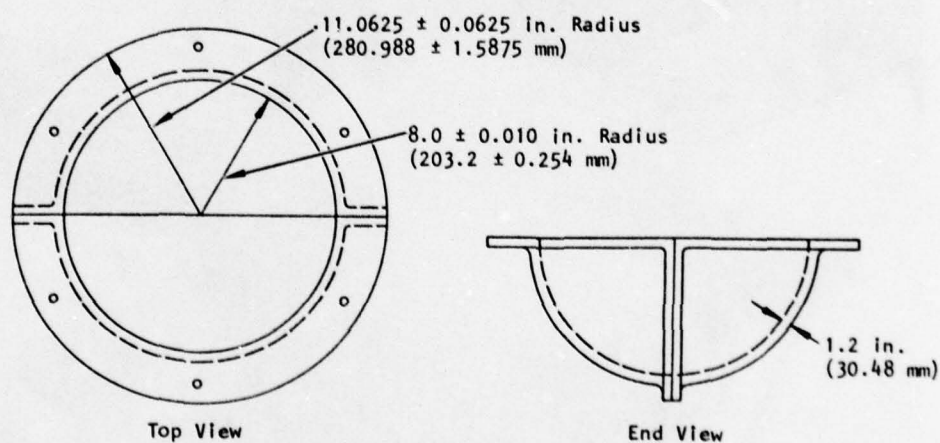


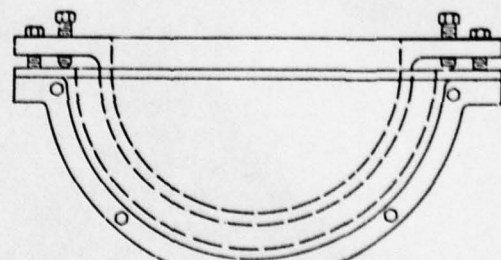
Figure A-1. Consistency of steel-fiber-reinforced concrete.



(a) Male insert



(b) Female shell



(c) Assembly

Figure A-2. Details of mold for concrete hemisphere.

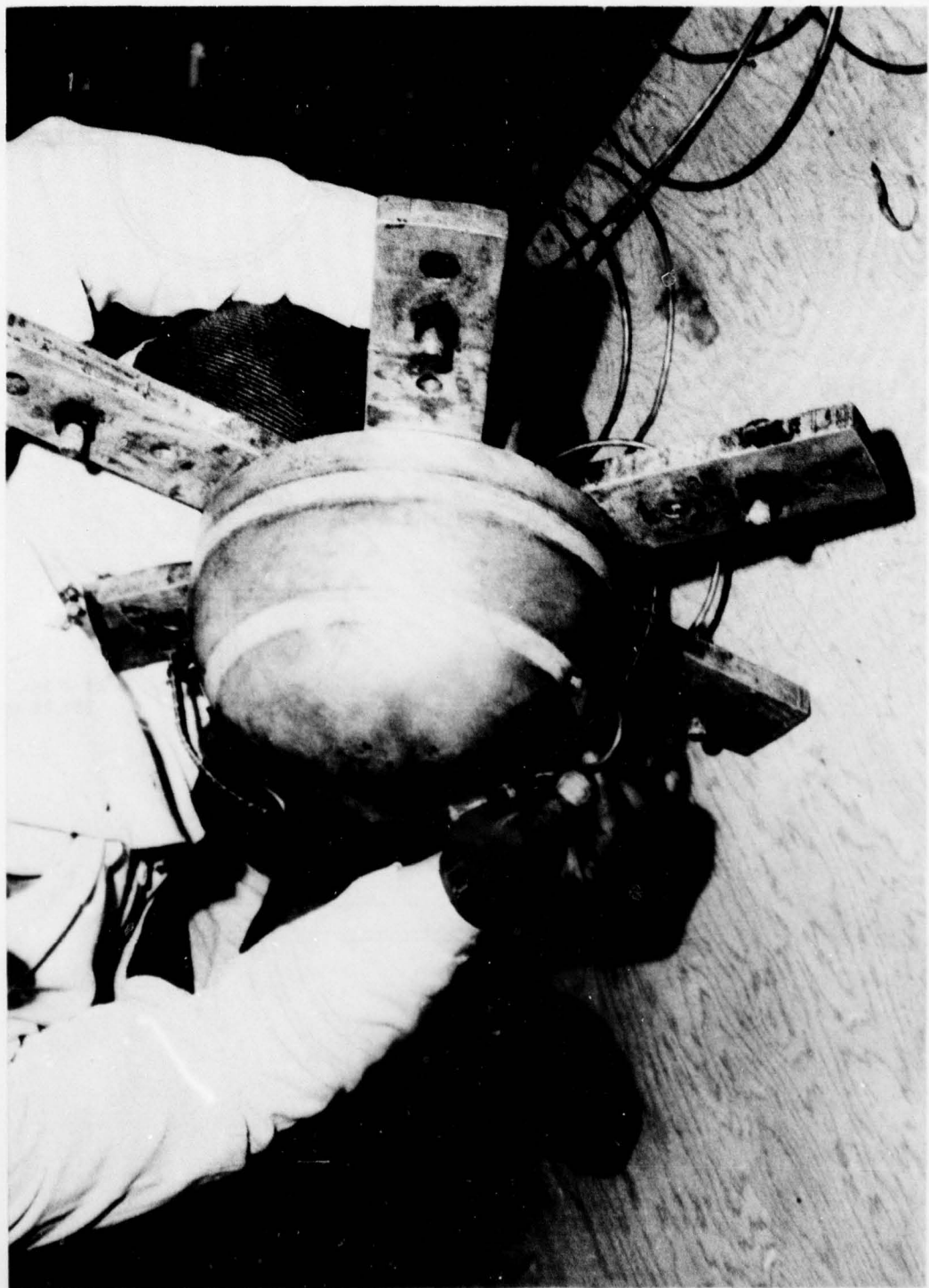


Figure A-3. Arrangement of steel rebar attached to inner mold.



Figure A-4. Arrangement of steel rebar attached to outer mold.



Figure A-5. Cast hemisphere ready for removal of molds.

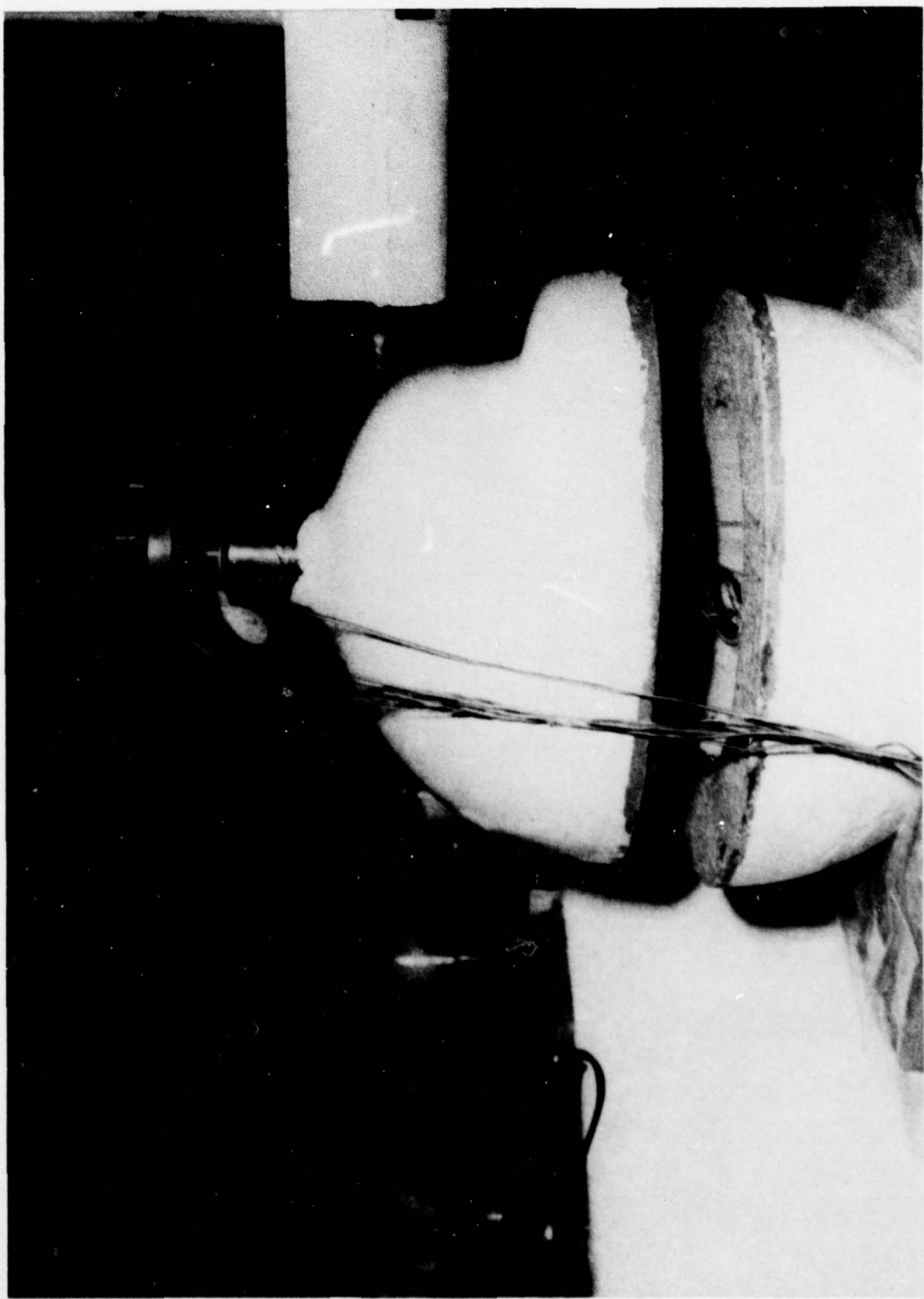


Figure A-6. Hemisphere prepared for bonding with epoxy adhesive.

APPENDIX B  
CYLINDER TEST DATA

Stress/strain curves from the instrumented cylinder tests are shown in Figures B-1 and B-2. Figure B-1 shows the data from single-load tests--small-cylinder data in Figures B-1a and B-1b, and large-cylinder data in Figures B-1c and B-1d. Figure B-2 shows the data from the double-load tests. Table B-1 gives the data from unconfined compression tests on cylinders cast with each hemisphere and tested on the day of the pressure-vessel test of the spherical test specimen associated with them. These data yield a mean unconfined compressive strength of  $\bar{f}'_c = 10,125$  psi (69.8 MPa) with COV 8%.

PRECEDING PAGE BLANK

Table B-1. Cylinder test data.

Associated Sphere, No.*	Unconfined Compressive Strength			Age at Test (days)	Elastic Modulus		Poisson's Ratio
	$f'_c$ psi (MPa)	Mean psi (MPa)	COV (%)		$10^6$ psi (GPa)		
1A	10,040 (69.2)			77	2.6 (17.9)	0.16	
	9,590 (66.1)				3.0 (20.7)	0.17	
	9,270 (63.9)	9,630 (66.4)	4.0		2.9 (20.0)	0.19	
1B	11,160 (76.9)			82	3.2 (22.1)	0.22	
	11,540 (79.6)				3.3 (22.8)	0.14	
	10,010 (69.0)	10,900 (75.2)	7.3		2.9 (20.0)	0.20	
2A	8,630 (59.5)			71	-- --	--	
	7,780 (53.6)				-- --	--	
	8,200 (56.5)	8,200 (56.5)	5.2		-- --	--	
2B	10,400 (71.7)			77	-- --	--	
	9,620 (66.3)				-- --	--	
	9,760 (67.3)	9,320 (64.3)	4.2		-- --	--	
3A	10,440 (72.0)			70	-- --	--	
	9,080 (62.6)				-- --	--	
	9,940 (68.5)	9,820 (67.7)	7.0		-- --	--	
3B	9,040 (62.3)			78	-- --	--	
	9,320 (64.3)				-- --	--	
	9,730 (67.1)	9,360 (64.5)	3.7		-- --	--	
4A	11,390 (78.5)			71	-- --	--	
	11,180 (77.1)				-- --	--	
	10,960 (75.6)	11,180 (77.1)	2.0		-- --	--	
4B	9,900 (68.3)			78	-- --	--	
	9,970 (68.7)				-- --	--	
	9,760 (67.3)	9,880 (68.1)	1.1		-- --	--	
5A	11,030 (76.1)			77	-- --	--	
	11,250 (77.6)				-- --	--	
	10,960 (75.6)	11,080 (76.4)	1.0		-- --	--	
5B	9,900 (68.3)			84	-- --	--	
	10,680 (76.6)				-- --	--	
	9,480 (65.4)	10,020 (69.1)	6.1		-- --	--	

\*Letter "A" designates top hemisphere and "B" bottom hemisphere.

Table B-1. (Concluded).

Associated Sphere, No.	Unconfined Compressive Strength			Age at Test (days)	Elastic Modulus		Poisson's Ratio
	$f'_c$ psi (MPa)	Mean psi (MPa)	COV (%)		$10^6$ psi (GPa)		
6A	11,320 (78.1) 10,610 (73.2) 9,900 (68.3)	10,610 (73.2)	6.7	77	--	--	--
6B	9,900 (68.3) 9,760 (67.3) 9,830 (67.8)	9,830 (67.8)	0.7	84	--	--	--
7A	10,470 (72.2) 9,560 (65.9) 10,850 (74.8)	10,290 (71.0)	6.4	78	--	--	--
7B	10,630 (73.3) 10,930 (75.4) 10,620 (73.2)	10,730 (74.0)	1.7	79	--	--	--
8A	9,900 (68.3) 10,260 (70.8) 10,500 (72.4)	10,220 (70.5)	2.9	84	--	--	--
8B	9,900 (68.3) 11,050 (76.2) 11,180 (77.1)	10,380 (71.6)	5.8	82	--	--	--
9A	10,180 (70.2) 10,620 (73.2) 10,340 (71.3)	10,380 (71.6)	2.1	85	--	--	--
9B	9,340 (64.4) 9,900 (68.3) 9,190 (63.4)	9,480 (65.4)	3.9	83	--	--	--

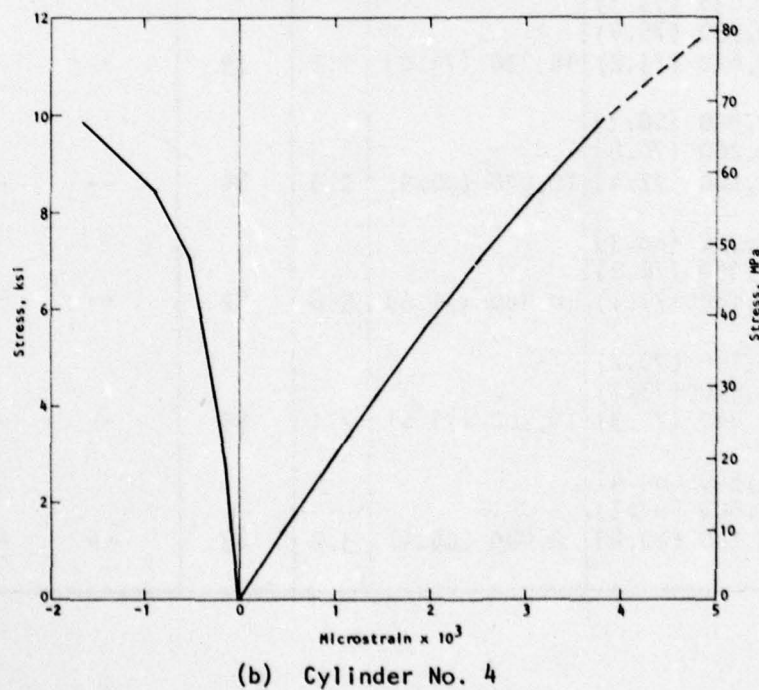
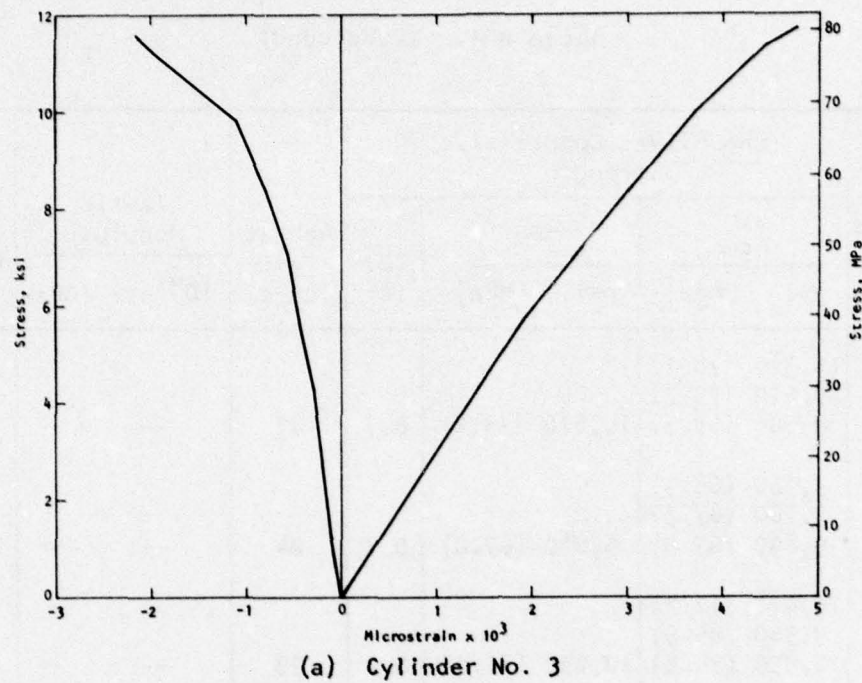
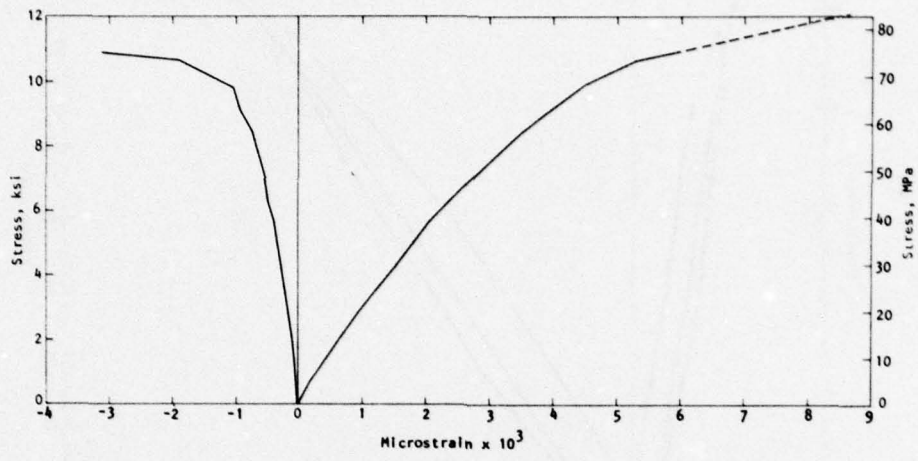
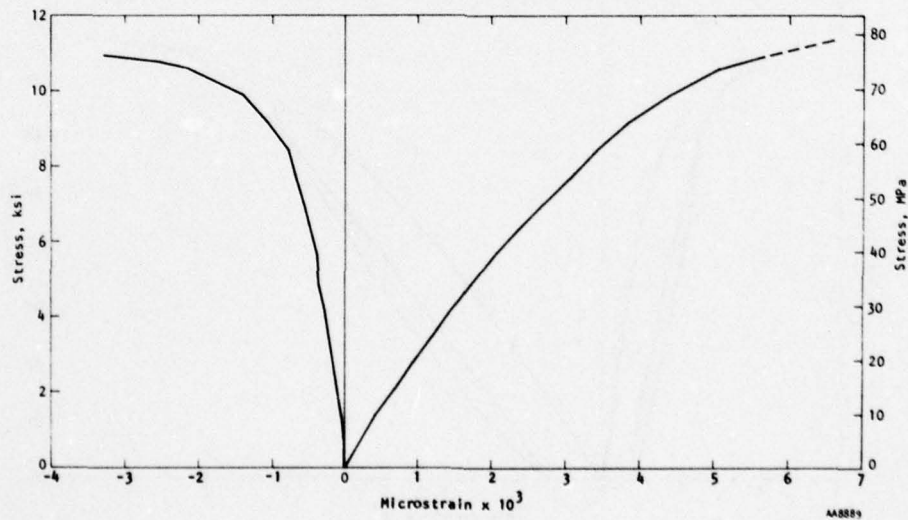


Figure B-1. Stress/strain curves from unconfined compression tests on cylinders--single-load tests.



(c) Cylinder No. 9



(d) Cylinder No. 10

Figure B-1. (Concluded).

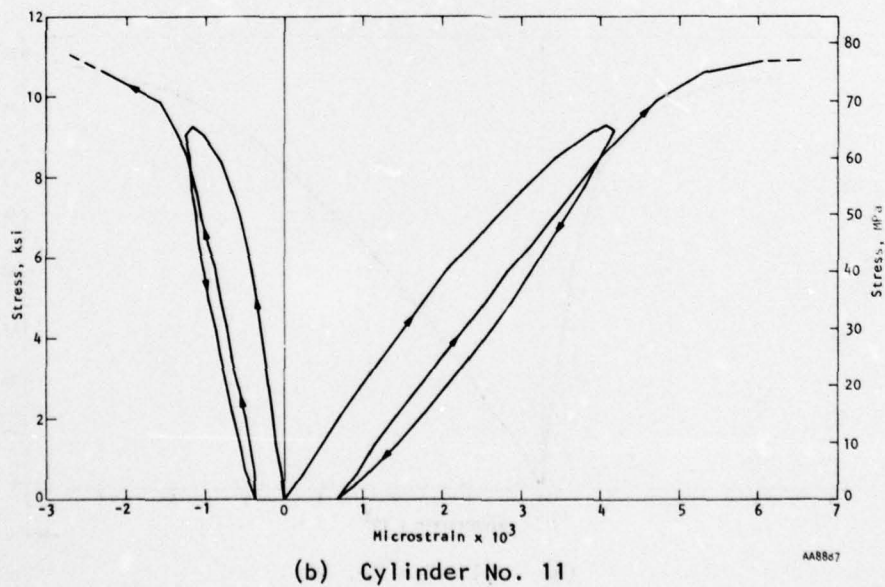
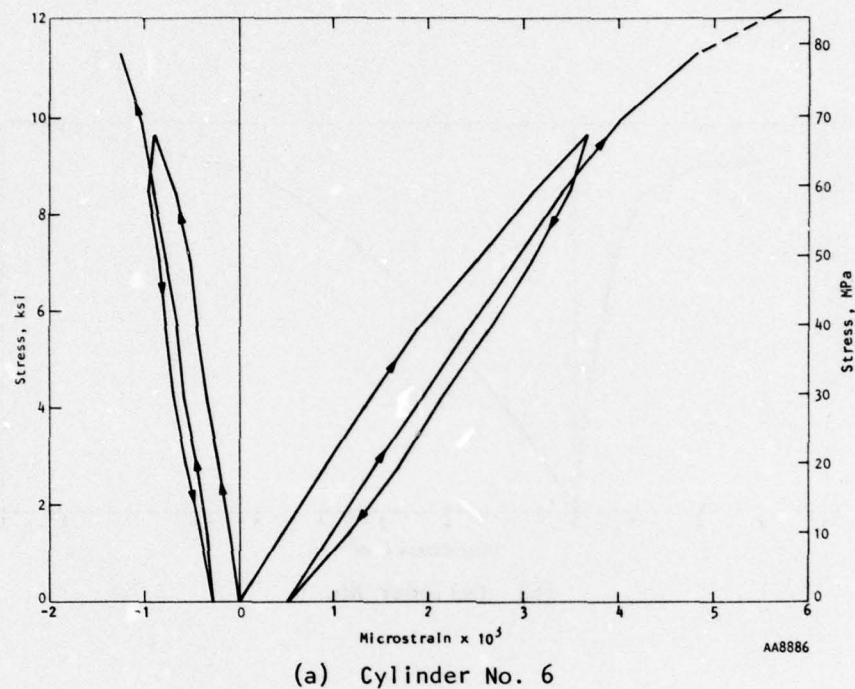
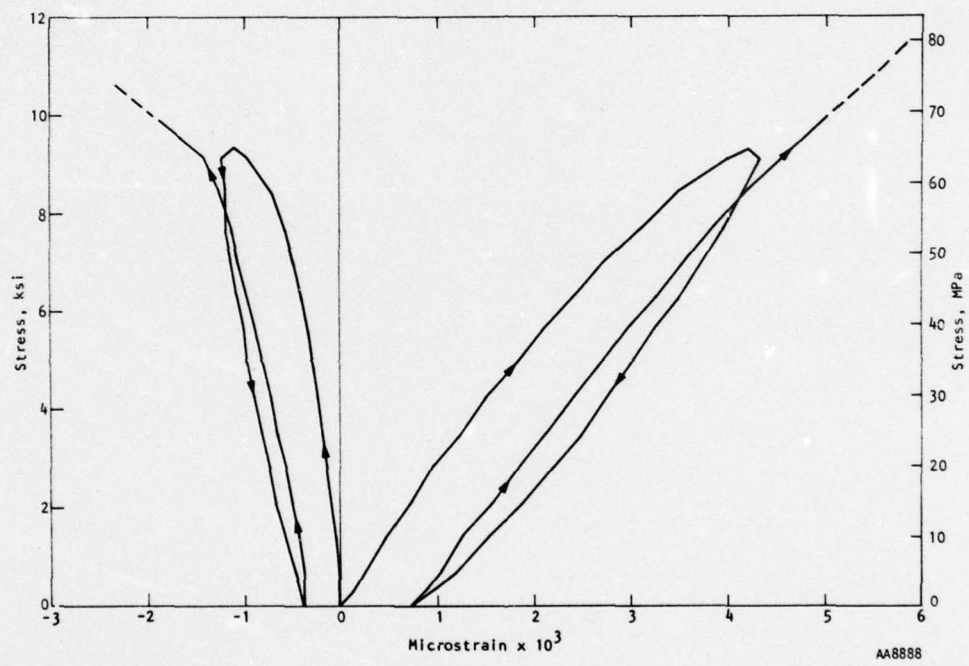


Figure B-2. Stress/strain curves from unconfined compression tests on cylinders--double-load tests.



(c) Cylinder No. 12

Figure B-2. (Concluded).

APPENDIX C  
STRAIN DATA FROM SINGLE-LOAD IMPLOSION TESTS

The pressure versus strain data obtained from the tests of Spheres 1, 3, and 4 are shown in Figures C-1 through C-3. For each specimen, the records of all seven gages are presented, followed by a plot of pressure vs. time showing the loading rate. In-plane cracking, which is signaled by a decrease in strain accompanying an increase in pressure, is clearly shown by the three concrete-mounted gages in the test records of Spheres 3 and 4. Sphere 1 shows in-plane cracking in steel-mounted gages Nos. 2 and 4, mounted near the external surface. This behavior is unusual.

AD-A058 365 AGBABIAN ASSOCIATES EL SEGUNDO CALIF  
LOW-CYCLE FATIGUE TESTS OF HOLLOW CONCRETE SPHERES WITH IMPLICA--ETC(U)  
APR 78 M B BALACHANDRA, C F BAGGE, H H HAYNES DNA001-77-C-0245

UNCLASSIFIED

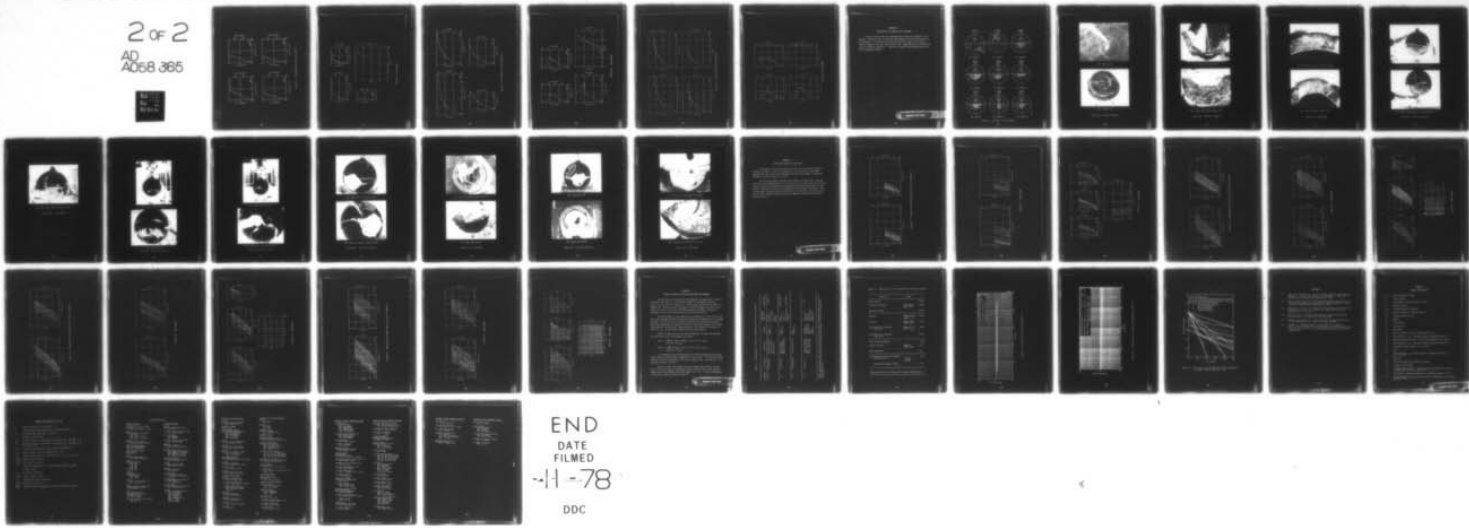
AA-R-7740-4551

DNA-4433F

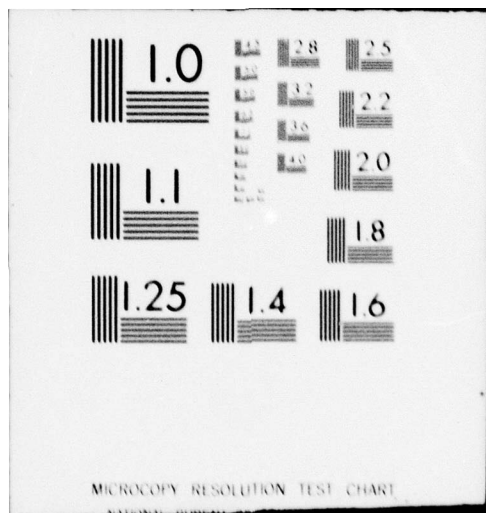
F/6 11/2

NL

2 of 2  
AD  
A058 365



END  
DATE  
FILED  
-11-78  
DDC



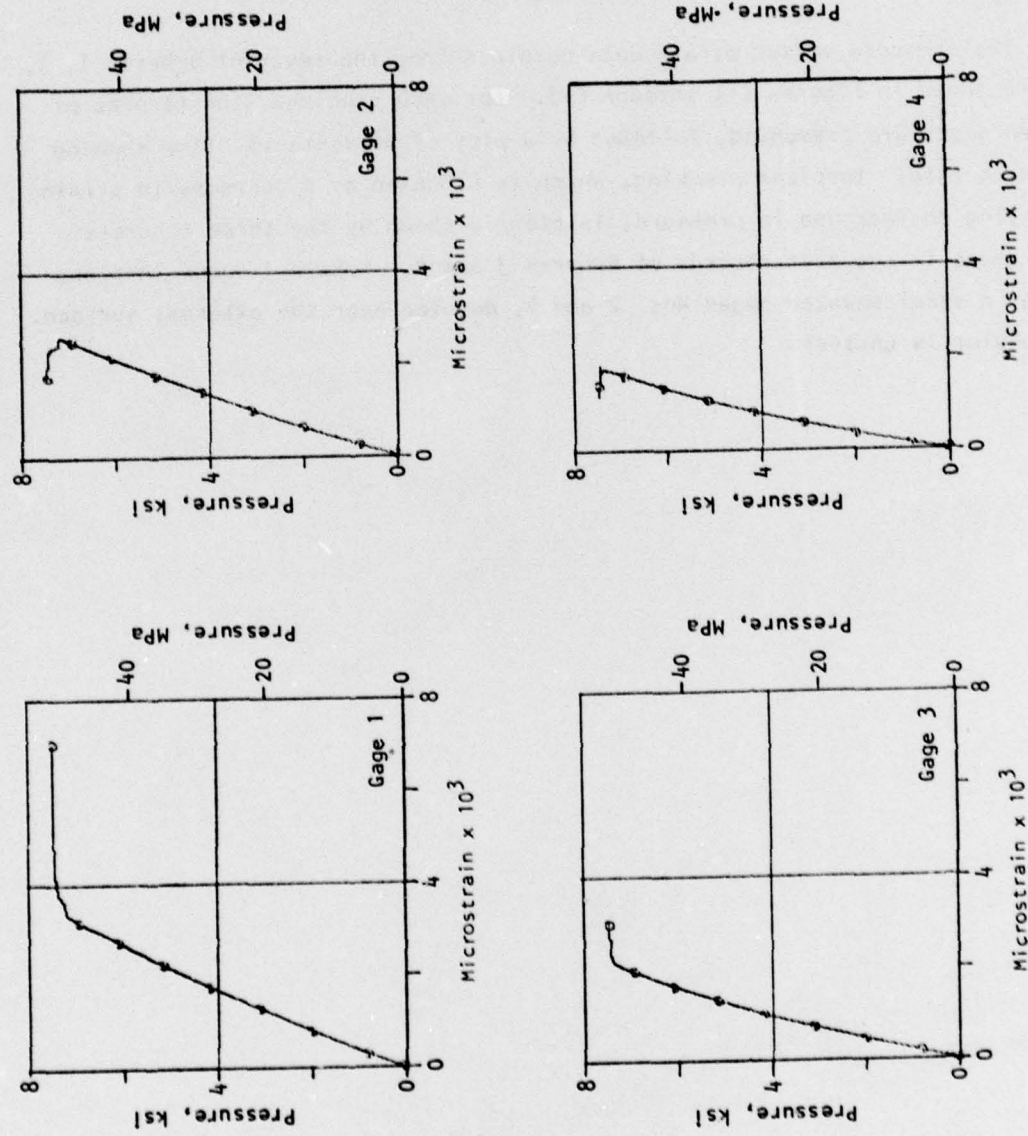


Figure C-1. Pressure/strain data for Sphere 1.

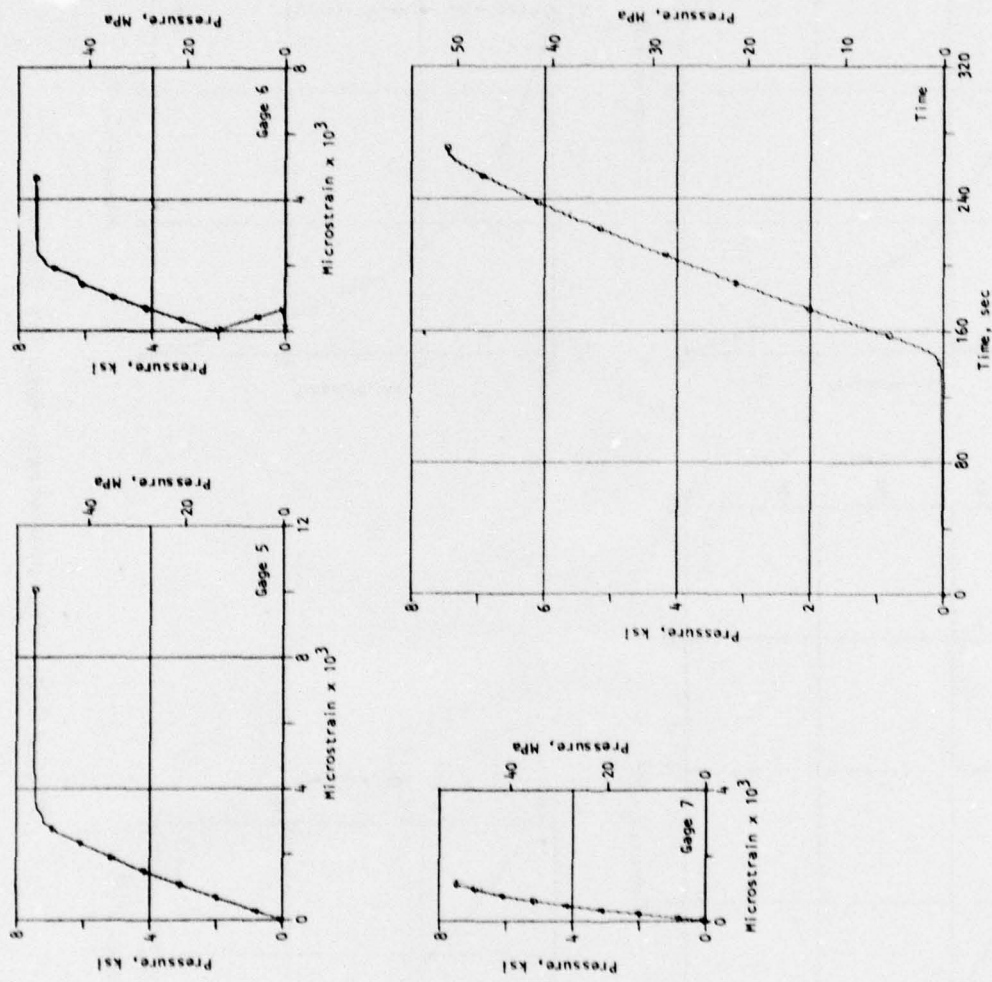


Figure C-1. (Concluded).

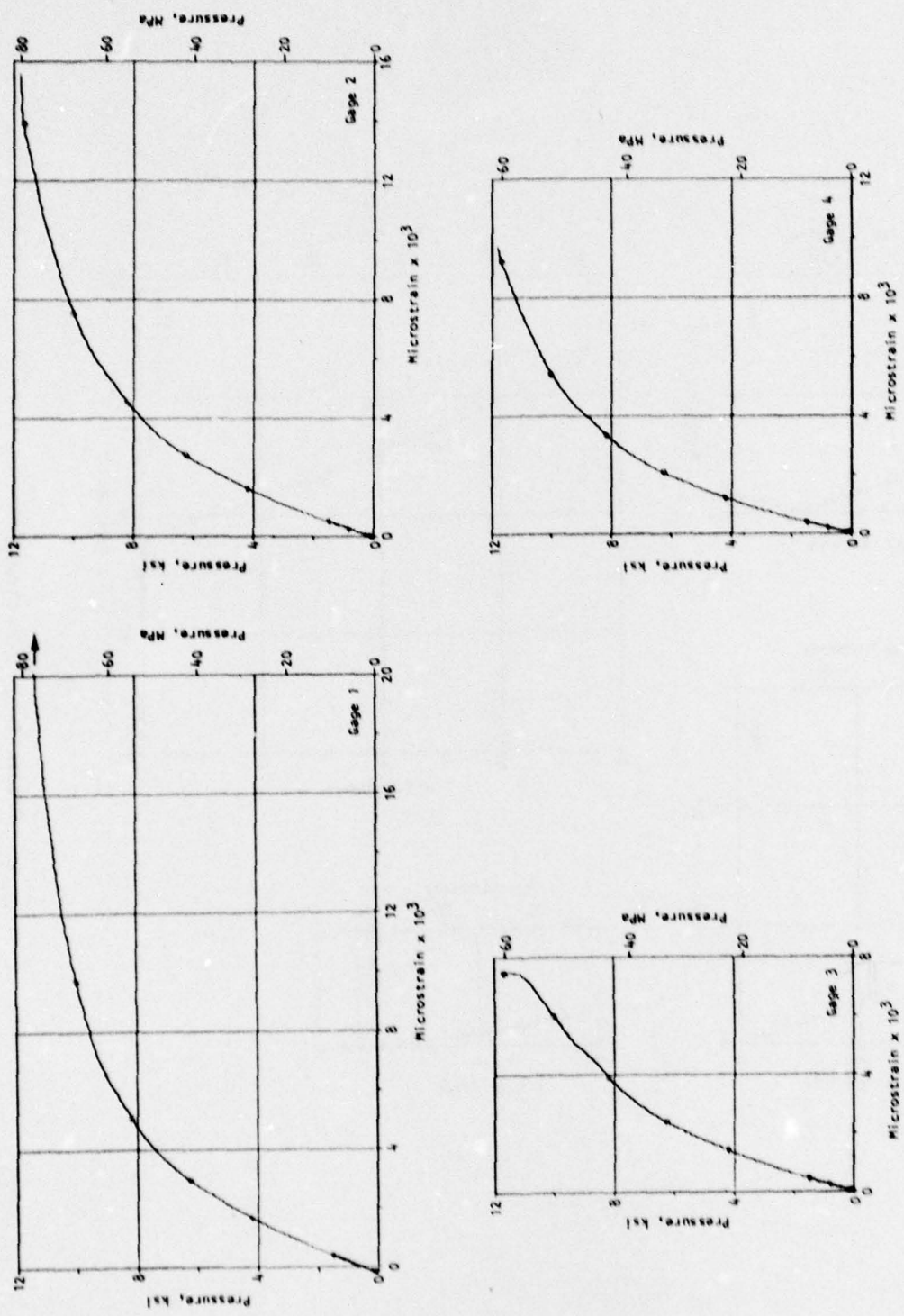


Figure C-2. Pressure/strain data for Sphere 3.

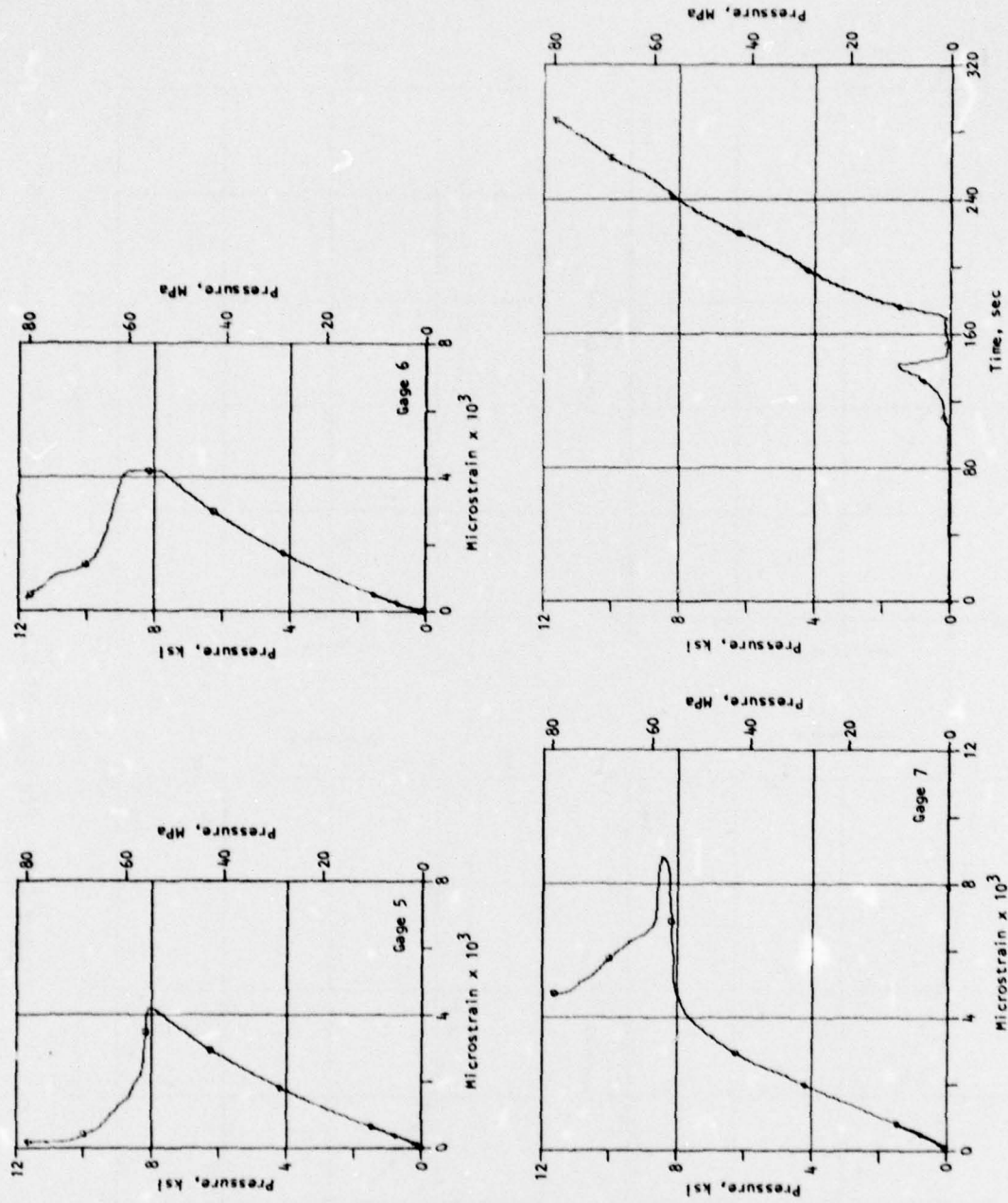


Figure C-2. (Concluded).

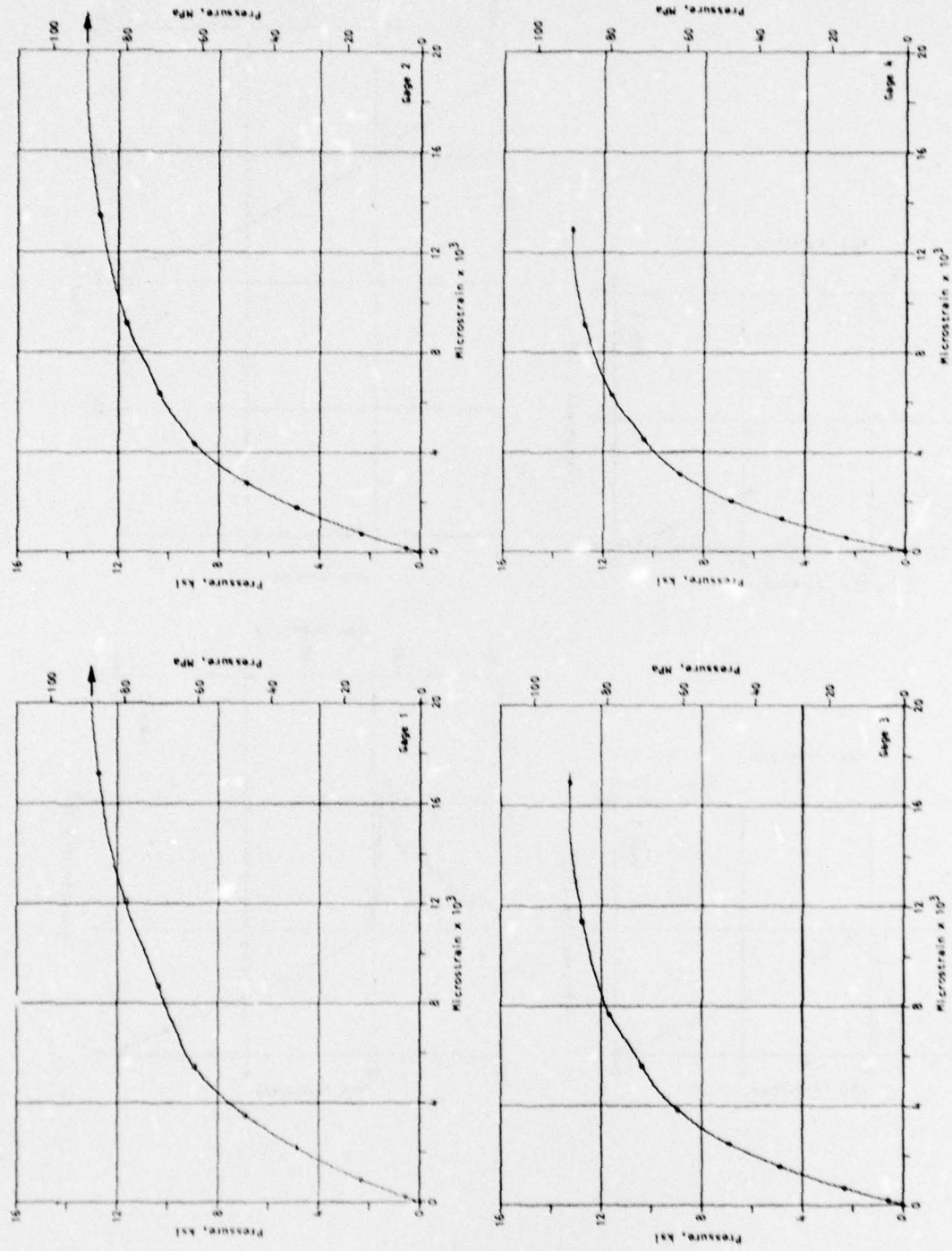


Figure C-3. Pressure/strain data for Sphere 4.

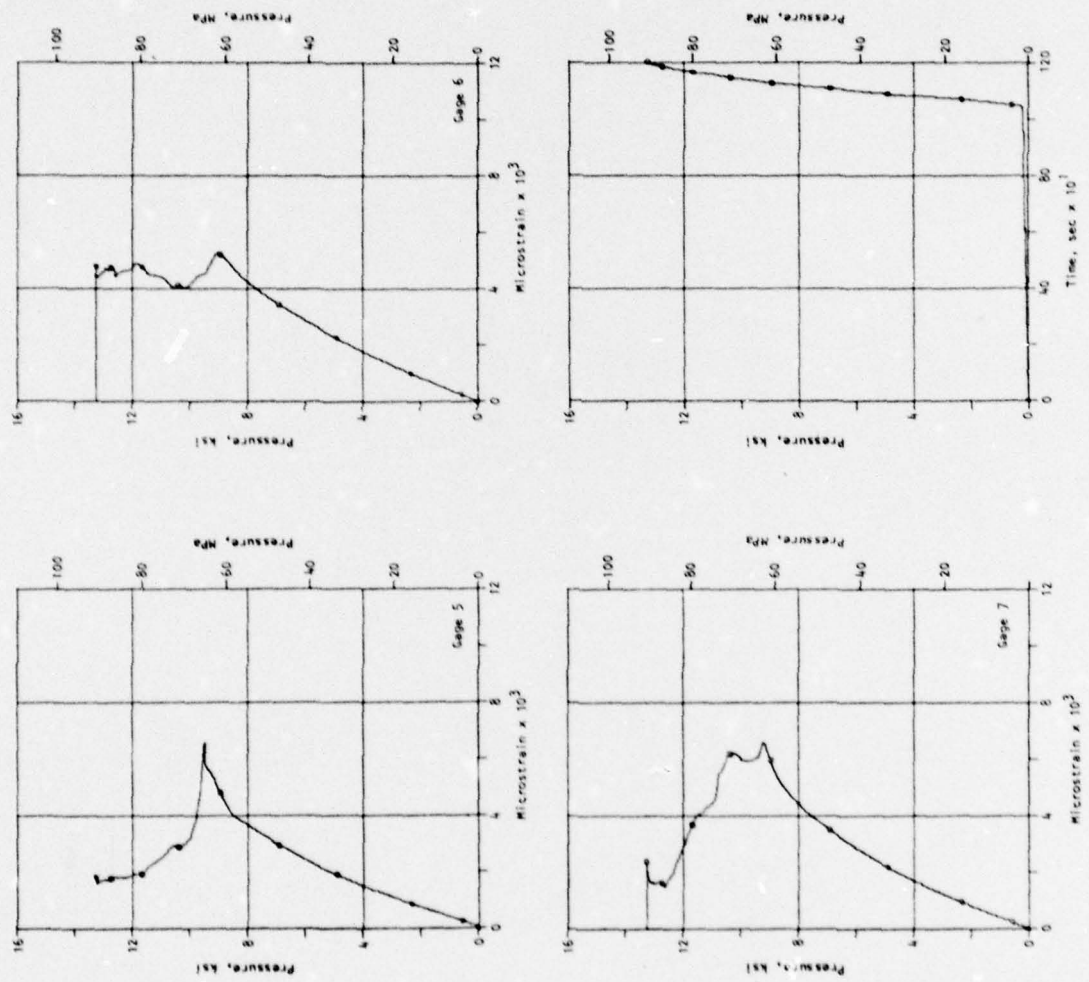
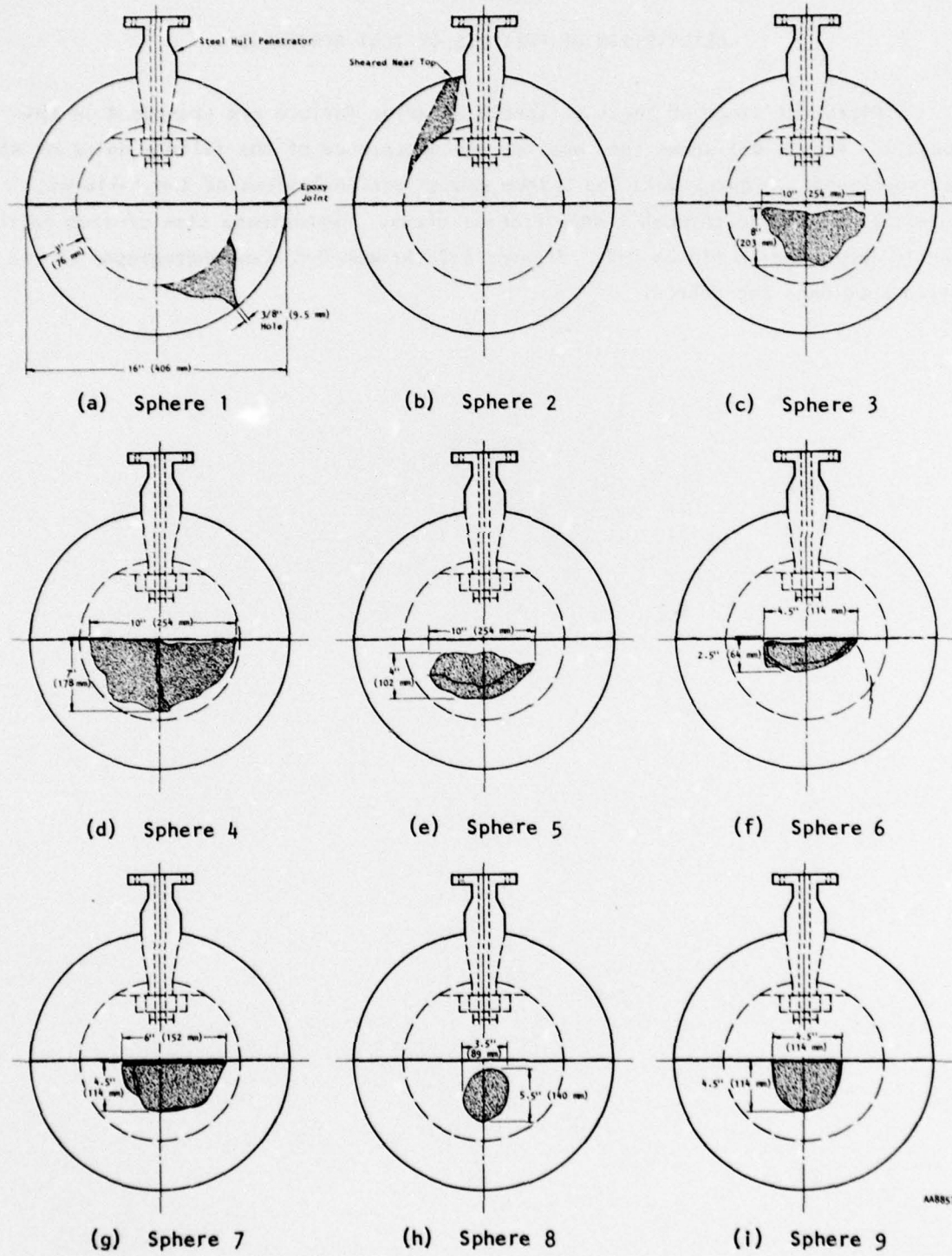


Figure C-3. (Concluded).

APPENDIX D  
DESCRIPTION OF FAILURES OF TEST SPECIMENS

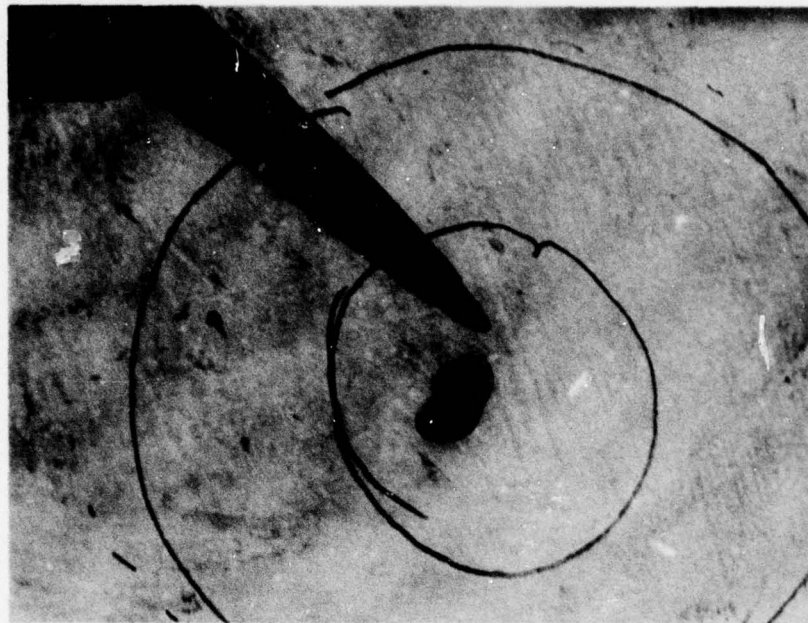
Pictorial views of the test specimens after failure are presented in this appendix. Figure D-1 shows the location and appearance of the failure holes of all test specimens. Figures D-1a and b show cross-sectional views of the failures, whereas Figures D-1c through i show frontal views. Approximate size of each failure zone is indicated in Figure D-1. Figures D-2 through D-8 show photographs of the failed specimens and debris.

PRECEDING PAGE BLANK

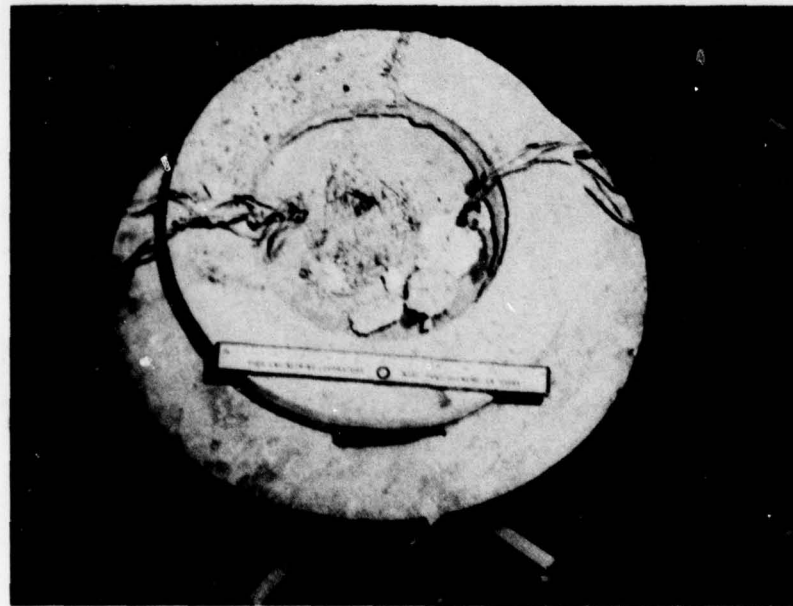


AA8857

Figure D-1. Failures in test specimens.



(a) Outer view

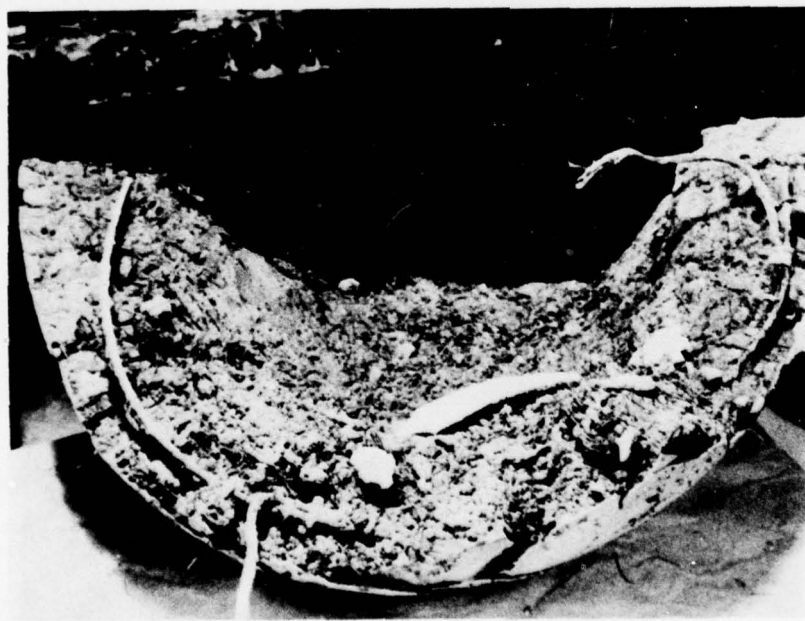


(b) Inner view

Figure D-2. Failure of Sphere 1.



(a) View of failure area



(b) Failed area showing steel rebar

Figure D-3. Failure of Sphere 2.



(c) Bent steel fiber on concrete surface

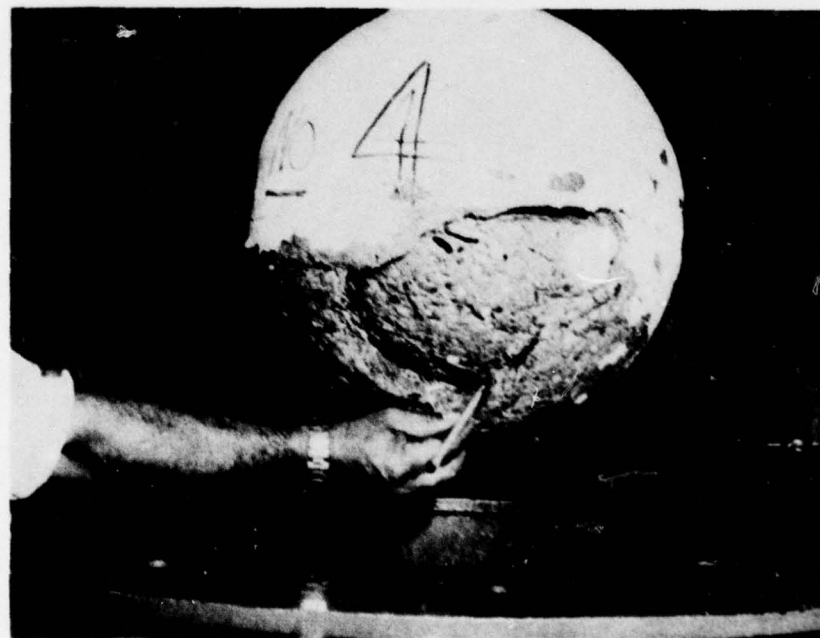


(d) View of sheared surface area

Figure D-3. (Concluded).

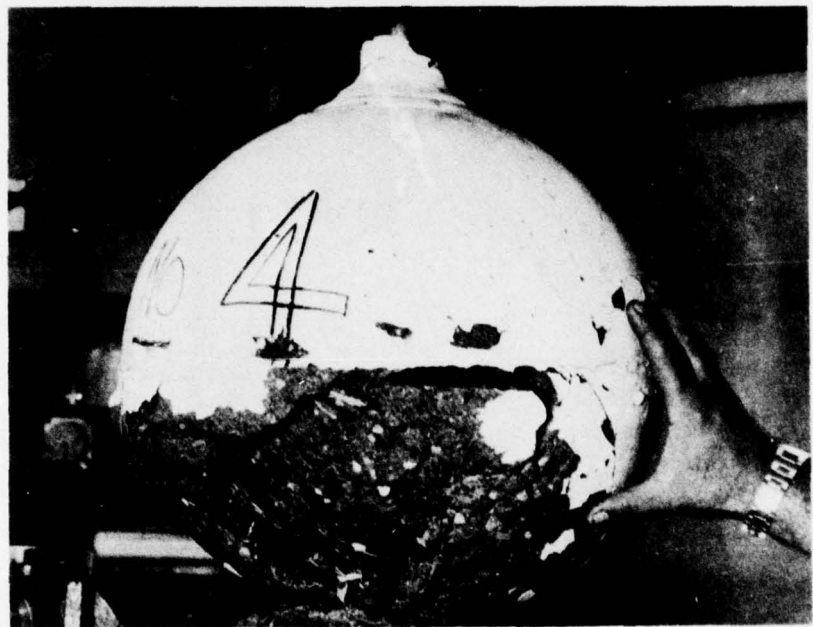


(a) Overall view of implosion area



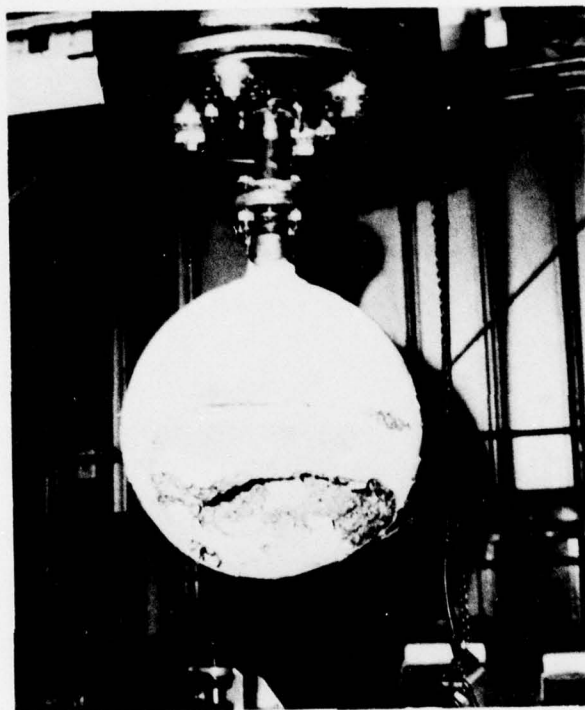
(b) View showing portion of wall pushed in

Figure D-4. Failure of Sphere 4.

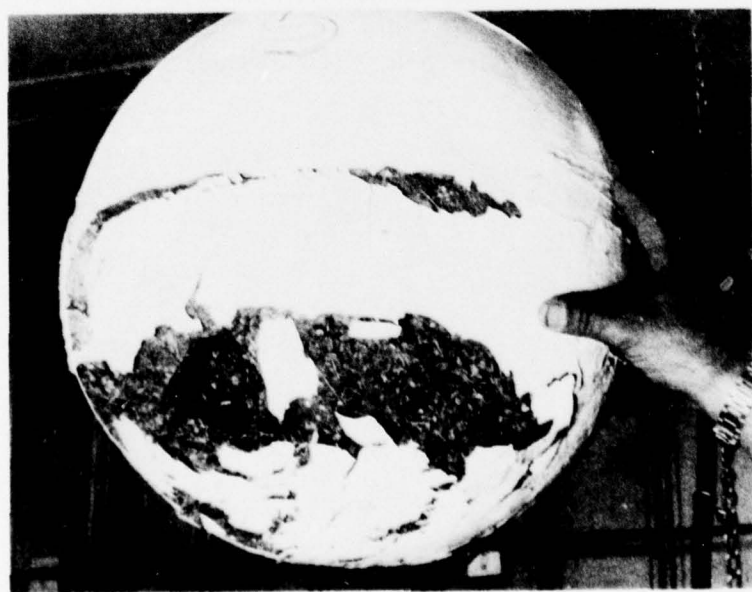


(c) Side view showing implosion area

Figure D-4. (Concluded).

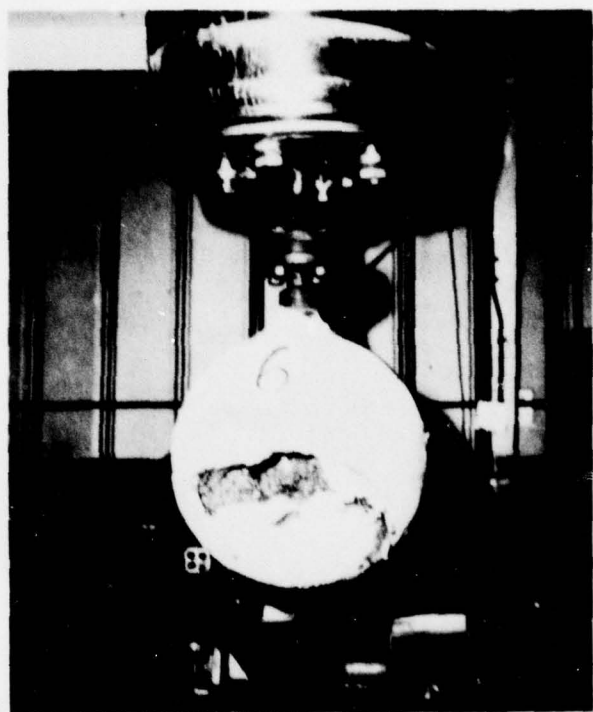


(a) View of implosion area

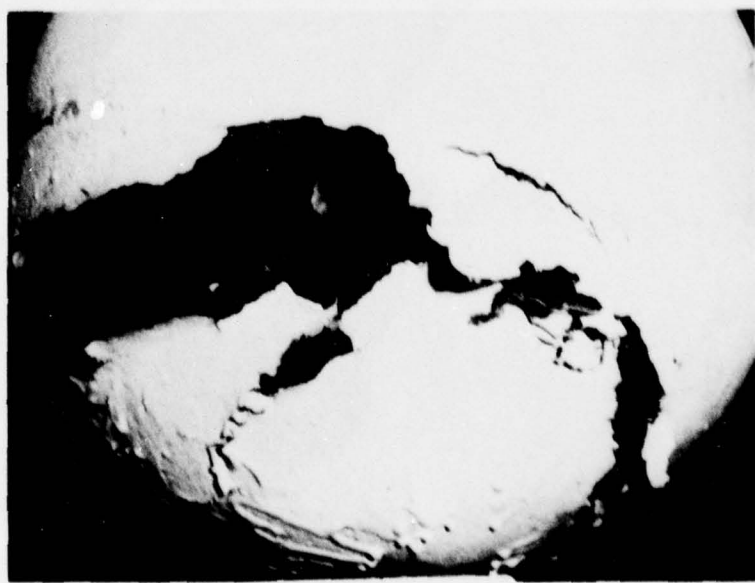


(b) Close-up view

Figure D-5. Failure of Sphere 5.



(a) View of implosion area



(b) Close-up view of implosion area

Figure D-6. Failure of Sphere 6.

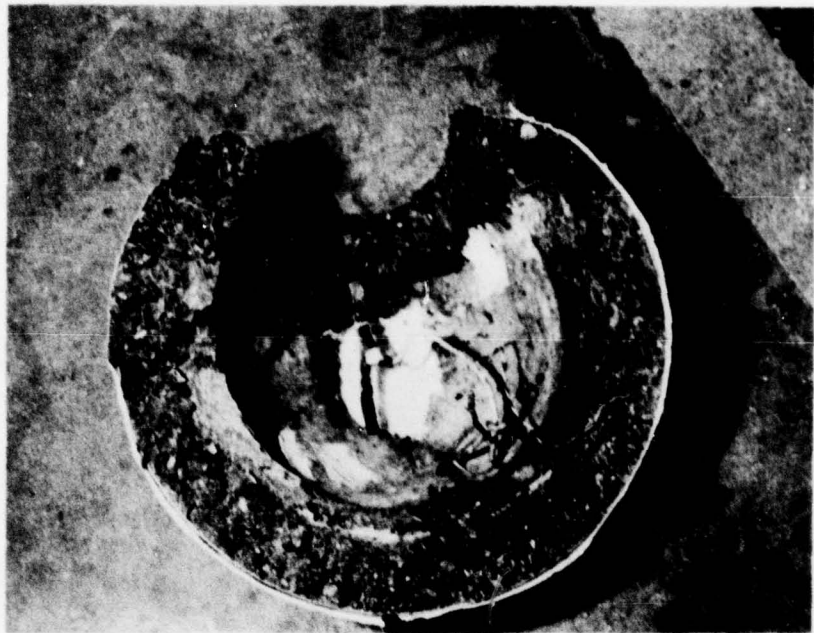


(a) Side view of implosion area



(b) View of circular implosion hole

Figure D-7. Failure of Sphere 7.

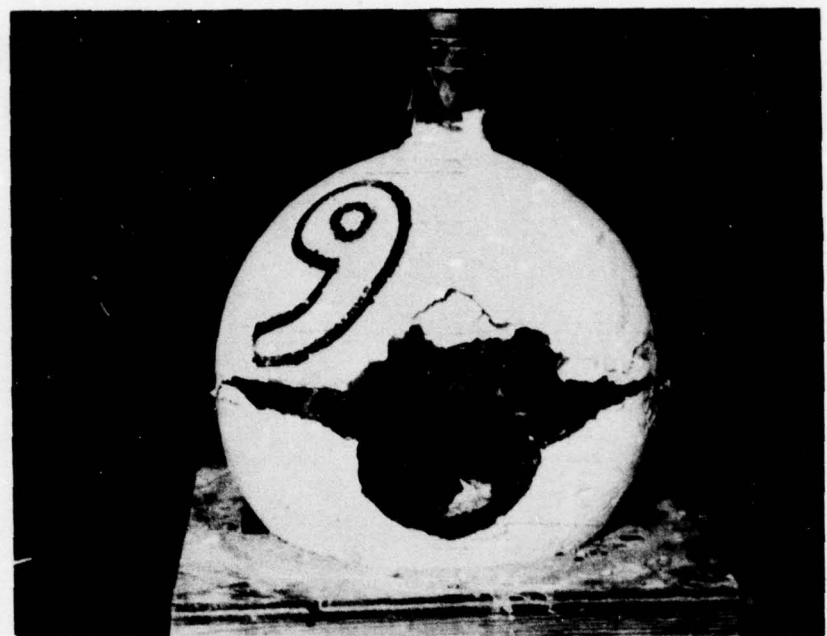


(c) Bottom hemisphere implosion area



(d) Upper hemisphere

Figure D-7. (Concluded).

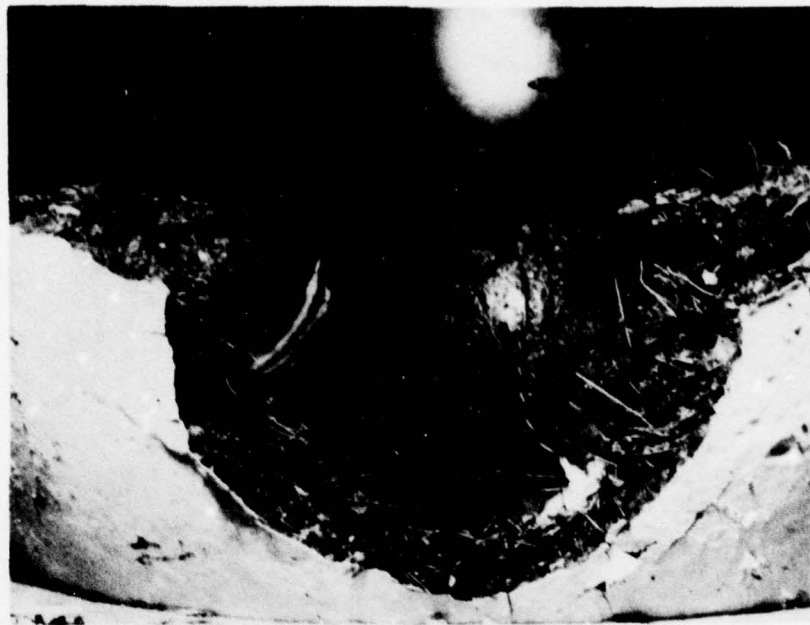


(a) Implosion area



(b) Bottom hemisphere

Figure D-8. Failure of Sphere 9.



(c) Close-up view of bottom hemisphere



(d) Close-up view showing wire fiber

Figure D-8. (Concluded).

APPENDIX E  
STRAIN DATA FROM CYCLIC LOAD TESTS

The pressure vs. strain data recorded during the cyclic tests of Spheres 6 through 9 are shown in Figures E-1 through E-4. As in the case of single-load implosion test data, the strains recorded by the seven strain gages are presented, followed by a plot of pressure vs. time.

The data from Spheres 7 through 9 are plotted to a larger scale. The data from the concrete-mounted Gage Nos. 5, 6, and 7 tend to be erratic after the first few cycles as a result of progressive local deterioration of the concrete near the inner surface. Accordingly, these strain records must be interpreted with caution. Some of these gages indicated tensile strains after an initial period. Since the tensile strains do not represent meaningful physical phenomena, they have been omitted in some of the plots.

PRECEDING PAGE BLANK

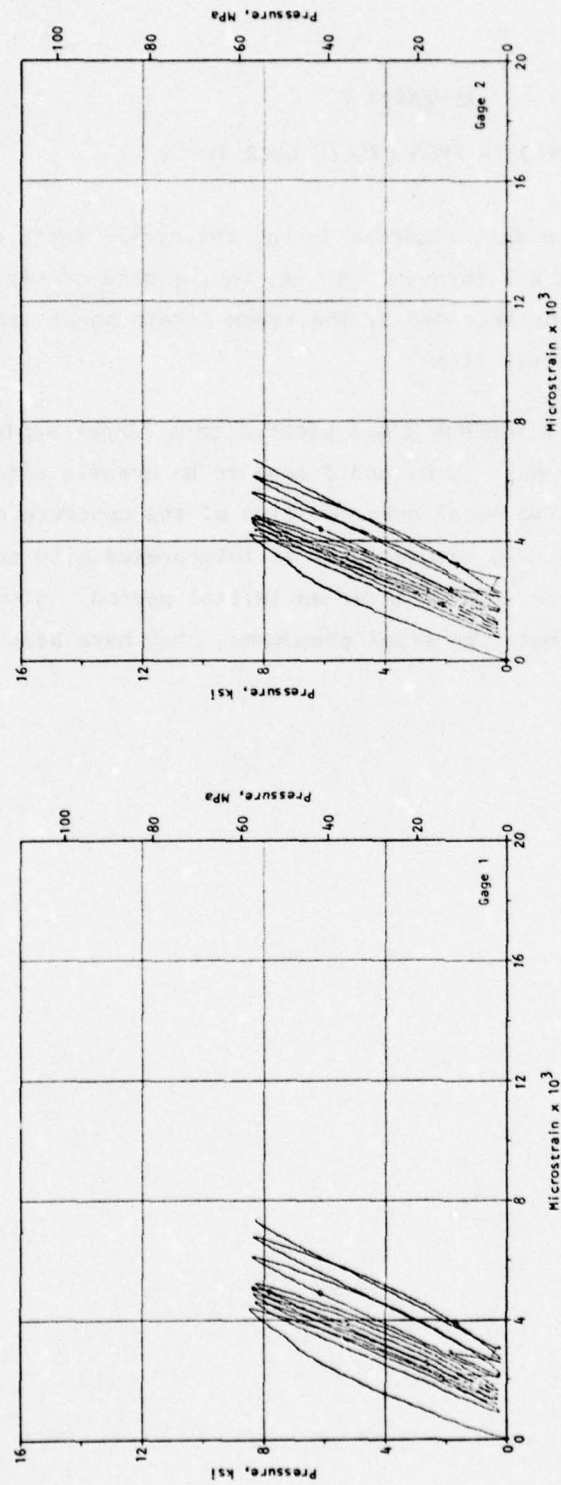


Figure E-1. Pressure/strain data from cyclic test of Sphere 6.

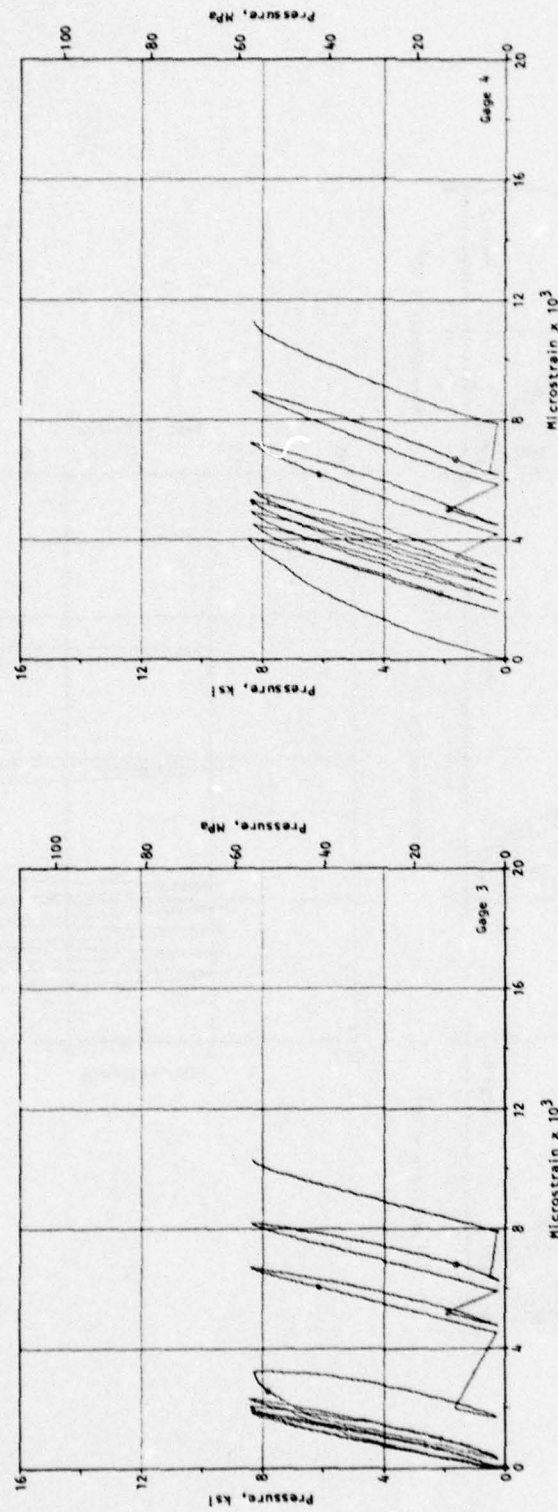


Figure E-1. (Continued).

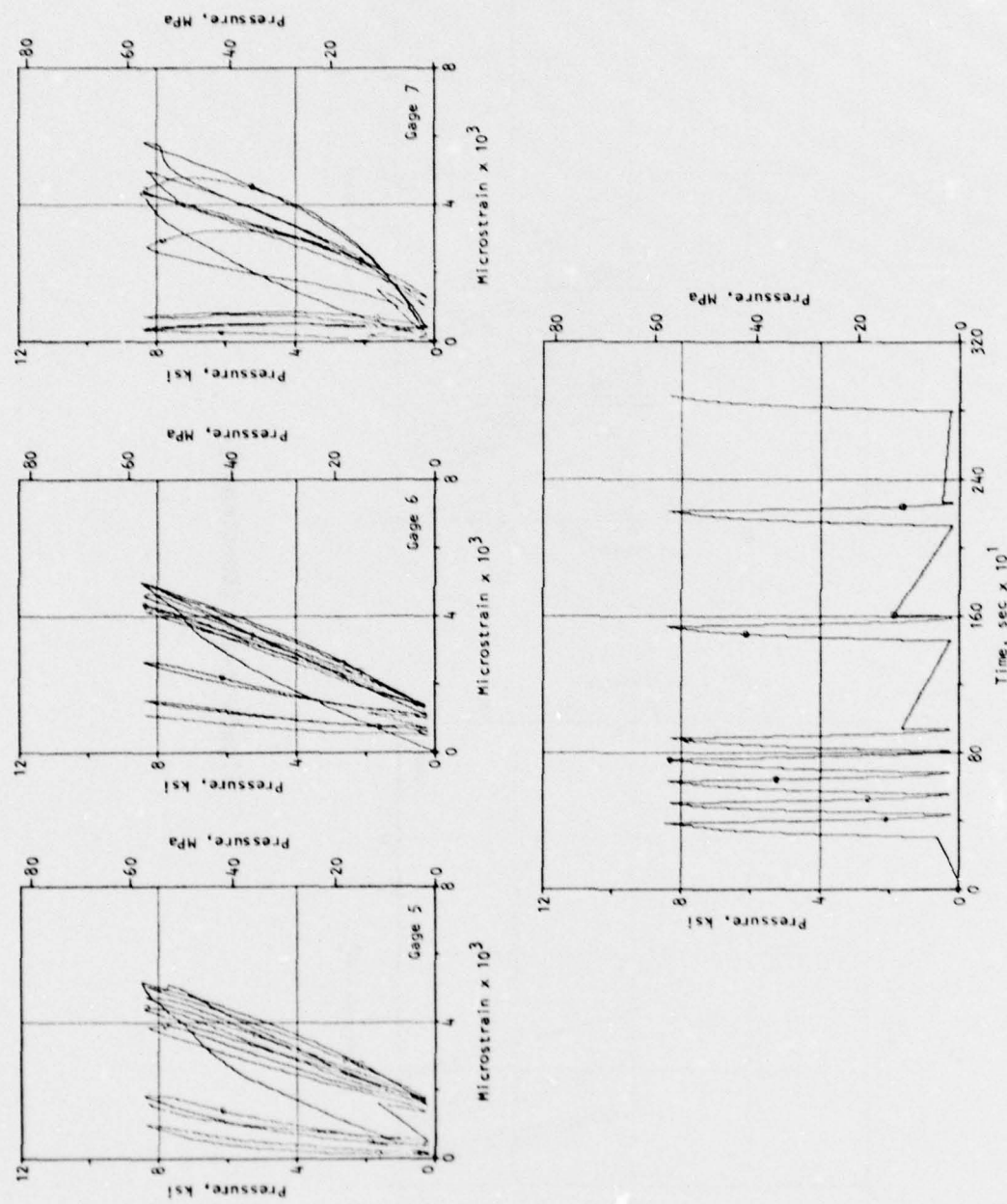


Figure E-1. (Concluded).

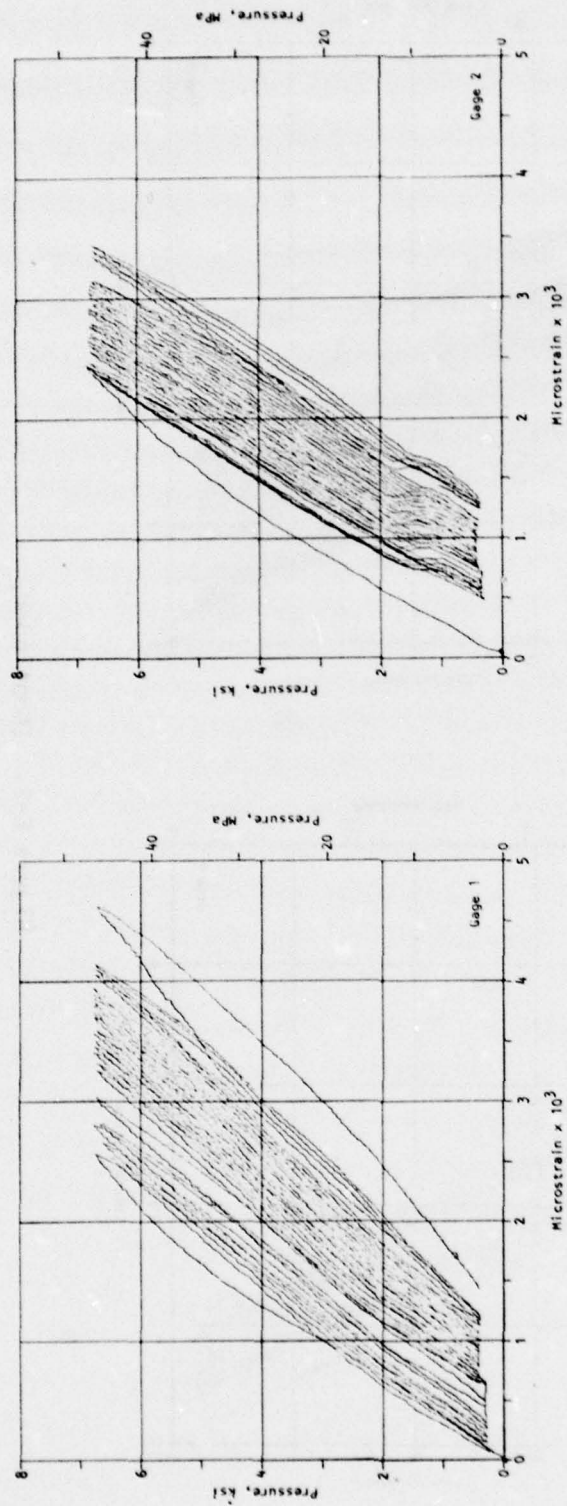


Figure E-2. Pressure/strain data from cyclic test of Sphere 7.

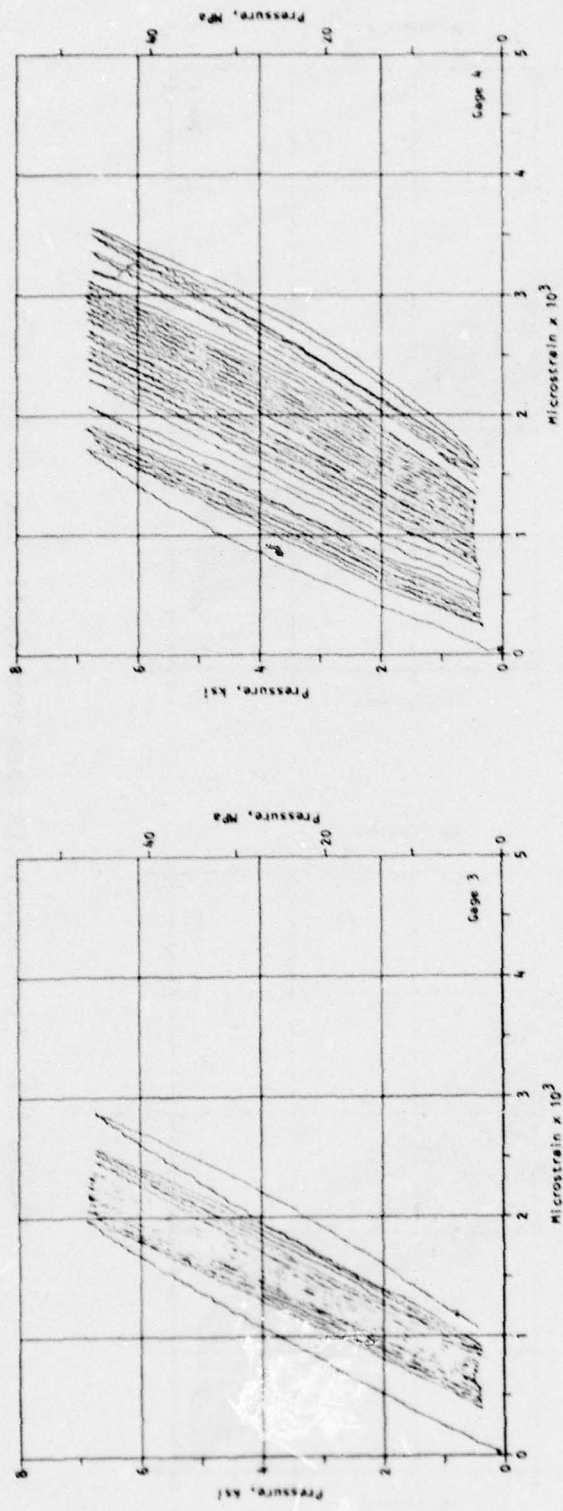


Figure E-2. (Continued).

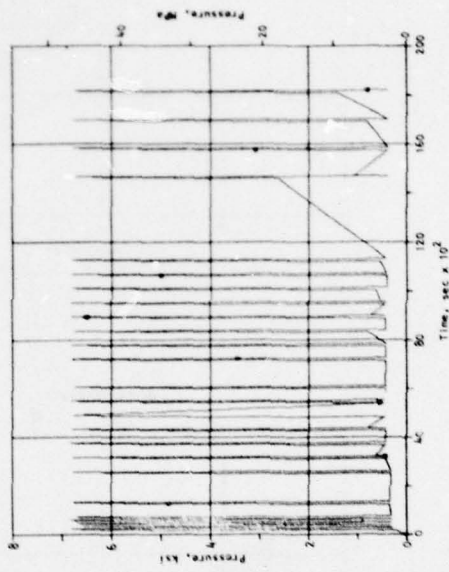
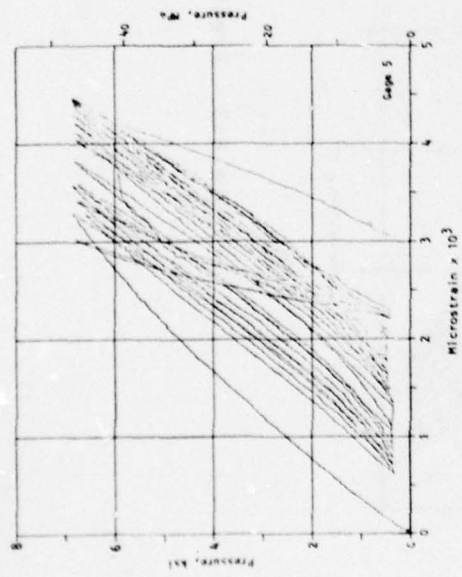
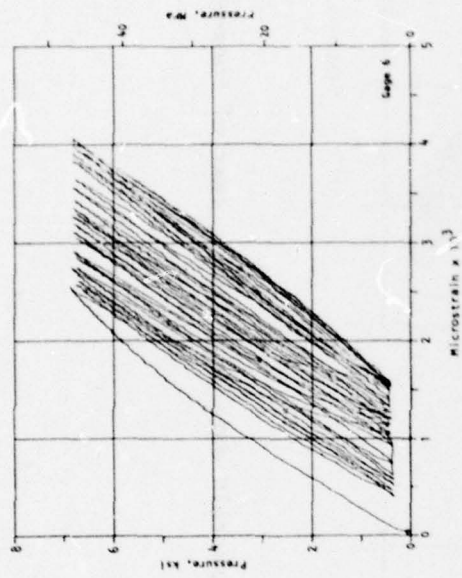
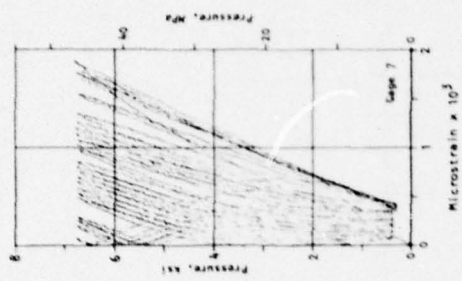


Figure E-2. (Concluded).

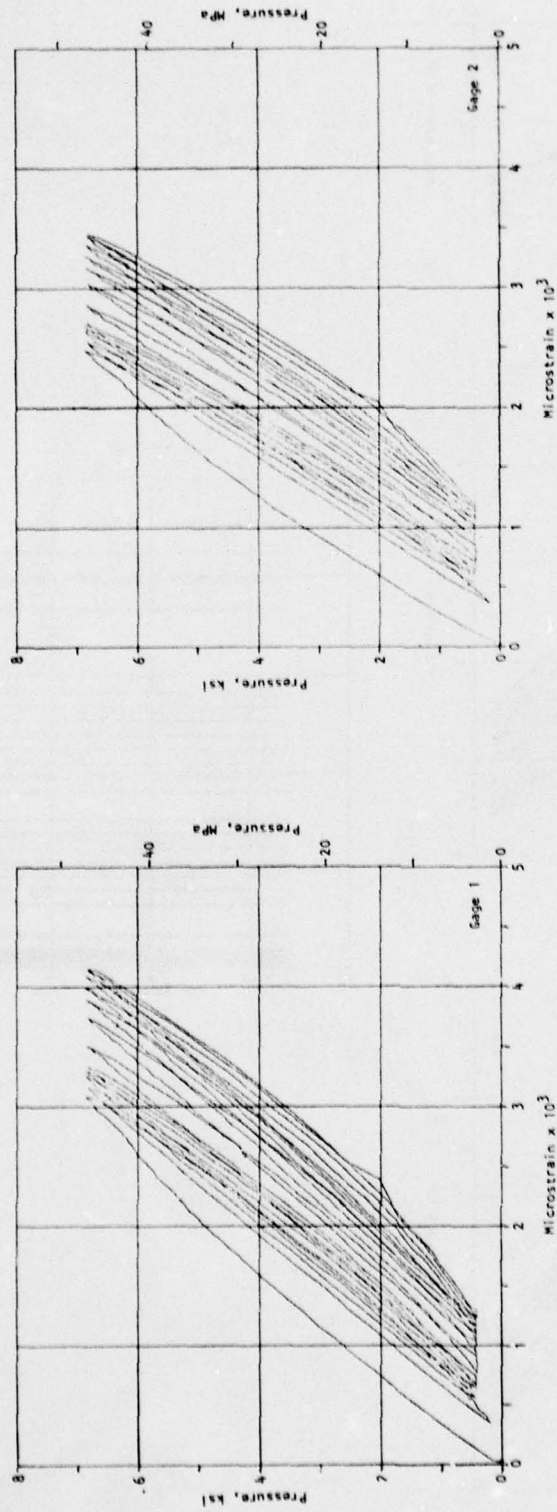


Figure E-3. Pressure/strain data from cyclic test of Sphere 8.

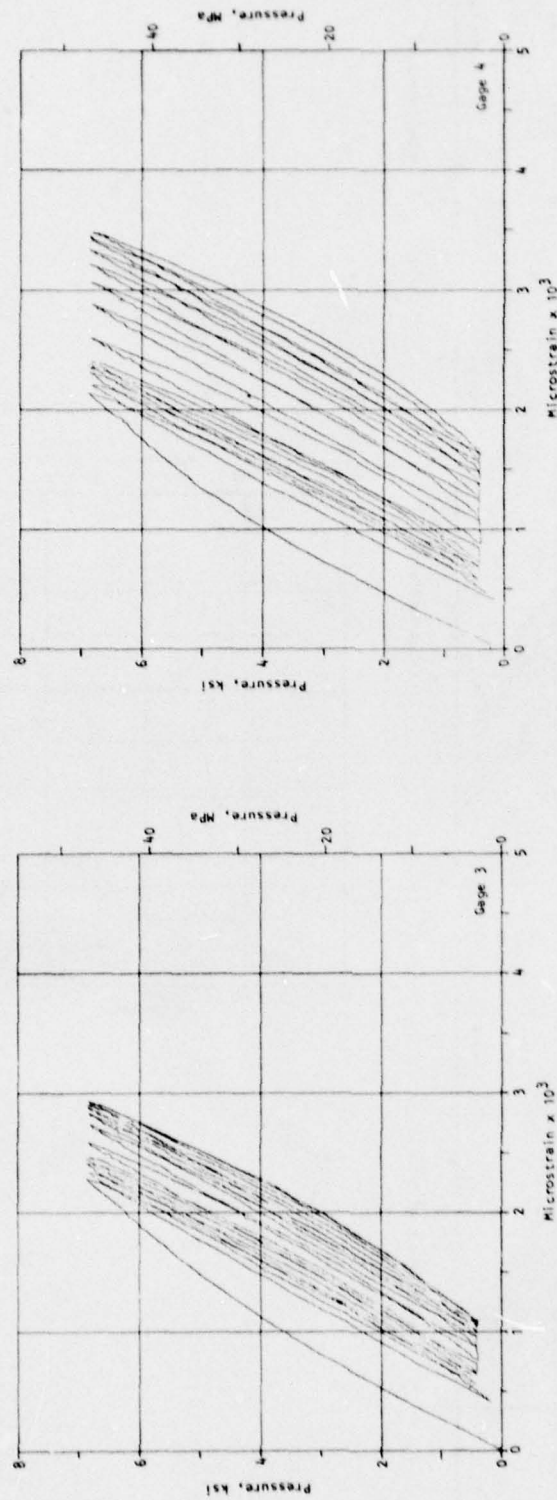


Figure E-3. (Continued).

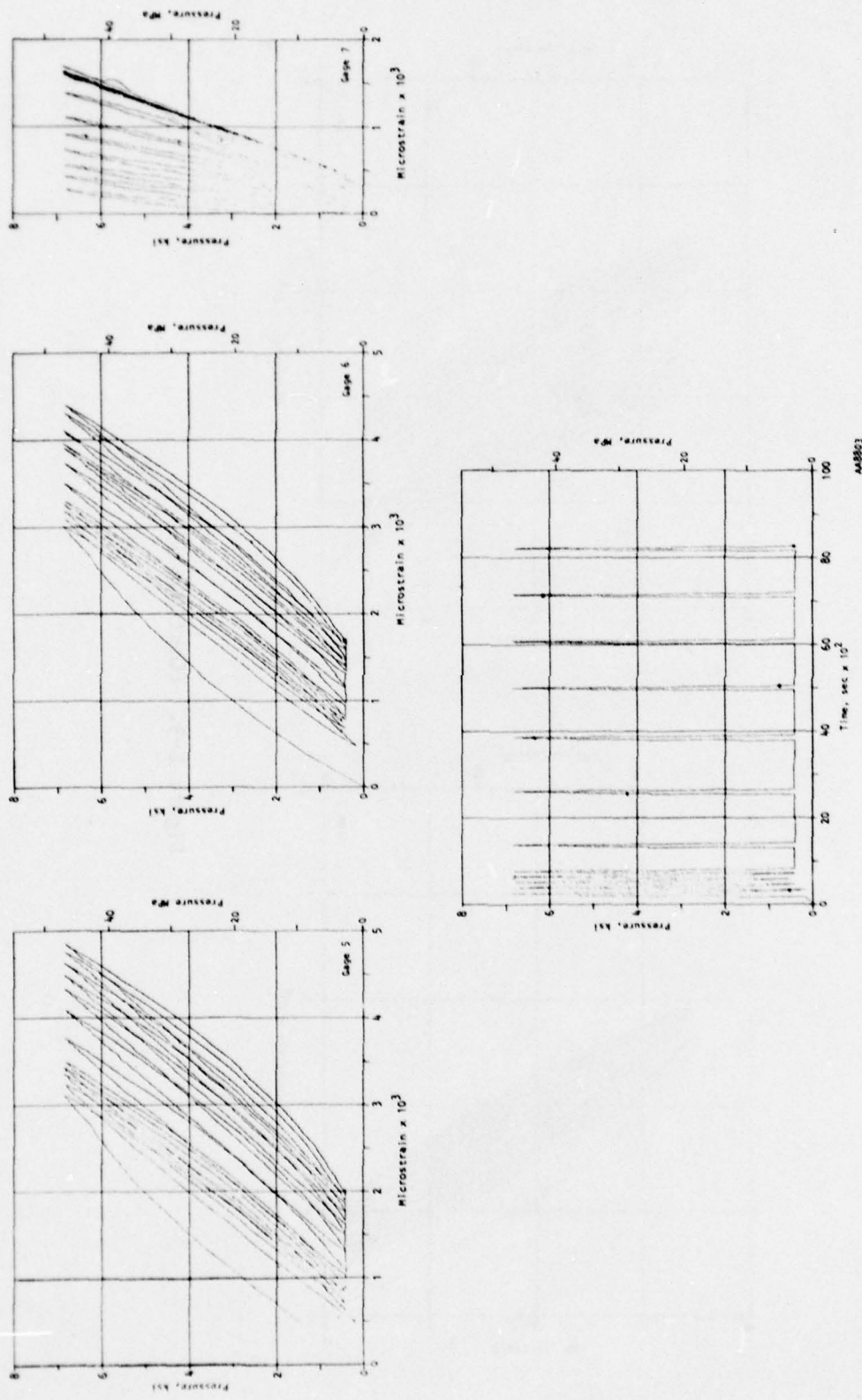


Figure E-3. (Concluded).

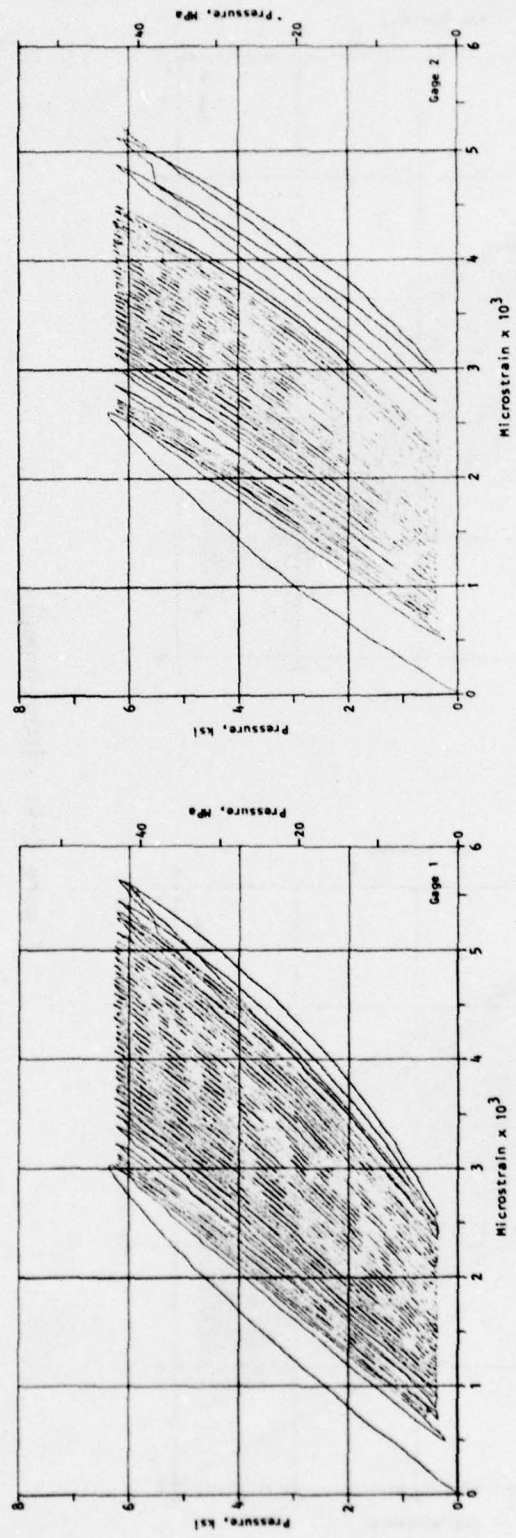


Figure E-4. Pressure/strain data from cyclic test of Sphere 9.

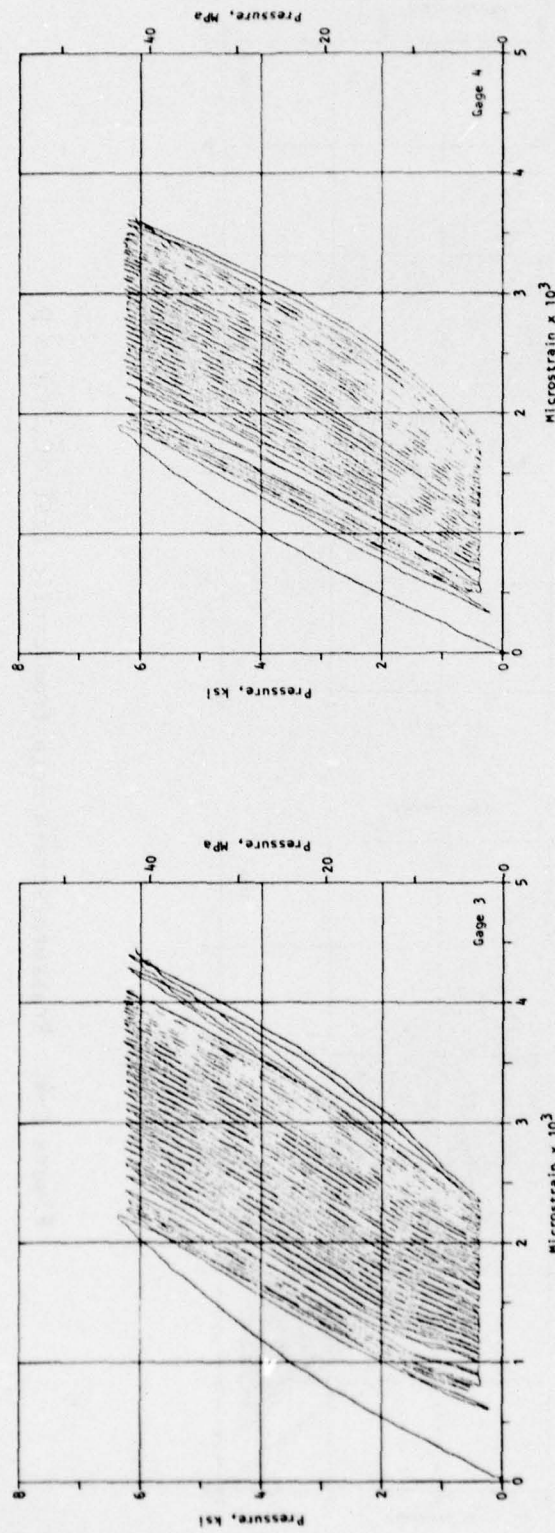


Figure E-4. (Continued).

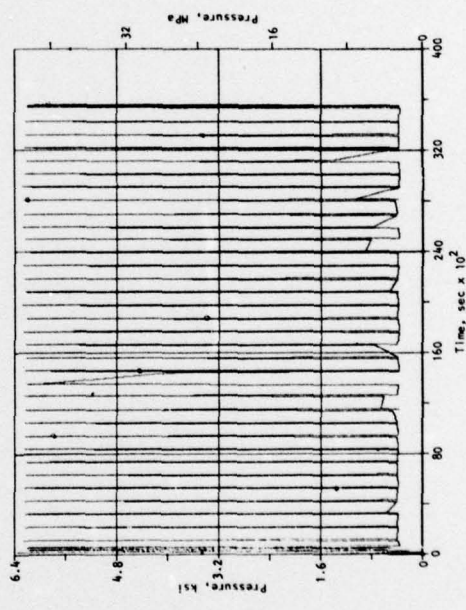
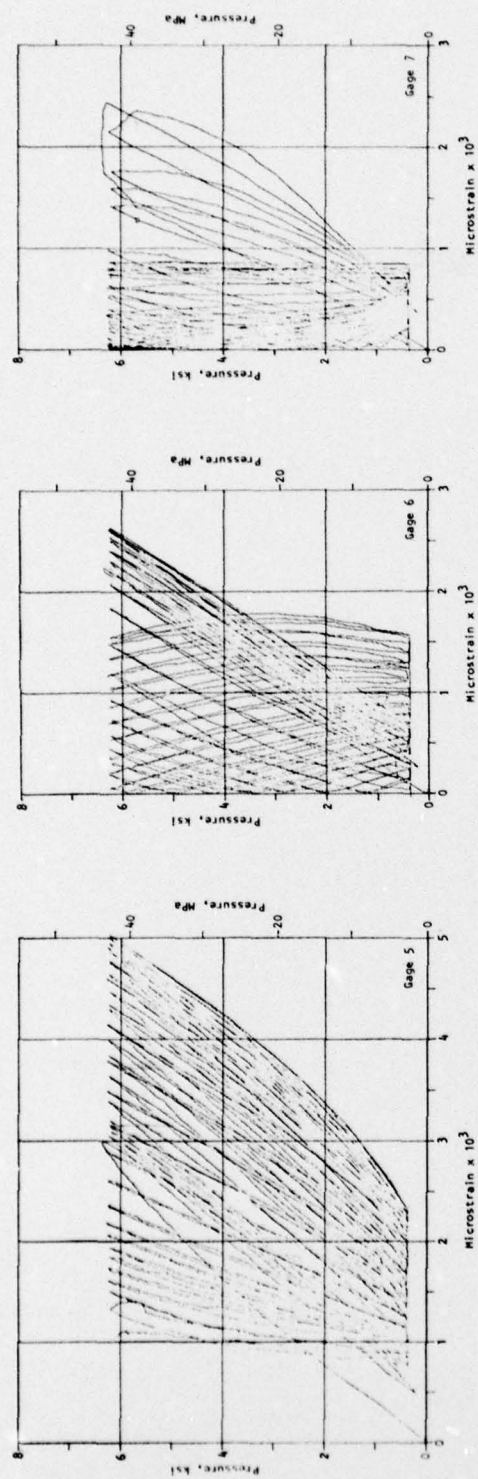


Figure E-4. (Concluded).

## APPENDIX F

### REVIEW OF LOW-CYCLE FATIGUE DATA ON ROCK AND CONCRETE

Pertinent details of some earlier investigations are summarized in Table F-1. The data on rock (Ref. F-1) are plotted in Figure F-1 and those on concrete (Refs. F-2, F-3, and F-4) in Figure F-2. For the axial compression tests (Refs. F-1 through F-3), the vertical axes of Figures F-1 and F-2 represent the ratio of the cyclic test stress to the static unconfined compression strength. The data of Reference F-2 and F-3 plot along the same line on the fatigue plot.

The load parameter in the flexural tests of Batson et al. (Ref. F-4) was the first-crack strength, defined as the point at which the load-deflection curve becomes nonlinear. The vertical axis in Figure F-2 for their data represents the cyclic-test stress normalized with respect to the static first-crack strength, the stresses being computed from the elastic flexure equations. This approach is analogous to the use of  $P_{p1}$  as the primary reference in the present program.

Figure F-2 shows two plots from data of Reference F-4 taken from specimens with two kinds of fiber reinforcement, as follows:

Fiber 1: 2.98% by volume, 0.0066 in. dia. x 0.5 in. long  
(0.17 mm x 12.7 mm)

Fiber 2: 2.98% by volume, 0.014 in. dia. x 1.23 in. long  
(0.36 mm x 31.8 mm)

It is noteworthy that the fatigue data from fiber-reinforced concrete under flexure and plain concrete under compression are very similar. The rock and concrete data are fitted with an equation of the type of Equation 5-3. The values of  $m$  so obtained are shown in Table F-2.

Figure F-3 (Ref. F-6) compares low-cycle fatigue data on several types of rock. The initial slopes (a few hundred cycles) of some of these curves are much steeper than in the regions representing longer life. The  $m$  values corresponding to the initial slopes are shown in Table F-2.

PRECEDING PAGE BLANK

Table F-1. Investigations on low-cycle fatigue behavior of rock and concrete.

Reference	Investigators	Material(s)	Loading	Sample Type and Size	Testing Rate
F-1	Hardy-Chugh	Tennessee Sandstone Indiana Limestone Barre Granite	Axial compression	Cylinders 1 in. dia. x 2.5 in. long (25 mm x 64 mm)	0.25 Hz
F-2	Awad-Hilsdorf	Plain Concrete: 28-day strength 4000 psi (27.6 MPa)	Axial compression	Prisms 4 in. x 4 in. x 12 in. (102 mm x 102 mm x 305 mm)	6000 psi/min (0.69 MPa/s)
F-3	Bennett-Raju*	Plain Concrete (?)	Axial compression	--	--
F-4	Batson et al.	Fiber-reinforced Concrete: strength, 4940 to 5097 psi (34.1 to 35.1 MPa)	Flexure: third-point loading over span of 96 in. (2438 mm)	4 in. x 6 in. (102 mm x 152 mm) cross section 102 in. long (2591 mm)	3 Hz

\* Details not available; tests covered a range from several tens to several millions of cycles and stress levels from 85% to 65% of the static compression strength. For earlier related work, see Reference F-5.

Table F-2. Regression fit to fatigue data on rock and concrete.

Material	Source	m
Barre Granite		30.22
Tennessee Sandstone	Hardy-Chugh (Ref. F-1)	52.58
Indiana Limestone		34.65
Concrete	Awad-Hilsdorf (Ref. F-2)	27.62
Concrete	Bennett-Raju (Ref. F-3)	27.02
Fiber-Reinforced Concrete Fiber No. 1	Batson et al. (Ref. F-4)	34.55
Fiber-Reinforced Concrete Fiber No. 2		81.83
White Tennessee Marble		6.64*
Westerly Granite	Haimson (Ref. F-6)	13.3*
Berea Sandstone		26
Fiber-Reinforced Concrete Spheres Pressure, ksi	Present program	8.37
Normalized pressure $P/\bar{P}_{im}$		8.6

\*Calculated from initial slope of S-N Curve (<100 cycles).

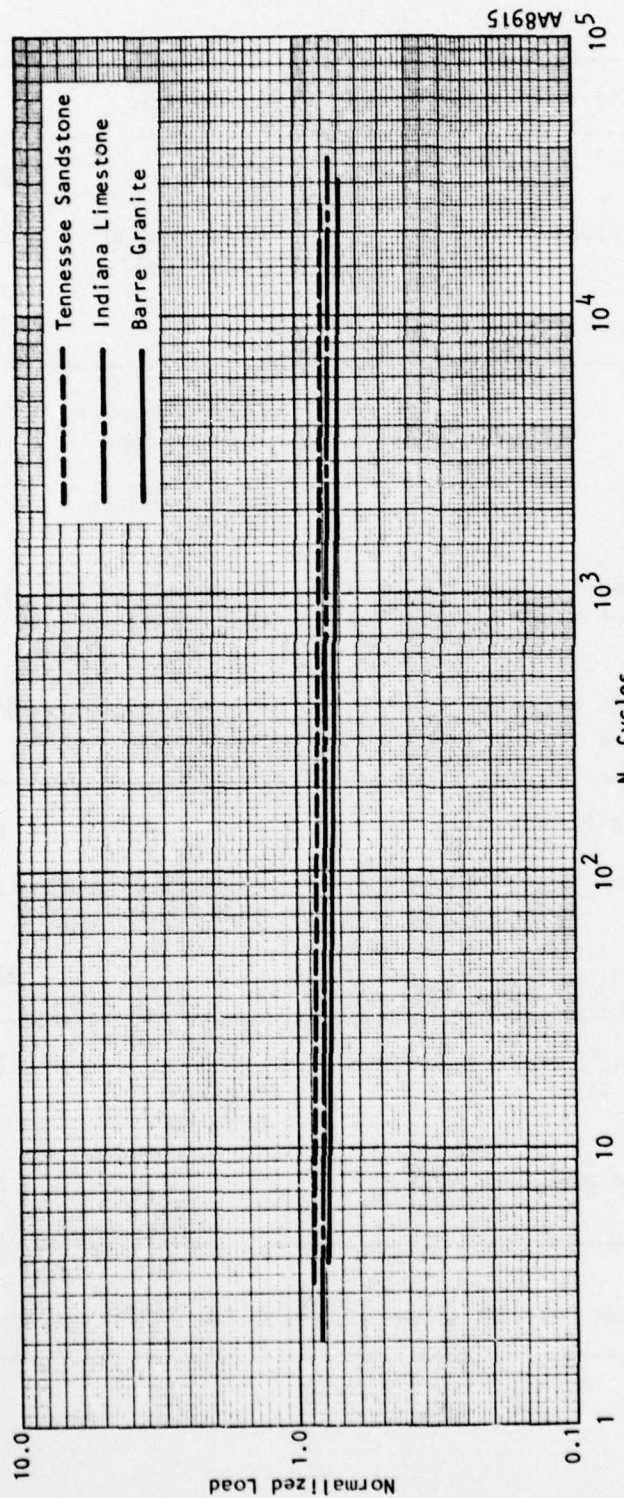


Figure F-1. Fatigue data on rock from Reference F-1.

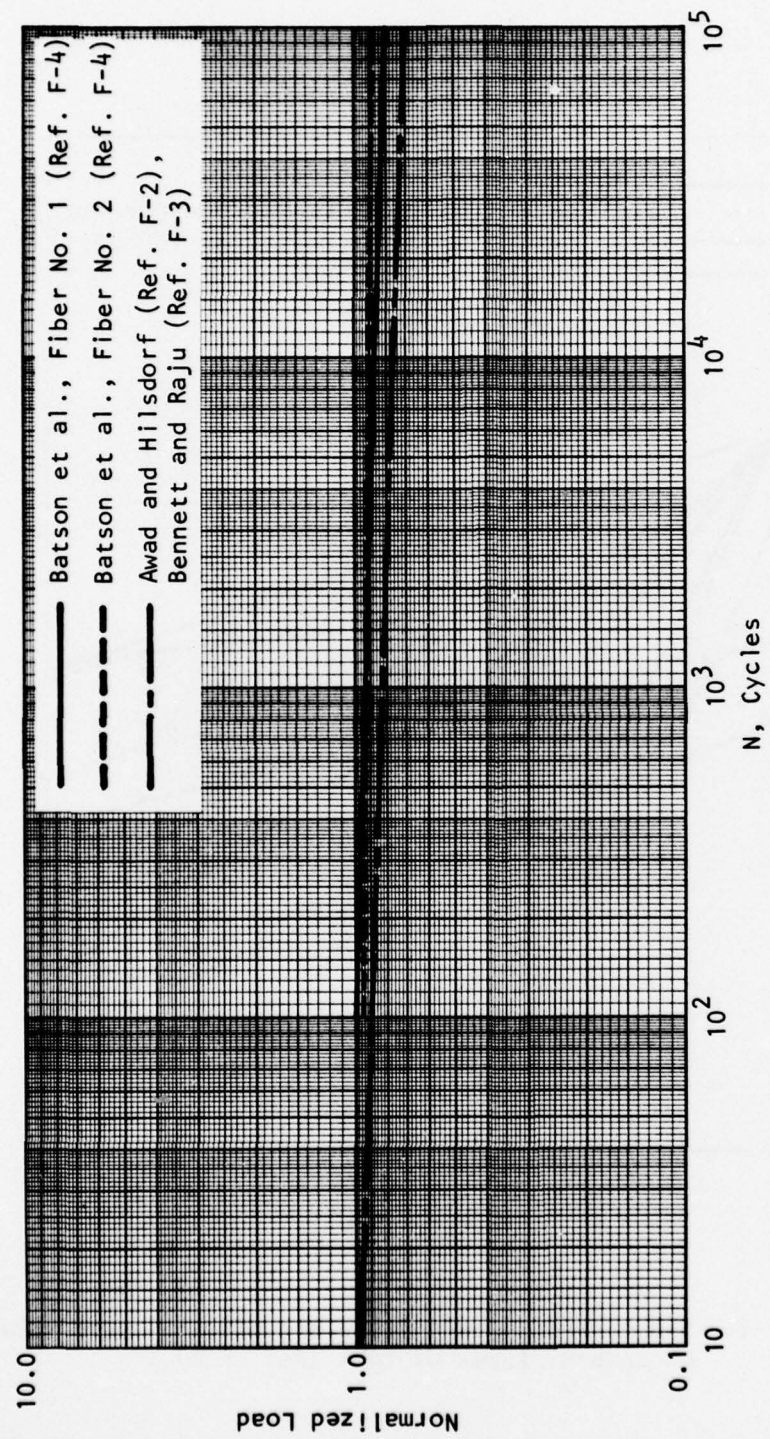


Figure F-2. Fatigue data on concrete from References F-2 to F-4.

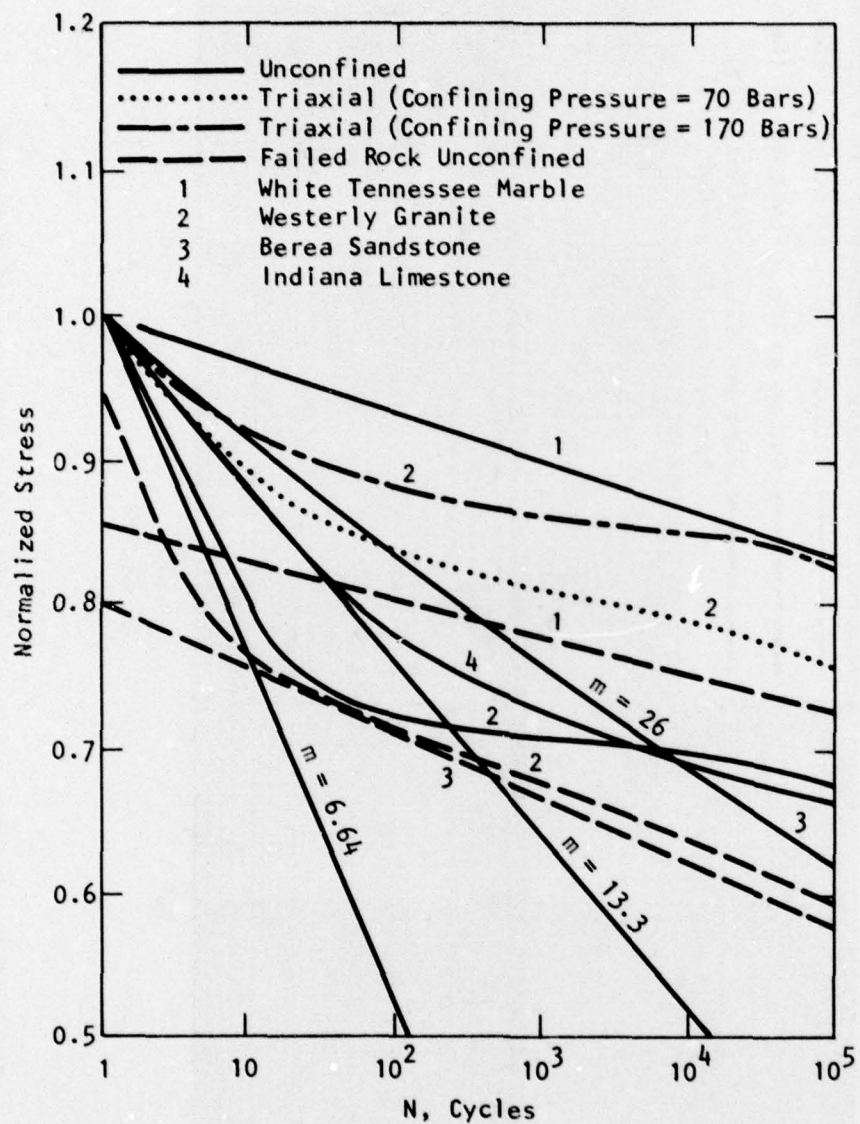


Figure F-3. S-N curves in unconfined and triaxial compression on several types of rock (Ref. F-6).

## REFERENCES

- F-1. Hardy, H.R. and Chugh, Y.P. "Failure of Geologic Materials under Low-Cycle Fatigue," in *Sixth Canadian Symposium on Rock Mechanics*. Ottawa, Ont.: Canadian Dept. of Energy, Mines, and Resources, 1971.
- F-2. Awad, M.E. and Hilsdorf, H.K. "Strength and Deformation Characteristics of Plain Concrete Subjected to High Repeated and Sustained Loads," in *Fatigue of Concrete*. Detroit: Amer. Concrete Inst., 1974.
- F-3. Bennett, E.W. and Raju, N.K. "Cumulative Fatigue Damage of Plain Concrete in Compression," *Int. Conf. on Structures, Soil Mech., and Eng. Design*. Southampton Univ., Apr 1969.
- F-4. Batson, G. et al. "Flexural Fatigue Strength of Steel Fiber Reinforced Concrete Beams," *ACI Jnl* 69:11, Nov 1972, pp 673-677.
- F-5. Bennett, E.W. and Muir, S.E. "Some Fatigue Tests on High Strength Concrete in Axial Compression," *Mag. of Conc. Res.* 19:59, Jun 1967.
- F-6. Haimson, B.C. "Mechanical Behavior of Rock under Cyclic Loading," in *Advances in Rock Mechanics*, Proc. 3rd Congress of the International Soc. for Rock Mechanics, Vol. 2, Pt. A, pp 373-378. Washington, DC: Nat'l Academy of Sciences, 1974.

APPENDIX G  
SYMBOLS AND NOTATIONS

$D_o$	Outside diameter of sphere
$E$	Young's modulus
$N$	Total number of applications of the load $Z$
$P$	External pressure
$P_{im}$	External pressure at implosion
$P_{pl}$	External pressure at in-plane cracking
$Q$	Dependent random variable
$R$	Radius
$R_i$	Inside Radius
$R_o$	Outside radius
$X$	Resistance
$X_n$	Mode resistance at start of the application of $Z_n$
$\bar{X}_n$	Best estimate of $\mu_{X_n}$ , the mean (average or expected) value of $X_n$
$X_1$	Mode resistance at the start of the first application of the load $Z$
$\bar{X}_1$	Best estimate of $\mu_{X_1}$ , the mean (average or expected) value of $X_1$
$Y_r$	Independent random variable ( $r = 1, 2, 3, \dots, R$ )
$Z$	Load
$\bar{Z}$	Best estimate of $\mu_Z$ , the mean (average or expected) value of $Z_n$ ( $n = 1, 2, 3, \dots, N$ )
$Z_n$	Mode load
$f'_c$	Unconfined compressive strength of concrete
$k$	Strength increase factor
$k_\alpha$	Parameter that reflects our confidence that the probability of survival is greater than or equal to $P(X_n > Z_n)$
$m, c$	Experimentally determined parameters in the fatigue equation $ns^m = c$
$\bar{m}$	Fatigue parameter, equal to the mean value of the exponent of the fatigue equation, $ns^m = c$

SYMBOLS AND NOTATIONS (concluded)

$n$	Cycles to implosion at stress level $s$
$n$	Index denoting repeated application of load (Sec. 6 only)
$n_z$	Life of the mode under load $z$ (Sec. 6)
$t$	Thickness of sphere wall
$\Delta \bar{x}_n$	COV that reflects our uncertainty in estimating $\mu_{\bar{x}_n}$ , the mean of $x_n$
$\Delta \bar{z}$	COV that reflects our uncertainty in estimating $\mu_{\bar{z}_n}$ , the mean of $z_n$ ( $n = 1, 2, 3, \dots, N$ )
$\psi(n)$	Mode resistance degradation function under repeated loads
$\delta_{\bar{x}_n}$	COV that reflects the real random nature of $\bar{x}_n$
$\delta_z$	COV that reflects the real random nature of $\bar{z}_n$ ( $n = 1, 2, 3, \dots, N$ )
$\epsilon_R(R)$	Radial strain at radius $R$
$\epsilon_\phi(R)$	Hoop strain at radius $R$
$\lambda$	Long-term loading factor, = 1 for short-term, noncyclic loading
$\nu$	Poisson's ratio
$\rho_{rs}$	Correlation coefficient
$\sigma_R(R)$	Radial stress at radius $R$
$\sigma_{im}$	Average wall stress at implosion
$\sigma_\phi(R)$	Hoop stress at radius $R$
$\Phi(\xi)$	Tabulated cumulative probability of the standard normal variate $\xi$

## DISTRIBUTION LIST

### DEPARTMENT OF DEFENSE

Assistant to the Secretary of Defense  
 Atomic Energy  
 ATTN: Honorable Donald R. Cotter

Director  
 Defense Advanced Rsch. Proj. Agency  
 ATTN: PMO  
 ATTN: Technical Library  
 ATTN: STO  
 ATTN: NMRO, Lt Colonel Bulin

Director  
 Defense Communications Agency  
 ATTN: CCTC, Major E. Volberding

Defense Communications Agency  
 WWMCCS Systems Engineering Org.  
 2 cy ATTN: Thomas Neighbors

Defense Documentation Center  
 Cameron Station  
 12 cy ATTN: TC

Director  
 Defense Intelligence Agency  
 ATTN: DB-4C2, Timothy Ross

Director  
 Defense Nuclear Agency  
 ATTN: DDST  
 ATTN: TISI  
 ATTN: RAEV  
 ATTN: STVL  
 3 cy ATTN: SPSS  
 3 cy ATTN: TITL

Commander  
 Field Command  
 Defense Nuclear Agency  
 ATTN: FCPR  
 ATTN: FCTMOF

Director  
 Joint Strat. Tgt. Planning Staff, JCS  
 ATTN: STINFO Library

Chief  
 Livermore Division, Fld. Command, DNA  
 Lawrence Livermore Laboratory  
 ATTN: FCPRL

Chief  
 Test Construction Division  
 Field Command Test Directorate  
 Defense Nuclear Agency  
 2 cy ATTN: Joe LaComb

Under Secretary of Def. for Rsch. & Engrg.  
 ATTN: S&SS (OS)  
 ATTN: AE

### DEPARTMENT OF THE ARMY

Director  
 Construction Engineering Rsch. Lab.  
 ATTN: CERL-SL

Dep. Chief of Staff for Rsch. Dev. & Acq.  
 ATTN: Technical Library

Chief of Engineers  
 ATTN: DAEN-MCE-D  
 ATTN: DAEN-RDM

Deputy Chief of Staff for Ops. & Plans  
 ATTN: Technical Library

Commander  
 Harry Diamond Laboratories  
 ATTN: DELHD-EM, John Bombardt

Director  
 U.S. Army Ballistic Research Labs.  
 ATTN: DRXBR-X, Julius J. Meszaros  
 ATTN: DRDAR-BLE, J. H. Keefer  
 ATTN: DRDAR-BLE, W. Taylor  
 ATTN: Tech. Lib., Edward Baicy

Commander and Director  
 U.S. Army Cold Region Res. Engr. Lab.  
 ATTN: Scott Blouin

Commander  
 U.S. Army Communications Command  
 ATTN: Technical Library

Commander  
 U.S. Army Engineer Center  
 ATTN: ATSEN-SY-L

District Engineer  
 U.S. Army Engineer Dist. Omaha  
 ATTN: MROED-D, Carl Distefano

Division Engineer  
 U.S. Army Engineer Division, Huntsville  
 ATTN: HNDED-SR  
 3 cy ATTN: Charles Huang

Division Engineer  
 U.S. Army Engineer Division, Ohio River  
 ATTN: Technical Library

Director  
 U.S. Army Engr. Waterways Exper. Sta.  
 ATTN: William Flathau  
 ATTN: James Drake  
 ATTN: James Ballard  
 ATTN: Leo Ingram  
 ATTN: Technical Library  
 ATTN: Paul Mlakar  
 ATTN: J. D. Day  
 ATTN: Guy Jackson

DEPARTMENT OF THE ARMY (Continued)

Commander  
U.S. Army Nuclear & Chemical Agency  
ATTN: Technical Library

DEPARTMENT OF THE NAVY

Officer-in-Charge  
Civil Engineering Laboratory  
Naval Construction Battalion Center  
ATTN: Technical Library  
ATTN: Stan Takahashi  
ATTN: L51, Warren Shaw  
ATTN: R. J. Odello  
ATTN: Harvey Haynes

Director  
Naval Cmd., Control & Communications  
ATTN: OP-943, S. Lechter

Commander  
Naval Electronic Systems Command  
ATTN: PME 117-21A, B. Kruger

Commander  
Naval Facilities Engineering Command  
ATTN: E. R. Violett  
ATTN: Technical Library

Superintendent (Code 1424)  
Naval Postgraduate School  
ATTN: Code 2124, Tech. Rpts. Librarian

Director  
Naval Research Laboratory  
ATTN: Code 2600, Tech. Library

Naval War College  
ATTN: Technical Library

Director  
Strategic Systems Project Office  
ATTN: NSP-43, Tech. Library

DEPARTMENT OF THE AIR FORCE

AF Geophysics Laboratory, AFSC  
ATTN: SUOL, Rsch. Library

AF Institute of Technology, AU  
ATTN: Library AFIT Bldg. 640, Area B

AF Weapons Laboratory, AFSC  
ATTN: DES-S, M. A. Plamondon  
ATTN: NT, Daniel N. Payton  
ATTN: SUL

Headquarters  
Air Force Systems Command  
ATTN: DLCA, Maj Celec

Commander  
Foreign Technology Division, AFSC  
ATTN: NICD Library

Hq USAF/RD  
ATTN: RDQSM, Lt Col Montulli

Hq USAF/SA  
ATTN: SASM

DEPARTMENT OF THE AIR FORCE (Continued)

Hq USAF/XO  
ATTN: XODC

SAMSO/MN  
ATTN: MNN  
ATTN: MNHH

Commander in Chief  
Strategic Air Command  
ATTN: NRI-STINFO Library

DEPARTMENT OF ENERGY

Department of Energy  
Division of Headquarters Services  
ATTN: Doc. Con. for Class Tech. Lib.

University of California  
Lawrence Livermore Laboratory  
ATTN: Tech. Info. Dept. L-3  
ATTN: David Oakley, L-21  
ATTN: Larry W. Woodruff, L-96  
ATTN: Hugh Heard

Los Alamos Scientific Laboratory  
ATTN: Doc. Con. for Reports Lib.  
ATTN: Doc. Con. for Larry Germaine  
ATTN: Doc. Con. for James Johnson  
ATTN: Doc. Con. for Barbara Killian

Oak Ridge National Library  
Union Carbide Corporation-Nuclear Division  
ATTN: Doc. Con. for Tech. Lib.

Sandia Laboratories  
Livermore Laboratory  
ATTN: Doc. Con. for Tech. Library

Sandia Laboratories  
ATTN: Doc. Con. for 3141 Sandia Rpt. Coll.  
ATTN: L. Hill

OTHER GOVERNMENT AGENCY

Department of the Interior  
Bureau of Mines  
ATTN: Technical Library

DEPARTMENT OF DEFENSE CONTRACTORS

Aerospace Corporation  
ATTN: Tech. Info. Services  
ATTN: Prem N. Mathur

Agbabian Associates  
2 cy ATTN: M. Agbabian  
ATTN: M. Balachandra  
ATTN: C. Bagge

Applied Theory, Inc.  
2 cy ATTN: John G. Trulio

Avco Research & Systems Group  
ATTN: Research Lib. A830, Rm. 7201

Battelle Memorial Institute  
ATTN: Technical Library

The BDM Corporation  
ATTN: Technical Library

DEPARTMENT OF DEFENSE CONTRACTORS (Continued)

**The Boeing Company**

ATTN: T. P. Berg  
ATTN: Robert Dyrdahl  
ATTN: James Wooster  
ATTN: Kenneth Friddell  
ATTN: Aerospace Library  
ATTN: H. G. Leistner

**California Research & Technology, Inc.**

ATTN: Technical Library  
ATTN: Sheldon Shuster  
ATTN: Ken Kreyenhagen

**Calspan Corporation**

ATTN: Technical Library

**Civil/Nuclear Systems Corp.**

ATTN: J. Bratten

**University of Dayton**

**Industrial Security Super. KL-505**  
ATTN: Hallock F. Swift

**University of Denver**

**Colorado Seminary**  
Denver Research Institute  
ATTN: Sec. Officer for J. Wisotski

**EG&G Washington Analytical Services Center, Inc.**

ATTN: Technical Library

**Electromechanical Sys. of New Mexico, Inc.**

ATTN: R. A. Shunk

**Engineering Decision Analysis Co., Inc.**

ATTN: Robert Kennedy

**Foster-Miller Associates, Inc.**

ATTN: J. M. Hampson for E. L. Foster

**The Franklin Institute**

ATTN: Zenons Zudans

**General Electric Company**

**TEMPO-Center for Advanced Studies**  
ATTN: DASIAC

**IIT Research Institute**

ATTN: Technical Library  
ATTN: Milton R. Johnson

**University of Illinois at Chicago**

**College of Engineering**  
Dept. of Materials Engineering  
ATTN: Ted Belytschko

**Institute for Defense Analyses**

ATTN: IDA Librarian, Ruth S. Smith

**J. H. Wiggins, Co., Inc.**

ATTN: Jon Collins

**Kaman AviDyne**

**Division of Kaman Sciences Corp.**  
ATTN: Technical Library

**Kaman Sciences Corporation**

ATTN: Library

DEPARTMENT OF DEFENSE CONTRACTORS (Continued)

**Lockheed Missiles and Space Co., Inc.**

ATTN: Tech. Info. Ctr., D/Coll.  
ATTN: Tom Geers, D/52023, Bldg. 205

**Massachusetts Institute of Technology**

ATTN: W. F. Brace, Rm. 54-720

**Merritt CASES, Incorporated**

ATTN: J. L. Merritt

**City College of New York**

**College of Engineering**  
Department of Civil Engineering  
ATTN: C. A. Miller

**Nathan M. Newmark**

**Consulting Engineering Services**  
ATTN: W. Hall  
ATTN: A. J. Hendron  
ATTN: Nathan M. Newmark

**Pacifica Technology**

ATTN: G. Kent

**Physics International Company**

ATTN: Doc. Con. for Fred M. Sauer  
ATTN: Doc. Con. for Dennis Orphal  
ATTN: Doc. Con. for E. T. Moore  
ATTN: Doc. Con. Coye Vincent  
ATTN: Doc. Con. Tech. Library

**R&D Associates**

ATTN: Technical Library  
ATTN: Henry Cooper  
ATTN: Robert Port  
ATTN: Cyrus P. Knowles  
ATTN: D. Shrinivasa  
ATTN: J. G. Lewis  
ATTN: Donald A. Rawson

**The Rand Corporation**

ATTN: Armas Laupa

**Science Applications, Inc.**

ATTN: Technical Library

**Science Applications, Inc.**

ATTN: Technical Library

**Southwest Research Institute**

ATTN: A. B. Wenzel  
ATTN: Wilfred E. Baker

**SRI International**

ATTN: B. S. Holmes  
ATTN: H. E. Lindberg  
ATTN: George R. Abrahamson

**Systems, Science and Software, Inc.**

ATTN: Donald R. Grine  
ATTN: Technical Library  
ATTN: Russell E. Duff  
ATTN: William Wray  
ATTN: Thomas Bache

**Terra Tek, Inc.**

ATTN: Howard Pratt  
ATTN: Technical Library

DEPARTMENT OF DEFENSE CONTRACTORS (Continued)

Tetra Tech, Inc.  
ATTN: Technical Library

Texas A & M Rsch. Foundation  
ATTN: Sec. Ofcr. for A. D. Rychlik

Texas A & M University System  
ATTN: John Handin

TRW Defense & Space Sys. Group  
ATTN: Norm Lipner  
ATTN: Peter K. Dai, R1/2170  
ATTN: Tech. Info. Center/S-1930  
ATTN: P. H. Huff

TRW Defense & Space Sys. Group  
San Bernardino Operations  
ATTN: E. Y. Wong, 527/712

DEPARTMENT OF DEFENSE CONTRACTORS (Continued)

Universal Analytics, Inc.  
ATTN: E. I. Field

The Eric H. Wang  
Civil Engineering Rsch. Fac.  
ATTN: Larry Bickle  
ATTN: Neal Baum  
ATTN: Gerald Leigh

Weidlinger Assoc. Consulting Engineers  
ATTN: Ivan Sandler  
ATTN: Melvin L. Baron

Weidlinger Assoc. Consulting Engineers  
ATTN: J. Isenberg

Westinghouse Electric Corp.  
ATTN: W. A. Volz